NRL Report 7942

Extension of Homogeneous Fluid Methods to the Calculation of Surface Disturbance Induced by an Object in a Stratified Ocean

MICHAEL H. REILLY

Space Environment Branch
Space Systems Division

February 24, 1976

NAVAL RESEARCH LABORATORY
Washington, D.C.

SECURITY CLASSIFICATION OF THIS PAGE *(When Data Entered)*

REPORT DOCUMENTATION PAGE		READ INSTRUCTIONS BEFORE COMPLETING FORM
1. REPORT NUMBER NRL Report 7942	2. GOVT ACCESSION NO.	3. RECIPIENT'S CATALOG NUMBER
4. TITLE *(and Subtitle)* EXTENSION OF HOMOGENEOUS FLUID METHODS TO THE CALCULATION OF SURFACE DISTURBANCE INDUCED BY AN OBJECT IN A STRATIFIED OCEAN		5. TYPE OF REPORT & PERIOD COVERED Final Report 6. PERFORMING ORG. REPORT NUMBER
7. AUTHOR*(s)* Michael H. Reilly		8. CONTRACT OR GRANT NUMBER*(s)* 74078-0104 (Ind.)
9. PERFORMING ORGANIZATION NAME AND ADDRESS Naval Research Laboratory Washington, D.C. 20375		10. PROGRAM ELEMENT, PROJECT, TASK AREA & WORK UNIT NUMBERS
11. CONTROLLING OFFICE NAME AND ADDRESS		12. REPORT DATE February 24, 1976 13. NUMBER OF PAGES 74
14. MONITORING AGENCY NAME & ADDRESS*(if different from Controlling Office)*		15. SECURITY CLASS. *(of this report)* Unclassified 15a. DECLASSIFICATION/DOWNGRADING SCHEDULE

16. DISTRIBUTION STATEMENT *(of this Report)*

Approved for public release; distribution unlimited.

17. DISTRIBUTION STATEMENT *(of the abstract entered in Block 20, if different from Report)*

18. SUPPLEMENTARY NOTES

19. KEY WORDS *(Continue on reverse side if necessary and identify by block number)*

Density-stratification effects
Hydrodynamic disturbance
Surface disturbance calculations

20. ABSTRACT *(Continue on reverse side if necessary and identify by block number)*

An extension of homogeneous fluid methods has been developed for calculation of the disturbance induced by a submerged point source in an incompressible, density-stratified fluid with a free surface. The extension comes in the treatment of the inhomogeneous wave equation, which results from linearization and Fourier transformation of the equations of motion. A closely related problem is the solution of the one-dimensional Schrodinger equation, where the negative squared Brunt-Vaisala frequency profile plays the role of the depth-dependent potential. A model potential

(Continued)

20. ABSTRACT (Continued)

with known bound state and continuum state eigenfunctions is substituted into the inhomogeneous wave equation, which is solved, subject to the free surface boundary condition, by an eigenfunction expansion method. Surface tension effects are also included. Contour integration techniques assist the evaluation of integrals and enable a clear separation of localized and extended wavelike disturbances. The point-source solutions may be used to calculate fluid disturbance in the near and far fields induced by a submerged body. As an example, the localized surface displacement and rate of strain induced by a submerged Rankine ovoid are calculated for a square-well density-stratification model. The results are compared to previously calculated far-field internal wave effects induced on the surface by wake collapse behind a submerged body.

CONTENTS

INTRODUCTION 1

GENERAL FORMALISM FOR A SUBMERGED POINT SOURCE 4

Linearized Equations of Motion for an Incompressible Fluid 6
Free-Surface Boundary Condition 7
Fourier-Transformed Equations 7
Solution for $\overline{w}$ 9
Evaluation of w: Contour Integration Techniques 10

POINT SOURCE IN A MODEL OCEAN ENVIRONMENT 13

The Model 13
Particular Solution $\overline{w}_p$ — Point Source Below Thermocline (PSBT) 14
Full Solution $\overline{w}$ (PSBT) 18
Evaluation of w (PSBT) 20
Surface Displacement ζ (PSBT) 28
Surface Rate of Strain S (PSBT) 29
Effect of the Rigid-Lid Condition 30

NUMERICAL CALCULATIONS FOR LOCALIZED SURFACE DISTRUBANCE INDUCED BY A RANKINE OVID 30

Simulation of the Ovoid 31
Use of Symmetries 32
Numerical Procedure 34
Results for Rankine Ovoid Model 36
Possible Effects of a More Realistic Model 58

COMPARISON WITH PREVIOUS RIGID-LID CALCULATIONS OF SURFACE DISTURBANCE INDUCED BY WAKE COLLAPSE 59

DISCUSSION 61

ACKNOWLEDGMENTS 63

REFERENCES 63

APPENDIX A – Homogeneous Fluid Solution for $\bar{w}$ 65

APPENDIX B – Evaluation of $\overline{W}_{p2}^{C}$ 66

APPENDIX C – Analytic Continuation of $F(x) = \sqrt{z^2 - a^2}$ 67

APPENDIX D – Filon's Method and Relevant Procedures 69

EXTENSION OF HOMOGENEOUS FLUID METHODS TO THE CALCULATION OF SURFACE DISTURBANCE INDUCED BY AN OBJECT IN A STRATIFIED OCEAN

INTRODUCTION

The surface disturbance induced by a submerged body has been a problem of considerable interest to theoretical hydrodynamicists and others for decades. For simplicity, most theoretical calculations have been limited to homogeneous fluids. The results have been used to account for wave resistance, stability of ships, and other matters important for ship design. The status of the theory and calculations prior to 1951 has been reviewed bv Lunde [1]. Many calculations have modeled the submerged body by a distribution of point sources and sinks, designed to provide streamlines which are tangent to the submerged body. Calculations of surface displacement in a homogeneous fluid were performed by Yim using this method [2]. A submarine was modeled by a separated point source and point sink pair for the hull and by a line dipole source and line dipole sink for the sail. Later, Yim's calculations for the localized part of the surface disturbance due to the hull were extended to deeper depths [3]. The surface disturbance due to a submerged point source is initially of interest. Once this result is in hand, the disturbance from a distribution of sources and sinks is obtained by simple linear superposition.

Over the last dozen years or so, several studies of submerged bodies in more realistic ocean environments, which include a density depth dependence, have disclosed other effects which must be accounted for. Some of these are indicated in Fig. 1. We note first a hull, simulated by a point source and point sink of strength q. The surface displacement ζ calculation due to the hull has been mentioned above. The density ρ depth dependence is shown. Associated with it is a Brunt-Vaisala (B-V) frequency N, proportional to the logarithmic derivative of ρ. A fluid element displaced upward will find itself in a lighter mass environment and sink back down. Similarly, a fluid element displaced downward will experience a restoring force upward. The B-V frequency is essentially the oscillation frequency of such a fluid element. An idealized N^2 depth dependence is also shown in Fig. 1. Three layers are clearly discernible: (a) a surface layer down to some depth, (b) a thermocline layer where the density is rapidly varying, and (c) the rest of the ocean below the thermocline. Actually, the N^2 profile does not ordinarily have the inverted-square-well profile shown in Fig. 1, but, for convenience, this will be the model for our computer calculations of the localized disturbance.

A turbulent wake behind the hull is also indicated in Fig. 1. The point source and sink used for the hull do not include the contribution of the turbulent wake to surface disturbance. In its growth stage the turbulent wake will entrain more and more of the surrounding fluid until the energy of the turbulence exceeds the potential energy of entrainment, which exists because fluid elements have been displaced away from their equilibrium positions. At this point wake collapse begins and takes place on the time scale of the inverse B-V frequency. In wake collapse, the turbulent wake squashes down vertically and spreads out horizontally. Wake collapse is thought to be accompanied by significant internal wave generation, which is a manifestation of

Manuscript submitted October 16, 1975.

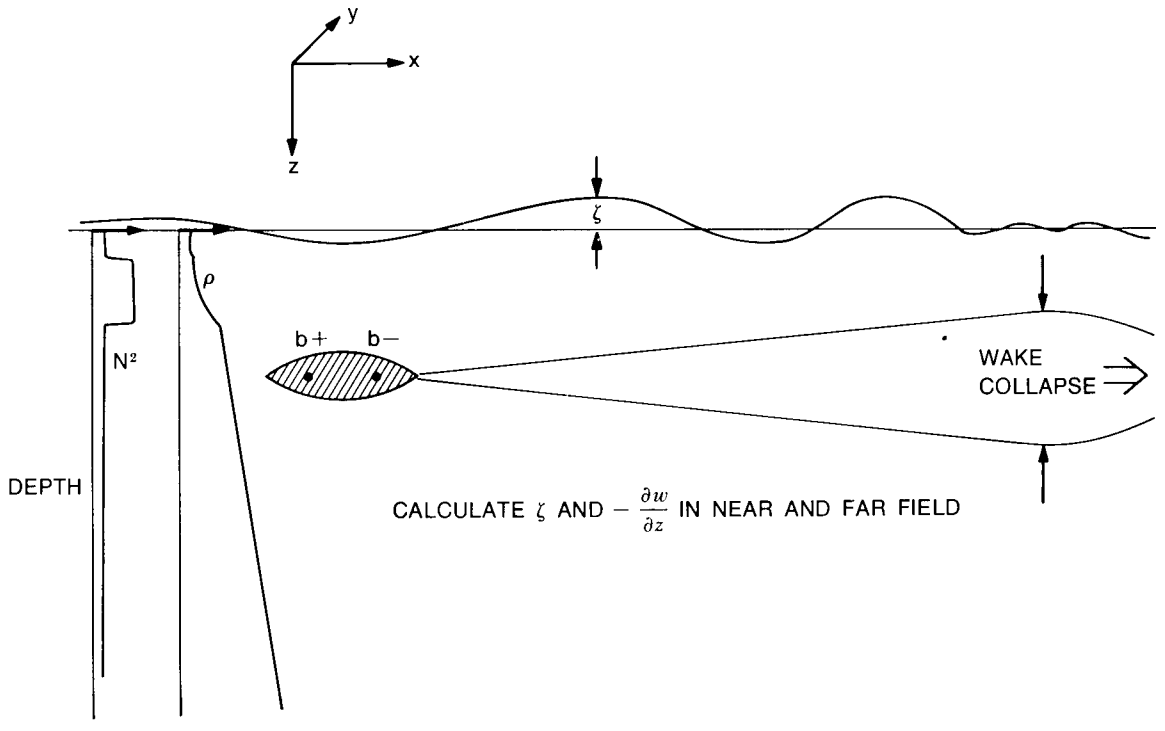

Fig. 1 – Schematic illustration of a hull in a stratified ocean. Some of the features shown are an induced surface displacement ζ, the point source and sink of strength q used to simulate the hull, a turbulent wake, and model depth dependence for the density ρ and squared Brunt-Vaisala frequency N^2.

the aforementioned fluid oscillation in a density-stratified medium. The phenomenon has been studied both experimentally and theoretically. Reference 4 includes a survey of previous work on wake collapse. The prevailing theoretical approach is to treat the fully expanded wake as a mixed region of quiescent fluid and to employ its density distribution as an initial condition in the numerical solution to the two-dimensional Navier-Stokes equations, involving the y and z coordinates (see Fig. 1) and time (the so-called $2d + t$ approximation). The displacement of the effects relative to the hull in the x direction is very simply related to the time – i.e., linearly through the hull's velocity. The surface boundary condition employed in the calculations is that of zero displacement. It is often referred to as the "rigid-lid" boundary condition.

It is convenient to refer to the near field and the far field in describing previous calculations. The near field rather arbitrarily describes the region on the surface within one hull depth (or length, whichever is larger) away from the source projection on the surface. By "source" we mean here, for example, the hull displacement region or portion of the turbulent wake under consideration. Similarly, the farfield will refer to regions on the surface at distances substantially further than one hull depth (or length) from the source projection on the surface. The Bernoulli depression is a near-field disturbance to which gravity waves make a substantial contribution. The Kelvin wake calculation of Yim [2] uses a fairly elaborate stationary phase method which is valid for the far field. All such gravity-wave effects require a free-surface boundary condition for their description.

There have been several recent calculations of internal wave contributions to surface disturbance which utilize a rigid-lid boundary condition for model density stratifications. Carrier and Chen [5] utilize a limited eigenfunction expansion to describe the wavelike hydrodynamic effects from a submerged body in the far field. Their model employs a B-V frequency which is zero, except for a thermocline layer where the B-V frequency is some positive constant. This is similar to the B-V square-well model that we shall employ for our calculations. A delta-function B-V frequency for the thermocline is an idealized limit of the square-well model used by Carrier and Chen [5], and this delta-function model has recently been used to calculate near-field internal wave contributions from a moving point dipole [6]. Substantial contributions from internal waves were found. Miles [7] had previously used this model and a constant-stratification model in the calculation of internal wave effects from a slender body in the far field. For completeness, we mention another TRW report by Hindman [8] on internal waves from collapsing wakes, although the author has not seen it yet. Finally, Piacsek [9] has performed rigid-lid calculations of surface fluid velocity and rate of strain from wake collapse for very many B-V profiles. These profiles are realistic fits [10] to measured, seasonally averaged, B-V profiles for the world oceans. Piacsek's calculations involve a full numerical solution of the Navier-Stokes equations in the $2d + t$ approximation and should therefore yield the internal wave surface disturbance from wake collapse in the near and far fields. Piacsek also has performed calculations (unpublished) on the effects of current shear.

It has become clear that a unified treatment of all the various hydrodynamic effects from a submerged source and its surface manifestation is desirable. We should like to include realistic B-V profiles in the formalism. Further, the interplay of gravity waves and internal waves can be important. Certainly, the Bernoulli depression, Kelvin wake, and other effects associated with gravity waves are dominant under some circumstances; the effects of internal waves are dominant in others. There is an intermediate region where both types of effects are important. We would like a unified treatment to be capable of including both hull displacement and turbulent wake effects, especially with regard to induced surface disturbance.

This report gives one possible unified treatment. It represents an extension of the homogeneous fluid approach taken by Yim [2]. Some important similarities are as follows. A free-surface boundary condition is used so that both gravity and internal wave effects can be taken into account correctly. A reference frame fixed to the hull is used, so that the fluid velocity components appear to be $(U + u, v, w)$ in Fig. 1, where the hull is moving with speed U in the negative x-direction. Here (u, v, w) are the fluid velocities induced by the submerged body, which are treated as small in a standard linearization of the Navier-Stokes equations. This choice of reference frame eliminates the time dependence. A two-dimensional Fourier transform in surface coordinates (x and y in Fig. 1) is used. The formalism includes both near- and far-field effects. Further, a separation of the various effects is made with the assistance of contour integration techniques. Initially, we concentrate on fluid disturbance induced by a submerged point source. The philosophy is that the effects of hull displacement and turbulent wake on the surface can later be taken into account by a suitable distribution of point sources and sinks. The corresponding expressions are obtained by simple algebraic manipulation of the point-source expressions, based on linear superposition.

The extensions of the homogeneous fluid approach are as follows. To include a realistic B-V profile we perform a full eigenfunction or normal mode expansion, appropriately defined, in the

z-dependence of the two-dimensional Fourier-transformed Navier-Stokes equations. This is similar to the approach of Carrier and Chen [5], who essentially used a limited eigenfunction expansion to describe far-field internal wave effects with a model B-V profile and with a rigid-lid boundary condition. We use a full eigenfunction expansion with a free-surface boundary condition, which is pointed to the arbitrary B-V profile case, and a description of both near- and far-field effects from both gravity and internal waves. We obtain expressions for the z-component of fluid velocity induced by a point source. The effects of surface tension are also included in the formalism.

The general formalism is developed in the following section for the solution of the problem of the flow velocity induced by a point source in a density-stratified, incompressible fluid. In the third section, expressions are obtained for a square-well model B-V profile, as indicated in Fig. 1. The B-V frequency is equal to some arbitrary nonnegative constant in this model, except in the thermocline region, where it can be a larger positive constant. Numerical computations of the localized surface disturbance from a submerged hull are then performed for a variety of stratification models, which include square-well fits to several representative smoothed B-V profiles. Finally, these results are compared to the results of rigid-lid calculations of surface disturbance induced by wake collapse [9]. The results of this work are discussed in the last section. The reader is urged to refer to the Contents page included with this work, where a more complete listing of topics is included. He may wish to avoid reading those parts that are of no immediate consequence to him.

There are parts of this work which seem to be new, or at least, not readily available in the literature of fluid dynamics. They include (a) a fuller exploitation of the eigenfunction expansion method for solving the Fourier-transformed equations of motion in a density-stratified, incompressible fluid, subject to a free surface boundary condition, (b) a more complete treatment of surface tension effects, (c) a calculation of the localized surface disturbance induced by the hull which includes both gravity and internal wave effects, and (d) a fuller evaluation of the relative importance of the localized surface disturbance caused by the hull and internal wave effects on the surface induced by wake collapse. In the computations a wide variety of stratification models was used, including various constant stratifications and square-well fits to several representative smoothed B-V frequency profiles. Surface displacements and rates of strain were computed, an angular dependence of localized surface disturbance was calculated for a particular case, and a dramatic resonance enhancement associated with square-well thermoclines was found. It is hoped that this work will help enable the inclusion of internal-wave and gravity-wave effects in future calculations of localized and wavelike contributions to the surface disturbance induced by a submerged body in a density-stratified fluid.

GENERAL FORMALISM FOR A SUBMERGED POINT SOURCE

Linearized Equations of Motion for an Incompressible Fluid

The equation of motion of an incompressible viscous fluid is [11]

$$\rho \frac{d\mathbf{v}}{dt} = -\nabla p - \rho g \mathbf{z} + \mu \nabla^2 \mathbf{v}, \tag{1}$$

where ρ, $\mathbf{v}$, p, $\mathbf{z}$, and μ are, respectively, the density, velocity, pressure, unit vector in the z direction, and dynamic viscosity in the fluid at a particular point. The entity g is the acceleration due to gravity. We adopt the coordinate system shown in Fig. 1. The coordinate axes move at the constant velocity of the point source, which is in the negative x direction and has magnitude U. In these coordinates the fluid velocity $\mathbf{v} = (U + u, v, w)$. There is no explicit time dependence in the problem, since it is assumed that the fluid is quiescent in the absence of the point source. Hence,

$$\frac{d\mathbf{v}}{dt} = (\mathbf{v} \cdot \nabla)\mathbf{v} \approx U\frac{\partial \mathbf{v}}{\partial x}. \tag{2}$$

Here we see one of the approximations which enters into the linearization of Eq. (1).

In the region of interest (e.g., near the surface) the fluid velocity components u, v, and w, which are induced by the point source, are much smaller than the velocity of the point source. Similarly, the density and pressure can be written as

$$\rho = \rho_o(z) + \rho'(x,y,z)$$

and

$$p = p_o(z) + p'(x,y,z),$$

where $\rho_o(z)$ and $p_o(z)$ are the density and pressure in the absence of the point source, which are assumed to be much larger than the induced density and pressure ρ' and p' in the region of interest. From Eq. (1) we have

$$p_{oz} + \rho_o\, gz = 0, \tag{3}$$

where p_{0z} denotes $\partial p_0/\partial z$, and similarly for x and y subscripts which will be used. To first order in the induced entities, the components of Eq. (1) become:

$$\rho_o U u_x + p_x' - \mu\nabla^2 v = 0 \tag{4}$$
$$\rho_o U v_x + p_y' - \mu\nabla^2 v = 0 \tag{5}$$
$$\rho_o U w_x + p_z' + \rho' g - \mu\nabla^2 w = 0. \tag{6}$$

These are the linearized equations of motion.

At first sight it may appear strange that the viscosity terms are kept at all in Eqs. (4)-(6). It is known, for example, that some of the terms thrown out of $\rho(\mathbf{v} \cdot \nabla)\mathbf{v}$ in the linearization (see Eq. (2)) are much larger than the viscosity terms. They are larger by a factor of the Reynold's number which is known to be extremely large for this problem. The viscosity terms are kept, for now, because they represent the causality assumptions in the problem – viz, the only guarantee in our equations that if the point source is removed, the induced perturbations will decay with time. The significance of this will be shown below. The author believes that this method of incorporating causality assumptions by means of viscosity is not dissimilar to a "frictional" force approach originated by Kelvin. The approach of linearizing the equations of motion is also standard [1,6].

From Eqs. (4) and (5) one obtains

$$(\rho_o U\, \partial/\partial x - \mu\nabla^2)\ \ (u_y - v_x) = 0,$$

which is implied by $u_y = v_x$. Hence, we assume that these velocity components can be obtained from a scalar potential $\phi(x, y, z)$:

$$u = \phi_x \qquad \text{and} \qquad v = \phi_y. \tag{7}$$

Next we write the equation of continuity for an incompressible fluid, for which

$$\frac{d\rho}{dt} = 0 = (\mathbf{v} \cdot \nabla)\rho \approx U\rho_x' + w\rho_{oz} \tag{8}$$

For a point source of strength M at position $\mathbf{r}_s = (x_s, y_s, z_s)$, the equation of continuity becomes

$$\nabla \cdot \mathbf{v} = \phi_{xx} + \phi_{yy} + w_z = M\delta(x - x_s)\delta(y - y_s)\delta(z - z_s). \tag{9}$$

The point source is seen to be adding fluid to its environment at the rate of M volume units per unit time. A distribution of point sources and sinks can be used to simulate the effect of an object, as will be discussed later. After Eq. (7) is substituted into Eqs. (4) and (5) it is seen that Eqs. (4) – (6), (8), and (9) are five coupled linear differential equations for the six unknowns, ϕ, w, p_x', p_y', p_z', and ρ'. We need another equation, which is the free-surface boundary condition (an infinitely deep ocean is assumed).

Free-Surface Boundary Condition

Another form of Eq. (1) which is approximately valid near the free surface is

$$\rho(\mathbf{v} \cdot \nabla)\mathbf{v} = \frac{1}{2}\rho\nabla(v^2) \approx -\nabla(p + \rho gz - \mu\nabla^2\phi),$$

where we have used Eq. (7) and the fact that

$$w \approx \phi_z \qquad (i.e., \mathbf{v} \approx \nabla\phi)$$

near the surface. Along a streamline (e.g., the free surface) ρ does not vary (see Eq. (8)), so that

$$\frac{1}{2}\rho v^2 + p + \rho gz - \mu\nabla^2\phi = \text{const.} \tag{10}$$

along a streamline. This is essentially Bernoulli's equation for steady flows [12]. Lunde [1] included a frictional term similarly to our inclusion of viscosity. The right-hand side of Eq. (10) can be taken to the value of the left-hand side far upstream or downstream of the source, so that if p_a is the ambient pressure just above the surface and z_o is the undisplaced surface level, we have

$$\frac{1}{2}\rho v^2 + p + \rho gz - \mu\nabla^2\phi = \frac{1}{2}\rho U^2 + p_a + \rho gz_o. \tag{11}$$

The free-surface displacement is ζ (e.g., see Fig. 1), so that $z = z_o + \zeta(x,y)$. Just below the free surface, p is related to p_a by†

†See Ref. 11, Sec. 60.

$$p = p_a + T\left(\frac{1}{R_1} + \frac{1}{R_2}\right) = p_a - T\,\frac{\nabla^2\zeta(x,y)}{[1 + (\nabla\zeta)^2]^{3/2}}, \tag{12}$$

where T is the surface tension coefficient and R_1 and R_2 are the principal radii of curvature at a given point of the surface. Combining Eqs. (11) and (12) and linearizing, we obtain

$$-T\nabla^2\zeta + \rho_o g\zeta + \rho_o U\phi_x - \mu\nabla^2\phi = 0. \tag{13}$$

as the free-surface boundary condition. Another unknown variable ζ has been introduced, but it is related to w through the kinematic boundary condition at the free surface:

$$w|_{z=z_0} = d\zeta/dt = (\mathbf{v}\cdot\nabla)\zeta \approx U\zeta_x. \tag{14}$$

Fourier-Transformed Equations

It is customary [1] to use the two-dimensional Fourier transform (FT) on x and y coordinates (see Fig. 1) in order to simplify the solution of the preceding equations. It is given, for example, by

$$w(x,y,z) = (2\pi)^{-2}\iint_{\xi>0} \overline{w}(\zeta,\eta,z)\, e^{i(\xi x+\eta y)}\, d\xi d\eta + c.c., \tag{15}$$

where the FT of w is $\overline{w}$, and analogously for the other fluid entities. The integration in the first term is limited to the half-space $\xi > 0$, and the term $c.c.$ denotes the complex conjugate of the first term on the right in Eq. (15). We can apply the FT to the previous equations. For the sake of discussion, we give the FT of one of the equations of motion (i.e., Eq. (6)) and of the free-surface boundary condition (i.e., Eq. (13)), which appear as

$$\rho_0 Ui\left(\xi - i\frac{\mu K^2}{\rho_0 U}\right)\overline{w} + \overline{p_z}' + \overline{\rho}' g - \mu\overline{w}_{zz} = 0$$

and

$$(TK^2 + \rho g)\overline{\zeta} + i\rho_0 U(\xi - i\frac{\mu K^2}{\rho_0 U})\,\overline{\phi} - \mu\overline{\phi}_{zz} = 0. \tag{16}$$

Here we have used the definition $K^2 \equiv \xi^2 + \eta^2$, which is a consequence of a transformation from rectangular coordinates (ξ, η) to cylindrical coordinates (K, θ)

$$\xi = K\cos\theta$$

and

$$\eta = K\sin\theta,$$

where

$$-\frac{\pi}{2} < \theta < \frac{\pi}{2} \text{ for } \xi > 0. \tag{17}$$

We intend to drop the relatively negligible viscosity term now, after we notice its effect. The effect is that ξ is to be regarded as having an infinitesimal negative imaginary part. This is essentially an effect of causality and will be seen later to have the profound consequence that wavelike hydrodynamic effects are largely restricted to the half-space behind the hull. In fact, this statement itself

is the causality assumption used by many authors. Hence, we drop the viscosity terms with this understanding about ξ. The FT of the equations of motion (4)–(6) combined with Eq. (7) is

$$\rho_0 U i\xi \bar{\phi} + \overline{p'} = 0 \tag{18}$$

$$\rho_0 U i\xi \bar{w} + \overline{p_z'} + \bar{\rho} g = 0. \tag{19}$$

We now eliminate the pressure terms from these two equations by taking the z derivative of Eq. (18) and subtracting it from Eq. (19) to obtain

$$i\xi\, U\rho_0\, [\bar{w} - \bar{\phi}_z - (\rho_{0z}/\rho_0)\bar{\phi}] = -\overline{\rho' g}. \tag{20}$$

Since ρ_{0z}/ρ_0 is of order $10^{-4}m^{-1}$, or less, we neglect the third term in square brackets compared to the second term, which is of order $\bar{\phi}/L$ where L is a characteristic length of the order of the point-source depth. One then uses the FT of the incompressibility equation (Eq. (8)), which is

$$i\xi U\overline{\rho'} + \rho_{0z}\bar{w} = 0 \tag{21}$$

Substitution into Eq. (20) yields

$$\bar{\phi}_z = \bar{w} - (N^2/U^2\xi^2)\,\bar{w}, \tag{22}$$

where $N^2(z) = -g\rho_{0z}/\rho_0$ and $N(z)$ is the B-V frequency. The equation of continuity (Eq. (9)) becomes

$$\bar{w}_z - K^2\bar{\phi} = M\delta(z - z_s)\exp\{-i\xi x_s - i\eta y_s\}. \tag{23}$$

These equations are subject to the boundary conditions at the free surface (Eqs. (13) and (14)), which are

$$[TK^2 + \rho_0 g]\bar{\zeta} + \rho_0 U i\xi\bar{\phi}(0) = 0 \tag{24}$$

$$\bar{w}(0) = i\xi U\bar{\zeta}, \tag{25}$$

where $\bar{w}(0)$ and $\bar{\phi}(0)$ are the values of $\bar{w} = \bar{w}(z)$ and $\bar{\phi} = \bar{\phi}(z)$ at $\zeta = 0$ in first order theory. We can combine Eqs. (22) and (23) and then Eqs. (23) - (25) to obtain

$$\bar{w}_{zz} + \left(\frac{N^2(z)}{U^2\cos^2\theta} - K^2\right)\bar{w} = M\delta_z(z - z_s)\exp(-i\xi x_s - i\eta y_s) \tag{26}$$

for the motion equation for $\bar{w}$ and

$$K_0\bar{w}(0) = \cos^2\theta\ \bar{w}_z(0),$$

where

$$K_0 \equiv \frac{TK^2}{\rho_0 U^2} + \frac{g}{U^2} \tag{27}$$

for the free-surface boundary condition satisfied by $\bar{w}$.

Solution for $\overline{w}$

For the moment, we ignore the presence of the surface and extend the definition of N^2 beyond the free surface ($z > z_0$) in some convenient, continuous fashion. For example, $N^2(z)$ could be smoothly extended to zero, or to a particular constant value in accordance with a particular analytic fit in a model calculation. We then are faced with the problem of finding the solution to a wave equation (Eq. (26)) in an infinite medium. The solution will thus be a particular solution, which will be found in this part through an eigenfunction expansion. The eigenvalue problem associated with Eq. (26) is defined by

$$-u_{zz} + W_\theta(z)u = \lambda u\,,$$

where

$$W_\theta(z) \equiv -N^2(z)/U^2\cos^2\theta, \tag{28}$$

which is written this way to emphasize the fact that it is a one-dimensional Schrodinger equation where $-N^2/U^2\cos^2\theta$ plays the part of the potential energy. For simplicity of description, we assume that N^2 tends to zero at great distances away from the region of interest. There is no difficulty in handling the case where N^2 tends to a constant value, as we shall see below. A particular solution $\overline{w}_p$ of Eq. (26) can be expanded in terms of the eigenfunction solutions of Eq. (28):

$$\overline{w}_p = \Sigma_n A_n U_n + \int dk A(k) u_k, \tag{29}$$

where the first term denotes the sum over the discrete bound states and the second term denotes the integral over continuum states. The expansion also includes degenerate eigenfunctions. We define the real eigenvalues by

$$\lambda \equiv \left\{\begin{matrix} -k_n^2 \text{ for bound states } (\lambda < 0) \\ k^2 \text{ for continuum states } (\lambda > 0) \end{matrix}\right\}. \tag{30}$$

The u_n and u_k comprise a complete orthonormal set, and it is straightforward to utilize these properties in the substitution of Eqs. (29) and (30) into Eq. (26) to obtain the expansion coefficients. The result is

$$\overline{w}_p(z) = M\exp(-i\xi x_s - i\eta y_s)\left\{\Sigma_n \frac{u_{nz}(z_s)^* u_n(z)}{K^2 - k_n^2} + \int_0^\infty dk \frac{u_{kz}(z_s)^* u_k(z)}{K^2 + k^2}\right\}, \tag{31}$$

where, e.g., $u_{nz}(z_s)^*$ is the z partial derivative of $u_n(z)^*$ evaluated at $z = z_s$.

To the particular solution just found we must add a general solution $\overline{w}_H$ of the homogeneous equation associated with Eq. (26) (i.e., without source term), which is adapted to satisfy the free-surface condition, Eq. (27). The solution $\overline{w}_H$ will have the property that

$$\overline{w}_H(z) \sim Ae^{Kz} \qquad \text{as } z \to -\infty. \tag{32}$$

The asymptotic solution $\exp(-Kz)$ is ruled out since it diverges in this limit. The constant A is chosen so that Eq. (27) is satisfied. The general solution is found analytically for some potentials,

but Eq. (32) can generally serve as the initial condition in a numerical integration of the homogeneous differential equations in order to find $\bar{w}_H$. The fact that $\exp(Kz)$ diverges as $z \to \infty$ is of no consequence, as this is outside the region of interest ($z < z_0$). If we were dealing with an ocean of finite depth, Eq. (32) would be replaced by the condition that $\bar{w}_H = -\bar{w}_p$ at the ocean floor z-coordinate. The economy of the above approach is illustrated for the homogeneous fluid case in Appendix A.

Now we suppose that we have the more general situation, where N approaches a constant value at great depths:

$$N^2(z) \to N_0^2 \qquad \text{as } z \to -\infty, \tag{33}$$

and the extension of N^2 for $z > 0$ is to a constant value less than or equal to N_0^2. Then it is possible to regain the description above by regrouping terms in Eq. (26). The modifications are easily obtained:

$$\begin{aligned} &V_\theta \to -(N^2 - N_0^2)/U^2 \cos^2\theta \qquad \text{in Eq. (28);} \\ &K^2 \to K_\theta^2 \equiv K^2 - N_0^2/U^2 \cos^2\theta \qquad \text{in Eq. (31).} \end{aligned} \tag{34}$$

The full solution is thus

$$\bar{w} = \bar{w}_p(z) + \bar{w}_H(z), \tag{35}$$

where $\bar{w}_p(z)$ is given by Eqs. (31) and (34) and $\bar{w}_H(z)$ is a general solution. This solution satisfies

$$\bar{w}_{Hzz} + \left(\frac{N^2}{U^2\cos^2\theta} - K^2\right)\bar{w}_H = 0, \tag{36}$$

the conditions of Eqs. (32) and (34), and the free-surface boundary condition of Eq. (27), which becomes

$$\cos^2\theta \bar{w}_{Hz} - K_0 \bar{w}_H = -\cos^2\theta \bar{w}_{pz} + K_0 \bar{w}_p. \tag{37}$$

This is tantamount to adjustment of the constant A in Eq. (32).

Evaluation of w: Contour Integration Techniques

The solution w is given by Eq. (15), where we have seen that the ξ integration corresponds to a contour infinitesimally displaced beneath the real ξ axis in the complex ξ plane. From the definition in Eq. (17) we have $K = (\xi^2 + \eta^2)^{1/2}$ from which it is easy to show that if ξ is given an infinitesimal negative imaginary component, so also is K given an infinitesimal negative imaginary component. Hence, if we set the origin of surface coordinates at the point of surface projection of the source (x_s, y_s) and define cylindrical coordinates with respect to it by

$$x = R\cos\delta, \qquad y = R\sin\delta \qquad 0 \leq \delta < 2n, \tag{38}$$

we can write Eq. (15) in the cylindrical coordinates of Eq. (17) as

$$w = (2\pi)^{-2} \int_{-\pi/2}^{\pi/2} d\theta \int_C K\bar{w}(K_\theta, \theta, z) e^{iK\omega}\, dK + c.c., \tag{39}$$

where $\omega \equiv R\cos(\theta - \delta)$. Here, K_θ is as given in Eq. (34), and the contour C is taken to be parallel to and infinitesimally displaced beneath the positive real K axis in the complex K plane.

From Eq. (31), we see that the K integration will have to contend with poles on the real axis associated with the values $K_n \equiv [k_n^2 + N_0^2/(U^2\cos^2\theta)]^{1/2}$. There are other poles which will arise. For example, in the homogeneous fluid case (Refs. 1 and 2 and App. A) there is another pole on the real axis at $K_0\sec^2\theta$ (neglecting surface tension) which gives the Kelvin wake contribution in contour integration. Other poles away from the real axis can also arise, as we shall see in the point source discussion. From Eqs. (39) and (40) and the fact that $\overline{w}$ is not an even function of K_θ, we see that it will be necessary to have a branch cut from $K = 0$ to $K = N_0/U\cos\theta$ on the real K axis. In our use of contour integration, it will be necessary to exclude this branch cut from within any closed contour that we form. For example, the residue theorem demands it; it applies to a function $\overline{w}$ which is analytic except for isolated poles, and single-valued within and on a closed contour.

Suitable closed contours are shown in Fig. 2 for the two cases $\omega > 0$ and $\omega < 0$. With respect to the simpler case $\omega < 0$ and Fig. 2b, the original K integral $\int_C KdK \ldots$ in Eq. (39) can be written in terms of the integral along the contour C_ℓ', which is along the negative imaginary axis;

$$\int_C KdK \ldots = -\int_{C_\ell'} KdK \ldots = -\int_0^\infty mdm \ldots, \tag{40}$$

since $K = -im (m > 0)$ along the negative imaginary axis. We substitute this into (see Eq. (34))

$$K_\theta(K) = [K^2 - N_0^2/(U^2\cos^2\theta)]^{1/2} \tag{41}$$

and we obtain from Eqs. (39) and (40) that

$$\int_C KdK \ldots = -\int_0^\infty mdm\, w(K_\theta(-im), \theta, z)e^{m\omega}.$$

In the case $\omega < 0$, as R gets larger, the exponential dumping factor $\exp(m\omega)$ has a larger effect, so that it is clear that the integral along the contour C_ℓ' gives a disturbance more or less localized to the vicinity of the hull. This is the mnemonic significance of the "ℓ" subscript which will be used again. Hence, for the region of the θ integration for which $\omega < 0$ we get only a localized disturbance contribution. Though we have not stated it, the contribution of the quarter-circle part of the contour C_R' with infinitely large radius is vanishingly small for $R \neq 0$.

In contrast, the situation for $\omega > 0$ in Fig. 2a is more complicated. The integral along C is written in terms of the contour C_ℓ along the imaginary axis, but also the contour C_s around the branch cut makes a contribution, as do the residue contributions from the simple poles on the K_x axis and elsewhere within the contour of Fig. 2a:

$$\int_C KdK \ldots = -\int_{C_\ell} KdK \ldots - \int_{C_s} KdK \ldots + 2\pi i\Sigma_\alpha \mathscr{R}(K_\alpha). \tag{42}$$

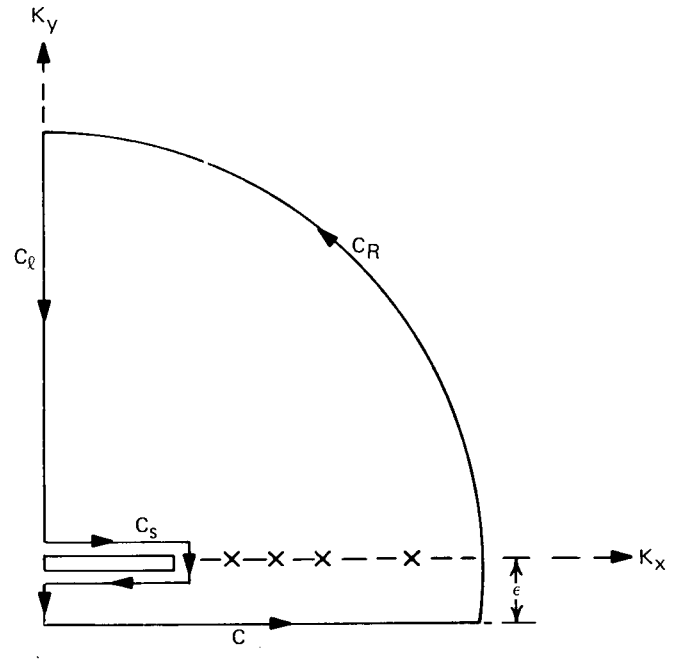

(a) Contour for $\omega > 0$

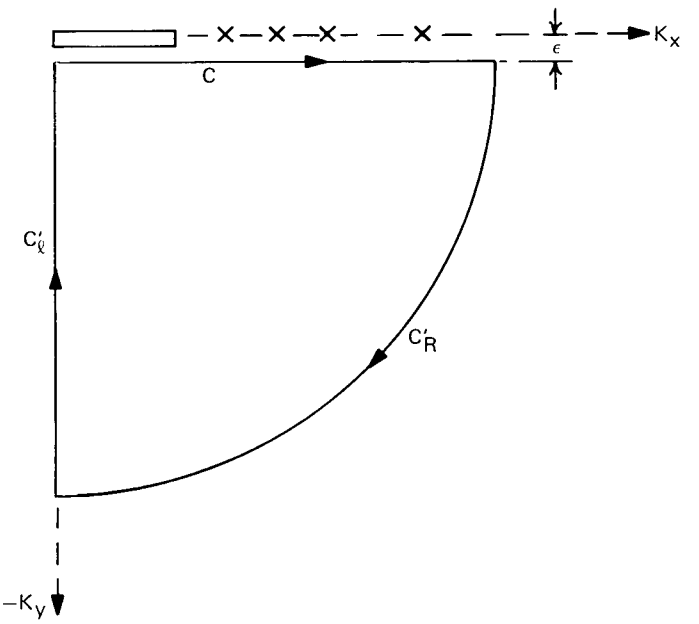

(b) Contour for $\omega < 0$

Fig. 2 — K-plane contours for K integral in Eq. (39). The integral in the text is along the contour C which is displaced an infinitesimal distance ϵ below the K_x axis. Indicated on the K_x axis is a branch cut in the interval $0 \leq K_x \leq N_0/(U \cos \theta)$ as well as poles indicated by x marks.

Similarly to the discussion following Eq. (41), the first integral on the right gives a localized disturbance and is therefore important for the near field. The second term on the right arises from a constant-stratification background (thus the mnemonic significance of the subscript s), and since it involves contributions around the real K_x axis it is potentially important for both the far and near fields. This statement follows from the oscillatory behavior of $\exp(iK\omega)$ as R gets larger. It also applies to the residue contribution, which is the last term on the right in Eq. (42). These terms are clearly wavelike for poles on the K_x axis because they involve contributions proportional to $\exp(iK_\alpha\omega)$. Many of the preceding considerations will be clarified by evaluating Eq. (39) for a model B-V profile in the next section.

The significance of causality is now clear. Its mathematical consequence is that extra wavelike contributions are included for $\omega > 0$ but are absent for $\omega < 0$. These extra contributions appear in the far field to the rear of the hull.

POINT SOURCE IN A MODEL OCEAN ENVIRONMENT

The Model

The model B-V frequency profile is shown in Fig. 1. As indicated in Eqs. (28) and (34), the model is defined as a square-well potential of depth

$$W_\theta = -(N^2 - N_0^2)/(U^2 \cos^2\theta) \equiv -V_\theta \equiv -V/\cos^2\theta \tag{43}$$

amidst a background constant reference potential of

$$W_\theta{}^r = -N_0^2/(U^2 \cos^2\theta) \equiv -V_\theta{}^r \equiv -V^r/\cos^2\theta, \tag{44}$$

where the defined V parameters are positive. We can define our model more completely in terms of these parameters as follows:

$$N^2 = \begin{cases} V^r U^2 & \text{for } -H < z < \infty \quad [\text{Reg. 1}] \\ (V + V^r) U^2 & \text{for } -H - 2A < z < -H \quad [\text{Reg. 2}] \\ V^r U^2 & \text{for } -\infty < z < -H - 2A \quad [\text{Reg. 3}]. \end{cases} \tag{45}$$

In oceanographic parlance, the depth to the thermocline is H, although N^2 has been extended from $z = 0$ to $z = \infty$, and the thermocline width is $2A$. Three regions are distinguished in Eq. (45): above, in, and below the thermocline. Hereafter, we shall let all distances be in units of A (i.e., set $A = 1$). This model is chosen by way of illustration and because the bound and continuum eigenstates associated with Eqs. (28) and (43) are analytically known and simple [13]. There are both even (g) and odd (u) eigenstates with respect to inversion symmetry about the center of the well (at $z = -H - 1$). The odd states change sign under inversion, and the even states retain their sign. The states are as follows:

Odd states

$$u^{(u)}(z + H + 1),$$

where

$$u^{(u)}(-z) = -u^{(u)}(z)$$

$$u_n^{(u)}(z) = \begin{cases} N_n \sin \beta_n z & \text{for } |z| < 1 \\ N_n \sin \beta_n \exp[-k_n(z-1)] & \text{for } z > 1 \end{cases}$$

$$u_k^{(u)}(z) = \begin{cases} N_k \sin pz & \text{for } |z| < 1 \\ N_k \{\sin \rho \cos k(z-1) + (\rho/k) \cos \rho \sin k(z-1)\} & \text{for } z > 1 \end{cases}$$

Even states

$$u_n^{(g)}(z) = \begin{cases} u^{(g)}(z+H+1) \text{ where } u^{(g)}(-z) = u^{(g)}(z) \\ N_n \cos \beta_n z & \text{for } |z| < 1 \\ N_n \cos \beta_n \exp[-k_n(z-1)] & \text{for } z > 1 \end{cases}$$

$$u_k^{(g)}(z) = \begin{cases} N_k \cos \rho z & \text{for } |z| < 1 \\ N_k \{\cos \rho \cos k(z-1) - (\rho/k) \sin \rho \sin k(z-1)\} & \text{for } z > 1 \end{cases}$$

where

$$\begin{aligned} N_n^2 &\equiv [1 + k_n^{-1}]^{-1} \\ \beta_n &\equiv \sqrt{V_\theta - k_n^2} \\ \rho &\equiv \rho(k) \equiv \sqrt{V_\theta + k^2} \\ N_k^2 &\equiv \pi^{-1} [1 + (V_\theta/k^2)\cos^2\rho]^{-1} \\ \beta_n \cot \beta_n &= -k_n \quad \text{for odd states} \\ \beta_n \tan \beta_n &= \quad \text{for even states.} \end{aligned} \tag{46}$$

The k_n values for the bound states are a function of the strength of the potential V_θ, as shown by Fig. 3. As V_θ increases steadily, more and more bound states appear. The nth bound state appears when $\sqrt{V_\theta}$ reaches the value $n\pi/2$. Even states are associated with even values of n ($n = 0, 2, 4, \ldots$), and odd states are associated with odd values of n ($n = 1, 3, 5, \ldots$). It is easily shown from Eq. (46) that

$$k_n \approx \sqrt{n\pi/2}\ \delta \qquad (n \geq 1)$$

and

$$\begin{aligned} k_0 &\approx \delta^2 \\ \sqrt{V_\theta} &= n\pi/2 + \delta \qquad (\delta << 1), \end{aligned} \tag{47}$$

which describes the behavior of k_n near the $\sqrt{V_\theta}$ value at which it appears.

The Particular Solution $\bar{w}_p$ — Point Source Below Thermocline (PSBT)

In Eq. (31), $\bar{w}_p$ is written as the sum of bound and continuum state contributions:

$$\bar{w}_p(z) = \bar{w}_p{}^b + \bar{w}_p{}^c, \tag{48}$$

where $\bar{w}_p{}^b$ is straightforwardly obtained as the sum of even- and odd-state terms. The factor $u_{nz}(z_s)$ is evaluated from the solution in Eq. (46) that applies below the thermocline. This case

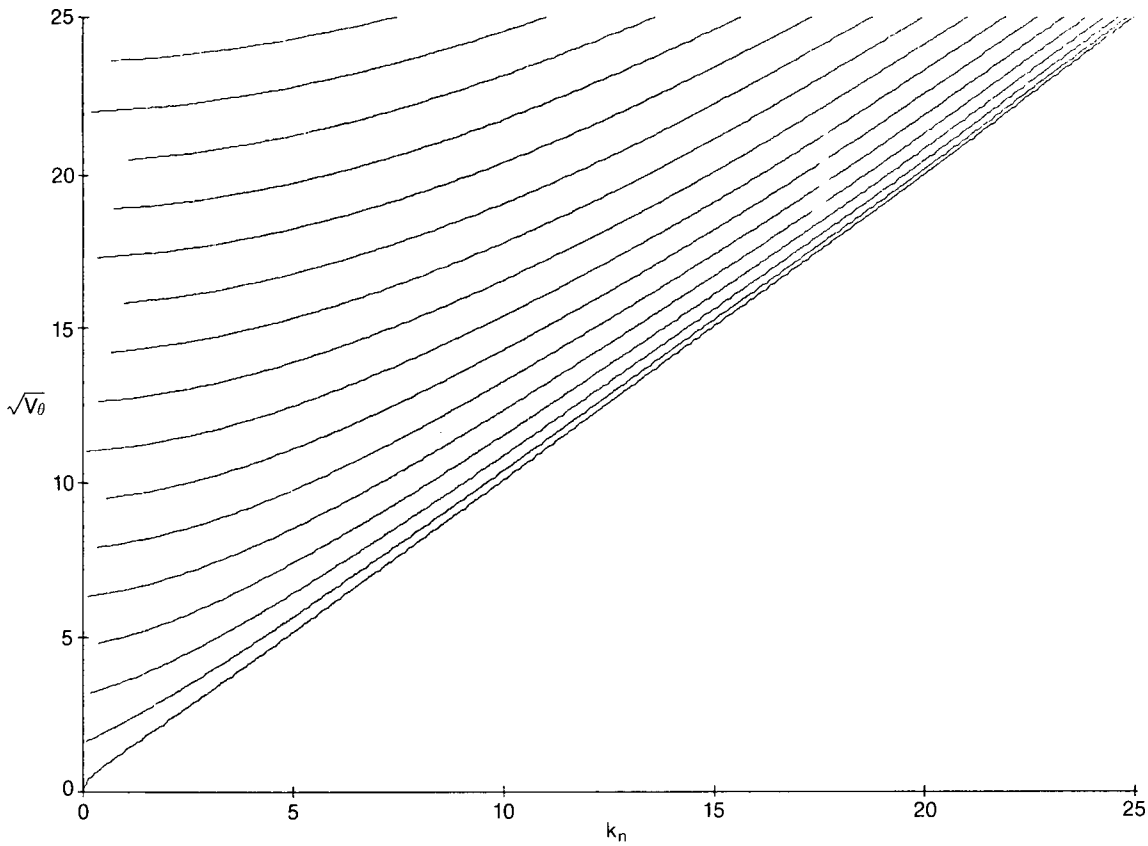

Fig. 3 – Solutions for bound state eigenvalues as a function of the square-well potential strength

will illustrate the method, although results have also been obtained for the point source in and above the thermocline. Accordingly, we let

$$z_s = -d, \qquad \text{where } d = \Delta + H + 2, \tag{49}$$

so that Δ represents the depth of the point source measured from the bottom of the thermocline. The factor $u_n(z)$ in Eq. (31) is evaluated for z above the thermocline, since we are interested in the region near the surface of the ocean. Based on the bound state equations in Eq. (46), the result is

$$\overline{w_p}^b = M\Sigma_n A_n \frac{1}{K_\theta^2 - k_n^2} \exp[-k_n(z + H + \Delta)], \tag{50}$$

where

$$A_n = \pm \frac{k_n^2}{1 + k_n}\left(1 - \frac{k_n^2}{V_\theta}\right) \qquad \begin{matrix}(+\text{for even states}) \\ (-\text{for odd states})\end{matrix}$$

From Eqs. (34) and (44),

$$K_\theta(K) \equiv \sqrt{K^2 - V_\theta{}^r}. \tag{51}$$

Similarly, one obtains

$$\overline{w}_p{}^C = M \int_0^\infty dk \, \frac{\rho}{k^2 + K_\theta{}^2} N_k{}^2 \{F_1 + F_2 + F_3\} \equiv \overline{w}_{p1}{}^C + \overline{w}_{p2}{}^C + \overline{w}_{p3}{}^C$$

where

$$\begin{aligned} F_1 &\equiv \sin 2\rho \cos k\,(z + H + \Delta) \\ F_2 &\equiv (\rho/k) \cos 2\rho \sin k\,(z + H) \cos k\Delta \\ F_3 &\equiv (k/\rho) \cos 2\rho \cos k\,(z + H) \sin k\Delta. \end{aligned} \tag{52}$$

Here, $\overline{w}_{pi}{}^C$ is associated with the F_i term ($i = 1, 2, 3$).

The above expression for $\overline{w}_p{}^C$ can be evaluated by using contour integration techniques and the Residue Theorem, similarly as demonstrated for the homogeneous fluid case in Appendix A. This density-stratified case is clearly a more complicated situation, but not as much as it initially appears. For example, since the integrand is an even function of ρ, no branch cut on the imaginary k axis from $k = 0$ to $k = i\sqrt{V_\theta}$ is called for. The poles that need to be accounted for are at $k = \pm iK_\theta$ in the complex k plane and at the singularities of $N_k{}^2$. The latter are found to occur on the imaginary axis, where $k = i\sigma$, and from Eq. (46);

$$N_{i\sigma}{}^2 = \frac{\sigma^2}{\pi} \frac{1}{\sigma^2 - V_\theta \cos^2 \rho(i\sigma)}$$

where

$$\begin{aligned} \rho(i\sigma) &= \sqrt{V_\theta - \sigma^2} \qquad \text{for } \sigma < \sqrt{V_\theta} \\ &= i\sqrt{\sigma^2 - V_\theta} \qquad \text{for } \sigma > \sqrt{V_\theta}. \end{aligned} \tag{53}$$

There is always a root of the denominator at $\sigma = \sqrt{V_\theta}$. For $\sqrt{V_\theta} < 1$ there is another root at the solution of

$$\sigma/\sqrt{V_\theta} = \cosh \sqrt{\sigma^2 - V_\theta} \qquad (\sqrt{V_\theta} < 1). \tag{54}$$

For $\sqrt{V_\theta} > 1$ there are additional roots $\sigma_{j\pm}$ which satisfy

$$\sigma_{j\pm}/\sqrt{V_\theta} = \pm \cos \sqrt{V_\theta - \sigma_{j\pm}{}^2} \qquad (\sqrt{V_\theta} > 1). \tag{55}$$

The various roots of the denominator in Eq. (53) were calculated and are shown in Fig. 4 For $\sqrt{V_\theta} > 1$ the roots $\sigma_{j\pm}$ are indicated by + or − symbols. We shall henceforth denote the total collection of σ roots shown in Fig. 4 by k_j. Hence, for example, for $\sqrt{V_\theta} < 1$ there are a total of two k_j roots shown in Fig. 4 ($j = 1, 2$).

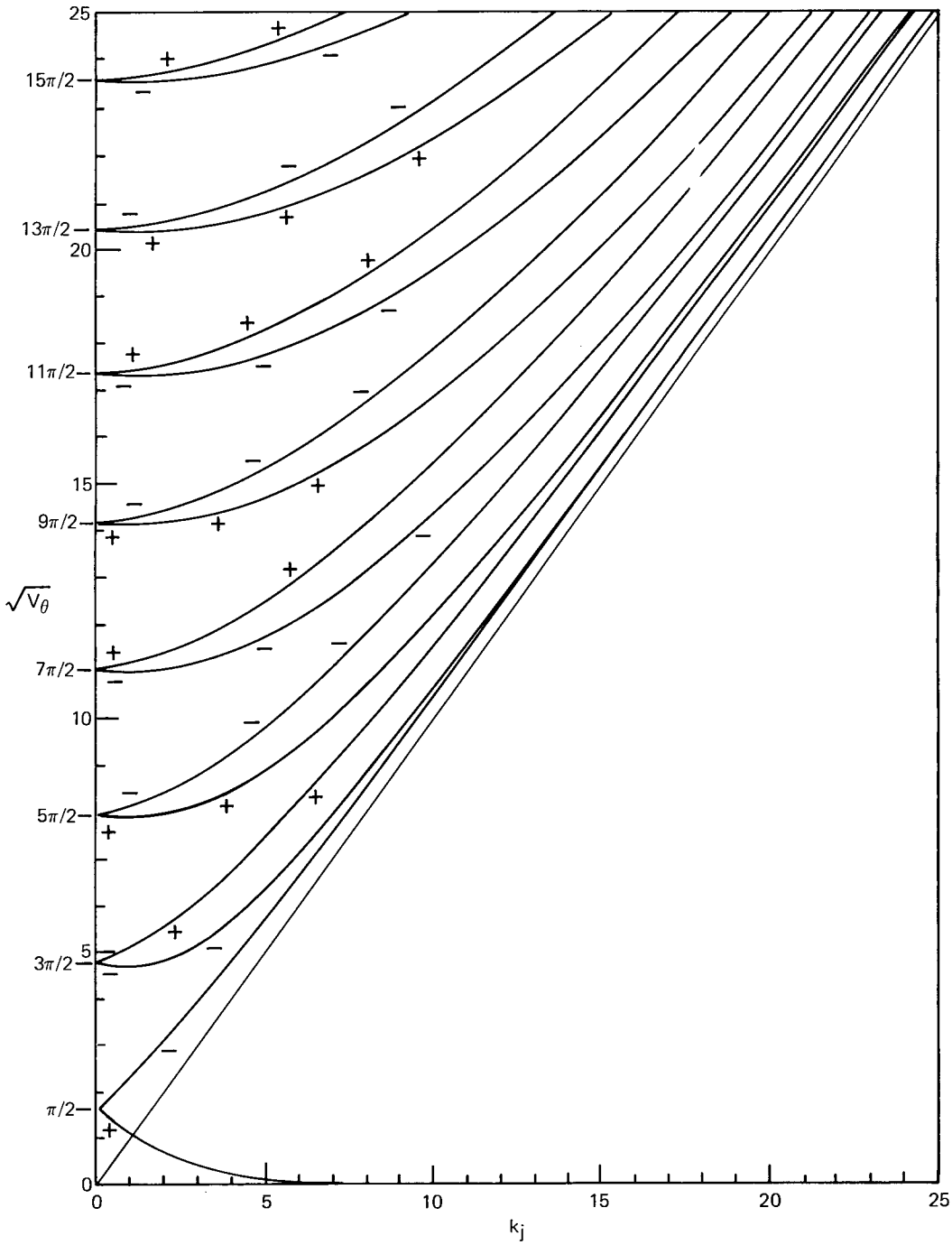

Fig. 4 — Zeros of the denominator in Eq. (53) with $\sigma = k_j$ as a function of the square-well potential strength

In the use of the residue theorem in the evaluation of Eq. (52), we shall need information on the residues associated with the poles of $N_k{}^2$ the complex k plane. We find that

$$\lim_{k \to ik_j} (k - ik_j) N_k{}^2 = -\frac{1}{2\pi i} \frac{k_j}{1 - F_j k_j},$$

where the factor $F_j \equiv F(k_j)$ is given by

$$\begin{aligned} &F(\sqrt{V_\theta}) = \sqrt{V_\theta} \text{ for the root } k_j = \sqrt{V_\theta} && (\sqrt{V_\theta} \neq 1) \\ &F(k_j) = 1 \text{ for solution of Eq. (54)} && (\sqrt{V_\theta} < 1) \\ &F(k_{j\pm}) = \pm \operatorname{sgn}[\sin \rho(ik_{j\pm})] && (\sqrt{V_\theta} > 1) \end{aligned} \tag{56}$$

where

$$\begin{aligned} \operatorname{sgn}[x] \equiv &+1 \text{ if } x > 0 \\ &-1 \text{ if } x < 0 \end{aligned} \tag{57}$$

For $\sqrt{V_\theta} = 1$, the root $k_j = \sqrt{V_\theta}$ becomes a pole of order two which makes no contribution in the residue theorem. We can take care of this by letting $F(1) = \infty$. In Appendix B the term $\bar{w}_{pz}{}^c$ is evaluated for the sake of illustration.

The evaluation of Eq. (52) proceeds as in Appendix B, and the result is

$$\begin{aligned} \bar{w}_p{}^c/M = &C(iK_\theta) e^{-K_\theta(\Delta + z + H)} + \operatorname{sgn}(\Delta - z - H)\, D(iK_\theta) e^{-K_\theta|\Delta - z - H|} \\ &- \Sigma_j \{C_j e^{-k_j(\Delta + z + H)} + \operatorname{sgn}(\Delta - z - H)\, D_j e^{-k_j|\Delta - z - H|}\}, \end{aligned} \tag{58}$$

where

$$\begin{aligned} C(ik) &= \frac{1}{4} \frac{2K\rho(iK) \sin 2\rho(iK) + [K^2 - \rho(iK)^2] \cos 2\rho(iK)}{K^2 - V_\theta \cos^2 \rho(iK)} \\ C_j &= \frac{1}{4} \frac{2k_j\, \rho(ik_j) \sin 2\rho(ik_j) + [k_j{}^2 - \rho(ik_j)^2] \cos 2\rho(ik_j)}{(K_\theta{}^2 - k_j{}^2)(1 - F_j k_j)} \\ D(iK) &= \frac{1}{4} \frac{V_\theta \cos 2\rho(iK)}{K^2 - V_\theta \cos^2 \rho(iK)} \\ D_j &= \frac{1}{4} \frac{V_\theta \cos 2\rho(ik_j)}{(K_\theta{}^2 - k_j{}^2)(1 - F_j k_j)} \end{aligned} \tag{59}$$

This completes the evaluation of $\bar{w}_p(z)$ in Eq. (48).

Full Solution $\bar{w}$ (PSBT)

To the particular solution just found we must add a solution of the homogeneous equation

$$\bar{w}_{IIzz} - W_\theta(z)\, \bar{w}_{II} - K_\theta{}^2 \bar{w}_{II} = 0, \tag{60}$$

in order to satisfy the boundary conditions, where $W_\theta(z)$ is the square-well potential which is zero outside and $-V_\theta$ inside the well (see Eq. (43)). The solution is found by demanding continuity of $\bar{w}_{II}$ and $\bar{w}_{IIz}$ across the square-well boundaries, along with the condition that $\bar{w}_{II}$ vanishes at $z = -\infty$. It is

$$\bar{w}_{II}(z) = \begin{cases} \frac{1}{2}Ae^{-2K_\theta}\left\{[2\cos 2\rho(iK_\theta) + \left(\frac{K_\theta}{\rho(iK_\theta)} - \frac{\rho(iK_\theta)}{K_\theta}\right)\sin 2\rho(iK_\theta)]e^{K_\theta z}\right\} & (z > -H) \\ \quad + \left(\frac{K_\theta}{\rho(iK_\theta)} + \frac{\rho(iK_\theta)}{K_\theta}\right)\sin 2\rho(iK_\theta)e^{-K_\theta(z+2H)} & [\text{Reg. 1}] \\ Ae^{-K_\theta(2+H)}\left\{\frac{K_\theta}{\rho(iK_\theta)}\sin[\rho(iK_\theta)(2+H+z)]\right. & (-2-H < z < -H) \\ \quad \left. + \cos[\rho(iK_\theta)(2+H+z)]\right\} & [\text{Reg. 2}] \\ Ae^{K_\theta z} & (z < -2-H) \\ & [\text{Reg. 3}] \end{cases}$$

The form $Ae^{-K_\theta z}$ in (region) Reg. 3 is rejected as a possible solution because it does not vanish at $z = -\infty$ for K which is to be regarded as displaced by a very small amount beneath the real K axis (see footnote in Appendix B). The constant A is adjusted to satisfy the free-surface boundary condition in Eq. (37), for which we need the Reg. 1 solution in Eq. (61). The details of this are somewhat tedious but completely straightforward, and the full solution for the observation point in Reg. 1 and the point source in Reg. 3 is

$$\begin{aligned} \bar{w}(K_\theta, \theta, z)/M = \Sigma_n \frac{A_n e^{-k_n(H+\Delta)}}{K_\theta^2 - k_n^2}[e^{-k_n z} + (k_n + K_0 \sec^2\theta) \\ \times F(iK_\theta, z)] + C(iK_\theta)e^{-K_\theta(H+\Delta)} \\ \times [e^{-K_\theta z} + (K_\theta + K_0 \sec^2\theta) F(iK_\theta, z)] \\ - \Sigma_j C_j e^{-k_j(H+\Delta)} [e^{-k_j z} + (k_j + K_0 \sec^2\theta) \\ \times F(iK_\theta, z)] + D(iK_\theta) [\text{sgn}(\Delta - z - H) \\ \times e^{-K_\theta|\Delta - z - H|} - (K_\theta - \text{sgn}(\Delta - H) K_0 \sec^2\theta) \\ \times e^{-K_\theta|\Delta - H|} F(iK_\theta, z)] - \Sigma_j D_j \\ \times [\text{sgn}(\Delta - z - H) e^{-k_j|\Delta - z - H|} - (k_j - \text{sgn}(\Delta - H) \\ \times K_0 \sec^2\theta) e^{-k_j|\Delta - H|} F(iK_\theta, z)], \end{aligned} \tag{62}$$

where we have defined the subsidiary function

$$F(iK, z) \equiv [S(iK)]^{-1}[P(iK)e^{Kz} + Q(iK)e^{-K(z+2H)}],$$

with

$$\begin{aligned} P(iK) &\equiv 2\cos 2\rho(iK) + \left[\frac{K}{\rho(iK)} - \frac{\rho(iK)}{K}\right]\sin 2\rho(iK) \\ Q(iK) &\equiv \left[\frac{K}{\rho(iK)} + \frac{\rho(iK)}{K}\right]\sin 2\rho(iK) \\ S(iK) &\equiv (K - K_0 \sec^2\theta) P(iK) - (K + K_0 \sec^2\theta) Q(iK)e^{-2KH}. \end{aligned} \tag{63}$$

The parameter A_n has already been defined in Eq. (50); C, C_j, D, and D_j have been defined in Eq. (59). Some care is in order to distinguish between K_θ, defined in Eq. (51), and K_0, defined in Eq. (27). One must also distinguish the bound state values k_n from the singular points k_j of the eigenfunction normalization parameters.

Expressions have also been found for the observation point in Reg. 1 and the point source in Reg. 1 or Reg. 2. These are available upon request.

Evaluation of w (PSBT)

As indicated by Eqs. (38)-(42) contour integration techniques can be used to separate localized and wavelike contributions from the point source. Of great interest are the positions of the poles in the complex K plane. From Eq. (62) it is clear that there are poles associated with the bound-state eigenvalues, and for the contours of interest (see Fig. 2) these occur at

$$K = K_n \equiv \sqrt{k_n{}^2 + V_\theta{}^r} \qquad \text{(poles)}$$

Poles of interest also occur at solutions of

$$S(iK_\theta) = 0 \qquad \text{(poles)}.$$

It might be thought that poles would also be associated with C, C_j, D, and D_j coefficients (see Eq. (59)), but it is easily shown that the singularities of C are canceled by the singularities of the C_j coefficients, and similarly for D and D_j coefficients.

To advance further in the discussion, we would like to know how to analytically continue $\overline{w}$ into the complex K plane, and, in particular, to various parts of the contours shown in Fig. 2. The central part of this problem is the analytic continuation of $\rho(iK_\theta)$ and K_θ which appear in the arguments of functions contained in Eq. (62). These entities can be written from their definitions in Eqs. (46) and (51) as

$$K_\theta \equiv \sqrt{K^2 - V_\theta{}^r}$$

$$\rho(iK_\theta) \equiv \sqrt{V_\theta + V_\theta{}^r - K^2} \equiv i\sqrt{K^2 - (V_\theta + V_\theta{}^r)}\,.$$

The generic problem is the analytic continuation of a function

$$f(z) \equiv \sqrt{z^2 - a^2} \quad (z = x + iy)$$

in the complex z plane. Here a is real. This is handled in various texts [14] and in Appendix C. The results of Appendix C are straightforwardly applied to K_θ and $\rho(iK_\theta)$ and the functions in which they appear as arguments.

We return now to the condition (see Eq. (63)) that

$$S(iK_\theta) = 0 = [P(iK_\theta) - Q(iK_\theta)e^{-2K_\theta H}]K_\theta - [P(iK_\theta) + Q(iK_\theta)e^{-2K_\theta H}]K_0 \sec^2\theta. \qquad (64)$$

Its homogeneous fluid counterpart solution corresponds to the pole at $K = K_0 \sec^2\theta$ which gives rise to the Kelvin wake [2], where $K_0 = g/U^2$ if surface tension is ignored. If we hypothesize a solution near this value for our case, we find without too much trouble that, since

$$g >> N^2 \Longrightarrow K_0 \sec^2\theta >> V_\theta, V_\theta^r$$

(where g is expressed in units of A/sec^2), we have

$$P(iK_\theta) \approx 2e^{2K} \qquad \text{and} \qquad Q(iK_\theta) \approx 0.$$

Then $K = K_0 \sec^2\theta$ is a solution of Eq. (64) to a very good approximation. The assumption that the surface tension part of K_0 in Eq. (27) can be ignored could be argued as follows. It is well known that surface tension is comparable with gravity effects only when the wavelength ($\approx 2\pi/K$) gets to be around a few centimeters. But the disturbance should be concentrated mainly in wavelengths on the order of the hull characteristic length or depth, whichever is larger. These wavelengths are much larger than a few centimeters, so that the surface tension correction in Eq. (27) is relatively negligible. The detailed effects of surface tension are, however, relatively unknown. Their most dramatic effect appears to be in the solution of Eq. (64), which can be rewritten to a good approximation as

$$K - K_0 \sec^2\theta = 0, \tag{65}$$

where K_0 is given by Eq. (27). Since K_0 is a function of K now, the solution of Eq. (65) is easily found to be

$$K = K_+ \text{ and } K_- \qquad \text{(poles)},$$

where

$$K_\pm = \frac{\rho U^2}{2T}\cos^2\theta \pm \sqrt{\frac{\rho^2 U^4}{4T^2}\cos^4\theta - \frac{\rho g}{T}}\,. \tag{66}$$

Here,

$$\rho \approx 1 \text{ gm/cm}^3$$
$$g = 980 \text{ cm/sec}^2$$

and

$$T \approx 72.5 \text{ erg/cm}^2.$$

For the first term under the radical sign dominant over the second,

$$K_+ \approx \frac{\rho U^2}{T}\cos^2\theta; \qquad K_- \approx \frac{g}{U^2}\sec^2\theta. \tag{67}$$

Under these circumstances K_+ corresponds to the surface-tension effects and K_- corresponds to the gravity effects, so that neglect of surface tension corresponds to throwing out K_+ and keeping K_- in the approximation of Eq. (67). Significant surface-tension effects occur when the two terms under the radical in Eq. (66) cancel. As a consequence,

$$K_{\pm} = \frac{\rho U^2}{2T} \cos^2\theta$$

when

$$\cos\theta = \frac{1}{U}\left(\frac{4Tg}{\rho}\right)^{1/4}. \tag{68}$$

A larger portion of the θ integration is involved in this condition for smaller velocities. For example, when $U = 20$ knots, $\theta = 88.7°$ in Eq. (68), but when $U = 1$ knot, $\theta = 63.3°$. Evidently, then, smaller velocities lead to more prominent surface-tension effects. In the expressions we shall derive, we shall neglect surface-tension effects, for simplicity and in accordance with precedent. This corresponds to letting $T = 0$ in Eq. (27), so that K_0 is simply a constant parameter. Surface-tension effects can be included at some future time, perhaps with the help of the above considerations.

We are in a position now to write down the expressions for w in Eq. (39), using the discussion of Eqs. (38)-(42) as a guide. We have

$$w = (2\pi)^{-2}\left(\int_{-\pi/2}^{-\pi/2+\delta} d\theta + \int_{-\pi/2+\delta}^{\pi/2} d\theta\right)\int_C dK\, K\overline{W}(K_\theta, \theta, z)e^{iK\omega} + c.c.$$

$$\equiv w^{(b)} + w^{(a)} \tag{69}$$

where $w^{(b)}$ is evaluated with the use of the contour in Fig. 2b and $w^{(a)}$ is evaluated with the use of the contour in Fig. 2a. Schematically,

$$w^{(b)} = \int_C dK \ldots = -\int_{C_{\mathscr{L}'}} dK \ldots = w_{\mathscr{L}}^{(b)},$$

where

$$w_{\mathscr{L}}^{(b)} = -(2\pi)^{-2}\int_{-\pi/2}^{-\pi/2+\delta} d\theta \int_0^\infty dm\, m\, \overline{W}(-i\sqrt{m^2 + V_\theta{}^r}, \theta, z)e^{m\omega} + c.c. \tag{70}$$

On the other hand,

$$w^{(a)} = \int_C dK \ldots = -\int_{C_{\mathscr{L}}} dK \ldots - \int_{C_s} dK \ldots + [2\pi i\mathscr{R}(\text{poles})] + c.c.$$

$$= \qquad w_{\mathscr{L}}^{(a)} \qquad + w_s \qquad + w_r,$$

where

$$w_{\ell}^{(a)} = -(2\pi)^{-2}\int_{-\pi/2+\delta}^{\pi/2} d\theta \int_0^{\infty} dm\ m\ \overline{W}(i\sqrt{m^2+V_\theta{}^r},\ \theta,\ z)e^{-m\omega} + c.c.$$

$$w_s = (2\pi)^{-2}\int_{-\pi/2+\delta}^{\pi/2} d\theta \int_0^{\sqrt{V_\theta{}^r}} dK\ K[\overline{W}(-i\sqrt{V_\theta{}^r - K^2},\ \theta,\ z) - \overline{W}(i\sqrt{V_\theta{}^r - K^2},\ \theta,\ z)] \times e^{iK\omega} + c.c.$$

$$w_r = -\pi^{-1}\int_{-\pi/2+\delta}^{\pi/2} d\theta\ \mathrm{Im}[\Sigma_n \mathscr{R}(\sqrt{k_n{}^2 + V_\theta{}^r}) + \mathscr{R}(K_0 \sec^2\theta)]. \tag{71}$$

Here $\mathscr{R}(K_n)$ is the residue of the integrand $K\overline{W}(K_\theta,\ \theta,\ z)\exp(iK\omega)$ at the pole at $K = K_n$. These expressions are straightforwardly found from Eq. (62):

$$w = w_B + w_C,$$

where

$$\begin{aligned} w_B &= w_{B\ell} + w_{Bs} + w_{Br} \\ w_C &= w_{C\ell} + w_{Cs} + w_{Cr} \end{aligned} \tag{72}$$

This separates $w(R, \delta, z)$ into bound state B and continuum state C contributions, and the latter are, in turn, subdivided into localized ℓ, stratification s, and residue r contributions as in Eqs. (70) and (71). Before we give these expressions in detail it will be convenient to define

$$F'(m, z) \equiv \mathrm{Re}\,F(m, z) \text{ and } F''(m, z) \equiv \mathrm{Im}\,F(m, z), \tag{73a}$$

where, from Eq. (63),

$$\begin{aligned} F'(m, z) = &-\frac{K_0 \sec^2\theta}{SS^*}\left\{\left[4\cos^2 2\rho + 2\left(\frac{\rho^2}{m^2} + \frac{m^2}{\rho^2}\right)\sin^2 2\rho\right]\cos mz\right. \\ &\left. - 2\left(\frac{\rho^2}{m^2} - \frac{m^2}{\rho^2}\right)\sin^2 2\rho \cos m(z+2H) - 4\left(\frac{\rho}{m} - \frac{m}{\rho}\right)\sin 2\rho \cos 2\rho \sin m(z+2H)\right\} \\ &+ \frac{m}{SS^*}\left\{\left[4\cos^2 2\rho + 2\left(\frac{\rho^2}{m^2} + \frac{m^2}{\rho^2}\right)\sin^2 2\rho\right]\sin mz\right. \\ &\left. + 2\left(\frac{\rho^2}{m^2} - \frac{m^2}{\rho^2}\right)\sin^2 2\rho \sin m(z+2H) - 4\left(\frac{\rho}{m} - \frac{m}{\rho}\right)\sin 2\rho \cos 2\rho \cos m(z+2H)\right\} \end{aligned}$$

$$F''(m, z) = (1/SS^*)\ (4K_0 \sec^2\theta \sin mz + 4m \cos mz), \tag{73b}$$

where

$$SS^* \equiv S(m)\, S(m)^*$$

$$= K_0^2 \sec^4\theta \left[4\cos^2 2\rho + 2\left(\frac{\rho^2}{m^2}+\frac{m^2}{\rho^2}\right)\sin^2 2\rho - 2\left(\frac{\rho^2}{m^2}-\frac{m^2}{\rho^2}\right)\sin^2 2\rho \cos 2mH \right.$$

$$\left. - 4\left(\frac{\rho}{m}-\frac{m}{\rho}\right)\sin 2\rho \cos 2\rho \sin 2mH\right]$$

$$+ m^2\left[4\cos^2 2\rho + 2\left(\frac{\rho^2}{m^2}+\frac{m^2}{\rho^2}\right)\sin^2 2\rho + 2\left(\frac{\rho^2}{m^2}-\frac{m^2}{\rho^2}\right)\sin^2 2\rho \cos 2mH \right.$$

$$\left. + 4\left(\frac{\rho}{m}-\frac{m}{\rho}\right)\sin 2\rho \cos 2\rho \sin 2mH\right]$$

$$- 4mK_0 \sec^2\theta \left[\left(\frac{\rho^2}{m^2}-\frac{m^2}{\rho^2}\right)\sin^2 2\rho \sin 2mH \right.$$

$$\left. - 2\left(\frac{\rho}{m}-\frac{m}{\rho}\right)\sin 2\rho \cos 2\rho \cos 2mH\right]. \tag{73c}$$

Here, from Eq. (46),

$$\rho \equiv \rho(m) = \sqrt{m^2 + V_\theta} \tag{73d}$$

By changing variables to $\theta' = \theta + \pi$ in Eq. (70), we find that

$$w_{Bl} = \frac{M}{2\pi^2}\int_{-\pi/2+\delta}^{\pi/2+\delta} d\theta \int_0^\infty dm e^{-m\omega} m \Sigma_n \frac{A_n e^{-k_n(H+\Delta)}}{m_\theta^2 + k_n^2}\{\quad\},$$

where

$$\{\quad\} \equiv e^{-k_n z} + K_0 \sec^2\theta\, F'(m_\theta, z), \tag{74}$$

with

$$m_\theta \equiv \sqrt{m^2 + V_\theta r}. \tag{75}$$

Similarly,

$$w_{Cl} = -\frac{M}{2\pi^2}\int_{-\pi/2+\delta}^{\pi/2+\delta} d\theta \int_0^\infty dm e^{-m\omega} m\{\mathrm{Re}\, C(\quad) - \Sigma_j\, \mathrm{Re}\, C_j(\quad) + \mathrm{Re}\, D(\quad) - \Sigma_j\, \mathrm{Re}\, D_j(\quad)\}. \tag{76a}$$

Here, from Eqs. (59) and (62),

$$\begin{aligned}\text{Re } C(\quad) = {} & C' \cos m_\theta(\Delta + H + z) - C'' \sin m_\theta(\Delta + H + z) \\ & + (C'F' - C''F'')\,[\cos m_\theta(\Delta + H)K_0 \sec^2\theta + m_\theta \sin m_\theta(\Delta + H)] \\ & + (C'F'' + C''F')\,[m_\theta \cos m_\theta(\Delta + H) - \sin m_\theta(\Delta + H)K_0 \sec^2\theta]\,. \end{aligned} \tag{76b}$$

In Eq. (76b),

$$C' \equiv \text{Re } C(-im_\theta) = \frac{1}{4}\frac{(m_\theta^2 + \rho^2)\cos 2\rho}{m_\theta^2 + V_\theta \cos^2\rho}$$

$$C'' \equiv \text{Im } C(-im_\theta) = \frac{1}{2}\frac{m_\theta \rho \sin 2\rho}{m_\theta^2 + V_\theta \cos^2\rho}$$

$$\text{Re } C_j(\quad) = C_j e^{-k_j(\Delta+H)}[e^{-k_j z} + (k_j + K_0 \sec^2\theta)F']\,,$$

where

$$C_j = -\frac{1}{4}\frac{(2k_j^2 - V_\theta)\cos 2\rho(ik_j) + 2k_j\rho(ik_j)\sin 2\rho(ik_j)}{(m_\theta^2 + k_j^2)\,(1 - F_j k_j)}\,, \tag{76c}$$

$$\begin{aligned}\text{Re } D(\quad) = {} & D\{\text{sgn}(\Delta - z - H)\cos m_\theta|\Delta - z - H| \\ & + F'[\text{sgn}(\Delta - H)K_0 \sec^2\theta \cos m_\theta|\Delta - H| - m_\theta \sin m_\theta|\Delta - H|] \\ & - F''[\text{sgn}(\Delta - H)K_0 \sec^2\theta \sin m_\theta|\Delta - H| + m_\theta \cos m_\theta|\Delta - H|]\} \end{aligned} \tag{76d}$$

where

$$D = D(-im_\theta) = -\frac{1}{4}\frac{V_\theta \cos 2\rho}{m_\theta^2 + V_\theta \cos^2\rho}\,,$$

$$\begin{aligned}\text{Re } D_j(\quad) = {} & D_j\{\text{sgn}(\Delta - z - H)e^{-k_j|\Delta - z - H|} \\ & - [k_j - \text{sgn}(\Delta - H)K_0 \sec^2\theta]\,e^{-k_j|\Delta - H|}F'\}\,, \end{aligned} \tag{76e}$$

where

$$D_j = -\frac{1}{4}\frac{V_\theta \cos 2\rho(ik_j)}{(m_\theta^2 + k_j^2)\,(1 - F_j k_j)}\,;$$

and we have used the abbreviations

$$\rho \equiv \rho(m_\theta), \qquad F' \equiv F'(m_\theta, z), \qquad F'' = F''(m_\theta, z). \tag{76f}$$

It is also straightforward (and tedious) to find the stratification terms. The result is

$$w_{Bs} = -\frac{M}{\pi^2}\int_{-\pi/2+\delta}^{\pi/2} d\theta\, K_0 \sec^2\theta \int_0^{\sqrt{V_\theta r}} dK \sin K\omega\, KF''(\sqrt{V_\theta r - K^2}, z)\Sigma_n\{\quad\}_n, \tag{77}$$

where

$$\{\quad\}_n = A_n e^{-k_n(H+\Delta)}/(K_\theta^2 - k_n^2),$$

and

$$w_{Cs} = -\frac{M}{\pi^2}\int_{-\pi/2+\delta}^{\pi/2} d\theta \int_0^{\sqrt{V_\theta r}} dK \sin K\omega\, K\{C'[\ ] - C''[\ ] - \Sigma_j C_j[\ ] + D[\ ] - \Sigma_j D_j[\ ]\}. \tag{78a}$$

Here,

$$C'[\ ] = C'\{\sin\sqrt{V_\theta r - K^2}\,(\Delta+H+z) + \cos\sqrt{V_\theta r - K^2}\,(\Delta+H)\,[K_0\sec^2\theta F'' - \sqrt{V_\theta r - K^2}\,F'] + \sin\sqrt{V_\theta r - K^2}\,(\Delta+H)\,[K_0\sec^2\theta F' + \sqrt{V_\theta r - K^2}\,F'']\} \tag{78b}$$

where

$$C' \equiv \mathrm{Re}\,C(-i\sqrt{V_\theta r - K^2}) = (2K_\theta^2 - V_\theta)\cos 2\rho(\sqrt{V_\theta r - K^2})/\{4\,[K_\theta^2 - V_\theta\cos^2\rho(\sqrt{V_\theta r - K^2})]\};$$

$$C''[\ ] = C''\{\cos\sqrt{V_\theta r - K^2}\,(\Delta+H+z) + \cos\sqrt{V_\theta r - K^2}\,(\Delta+H)\,[K_0\sec^2\theta F' + \sqrt{V_\theta r - K^2}F''] - \sin\sqrt{V_\theta r - K^2}\,(\Delta+H)\,[K_0\sec^2\theta F'' - \sqrt{V_\theta r - K^2}F']\}, \tag{78c}$$

where

$$C'' \equiv -\mathrm{Im}\,C(-i\sqrt{V_\theta r - K^2}) = \sqrt{V_\theta r - K^2}\;\rho(\sqrt{V_\theta r - K^2})\sin 2\rho(\sqrt{V_\theta r - K^2})/\{2[K_\theta^2 - V_\theta\cos^2\rho(\sqrt{V_\theta r - K^2})]\};$$

$$C_j[\ ] = C_j\, e^{-k_j(\Delta+H)}(k_j + K_0\sec^2\theta)F'', \tag{78d}$$

where

$$C_j = [(2k_j^2 - V_\theta)\cos 2\rho(ik_j) + 2k_j\;\rho(ik_j)\sin 2\rho(ik_j)]/[4(K_\theta^2 - k_j^2)(1 - F_j k_j)];$$

$$D[\ ] = D\{\mathrm{sgn}(\Delta - z - H)\sin\sqrt{V_\theta r - K^2}\,|\Delta - z - H| + F''[\mathrm{sgn}(\Delta - H)\,K_0\sec^2\theta\cos\sqrt{V_\theta r - K^2}\,|\Delta - H| - \sqrt{V_\theta r - K^2}\sin\sqrt{V_\theta r - K^2}\,|\Delta - H|] + F'\,[\sqrt{V_\theta r - K^2}\cos\sqrt{V_\theta r - K^2}\,|\Delta - H| + \mathrm{sgn}\,(\Delta - H)\,K_0\sec^2\theta\sin\sqrt{V_\theta r - K^2}\,|\Delta - H|]\},$$

where

$$D = V_\theta\cos 2\rho\,(\sqrt{V_\theta r - K^2})/\{4[K_\theta^2 - V_\theta\cos^2\rho(\sqrt{V_\theta r - K^2})]\}; \tag{78e}$$

$$D_j[\ ] = D_j\,[k_j - \mathrm{sgn}\,(\Delta - H)\,K_0\sec^2\theta]\,e^{-k_j|\Delta - H|}F'', \tag{78f}$$

where

$$D_j = V_\theta\cos 2\rho(ik_j)/[4(K_\theta^2 - k_j^2)(1 - F_j k_j)];$$

we have used the abbreviations

$$\begin{aligned} F' &\equiv F'(\sqrt{V_\theta{}^r - K^2},\, z), \\ F'' &\equiv F''(\sqrt{V_\theta{}^r - K^2},\, z), \\ \rho(\sqrt{V_\theta{}^r - K^2}) &= \sqrt{V_\theta + V_\theta{}^r - K^2}. \end{aligned} \tag{78g}$$

The residue terms are found to be

$$w_{Br} = -\frac{M}{\pi}\int_{-\pi/2+\delta}^{\pi/2} d\theta\, \Sigma_n A_n e^{-k_n(H+\Delta)}\{\quad\},$$

where

$$\{\quad\} \equiv \frac{1}{2}\sin\sqrt{k_n{}^2 + V_\theta{}^r}\,\omega[e^{-k_n z} + K_0\sec^2\theta\, F(ik_n)] + \sin(K_0\sec^2\theta\,\omega)\, e^{(K_0\sec^2\theta)z}. \tag{79}$$

$$w_{Cr} = -\frac{M}{\pi}\int_{-\pi/2+\delta}^{\pi/2} d\theta\, K_0\sec^2\theta\sin(K_0\sec^2\theta\,\omega)\,\{C[\quad] - \Sigma_j C_j[\quad] - D[\quad] + \Sigma_j D_j[\quad]\}. \tag{80a}$$

Here,

$$C[\quad] = Ce^{-K_0\sec^2\theta(\Delta+H)}2K_0\sec^2\theta\, e^{(K_0\sec^2\theta)z},$$

where

$$C \equiv C(iK_0\sec^2\theta) \approx \frac{1}{4}\frac{2K_0{}^2\sec^4\theta\, e^{-2K_0\sec^2\theta} + \frac{1}{4}\left(\frac{V_\theta}{K_0\sec^2\theta}\right)^2\sinh(2K_0\sec^2\theta)}{K_0{}^2\sec^4\theta - V_\theta\cosh^2(K_0\sec^2\theta)}; \tag{80b}$$

$$C_j[\quad] = C_j e^{-k_j(\Delta+H)}\,(k_j + K_0\sec^2\theta)\, e^{(K_0\sec^2\theta)z},$$

where

$$C_j = \frac{1}{4}\frac{2k_j\rho(ik_j)\sin 2\rho(ik_j) + [k_j{}^2 - \rho(ik_j)^2]\cos 2\rho(ik_j)}{(K_0{}^2\sec^4\theta - k_j{}^2)\,(1 - F_j k_j)}; \tag{80c}$$

$$D[\quad] = D\,K_0\sec^2\theta[1 - \mathrm{sgn}(\Delta - H)]\, e^{-K_0\sec^2\theta|\Delta-H|}e^{(K_0\sec^2\theta)z}, \tag{80d}$$

where

$$D = D(iK_0\sec^2\theta) = \frac{1}{4}\frac{V_\theta\cosh(2K_0\sec^2\theta)}{K_0{}^2\sec^4\theta - V_\theta\cosh^2(K_0\sec^2\theta)};$$

and

$$D_j[\quad] = D_j[k_j - \mathrm{sgn}(\Delta - H)K_0\sec^2\theta]\, e^{-k_j|\Delta-H|}\, e^{(K_0\sec^2\theta)z},$$

where

$$D_j = \frac{1}{4} \frac{V_\theta \cos 2\rho(ik_j)}{(K_0^2 \sec^4 \theta - k_j^2)(1 - F_j k_j)}. \tag{80e}$$

Expressions for the point source in the thermocline are available upon request. We have discussed the effect of surface tension on w_r. The effect on w_ℓ and w_s is included simply by substituting Eq. (27) for $K_0(K)$, with $K = -im_\theta$ in w_ℓ and $K = -i\sqrt{V_\theta{}^r - K^2}$ in w_s.

Surface Displacement ζ (PSBT)

From Eq. (14) one obtains surface displacement by evaluating (undisplaced surface level at $z = 0$)

$$\zeta = U^{-1} \int_{-\infty}^{x} dx\ w(xyz)|_{z=0}. \tag{81}$$

This is very simply done from Eqs. (72)-(80), and if we denote

$$F(m) \equiv F(m, z)|_{z=0} \equiv F'(m) + iF''(m) \tag{82}$$

in Eq. (73), the results are

$$\zeta_{B\ell} = -\frac{M}{2\pi^2 U} \int_{-\pi/2+\delta}^{\pi/2+\delta} d\theta \sec\theta \int_0^\infty dm\ e^{-m\omega}[1 + K_0 \sec^2\theta\ F'(m_\theta)] \Sigma_n \{\ \}_n,$$

where

$$\{\ \}_n = A_n e^{-k_n(H+\Delta)}/(m_\theta^2 + k_n^2); \tag{83}$$

$$\zeta_{C\ell} = \frac{M}{2\pi^2 U} \int_{-\pi/2+\delta}^{\pi/2+\delta} d\theta \sec\theta \int_0^\infty dm\ e^{-m\omega}\{\mathrm{Re}\, C(\ ) - \Sigma_j\, \mathrm{Re}\, C_j(\ ) + \mathrm{Re}\, D(\ ) - \Sigma_j\, \mathrm{Re}\, D_j(\ )\}; \tag{84}$$

$$\zeta_{Bs} = \frac{M}{\pi^2 U} \int_{-\pi/2+\delta}^{\pi/2} d\theta\, K_0 \sec^3\theta \int_0^{\sqrt{V_\theta{}^r}} dK \cos(K\omega) F''(\sqrt{V_\theta{}^r - K^2}\ \Sigma_n A_n e^{-k_n(H+\Delta)}/(K_\theta^2 - k_n^2); \tag{85}$$

$$\zeta_{Cs} = \frac{M}{\pi^2 U} \int_{-\pi/2+\delta}^{\pi/2} d\theta \sec\theta \int_0^{\sqrt{V_\theta{}^r}} dK \cos(K\omega)\{C'[\ ] - C''[\ ] - \Sigma_j C_j[\ ] + D[\ ] - \Sigma_j D_j[\ ]\}; \tag{86}$$

$$\zeta_{Br} = \frac{M}{\pi U} \int_{-\pi/2+\delta}^{\pi/2} d\theta \sec\theta\ \Sigma_n A_n e^{-k_n(H+\Delta)}\ \{\ \}_n,$$

where

$$\{\quad\} \equiv \frac{1}{2\sqrt{k_n{}^2 + V_\theta{}^r}} \cos\left(\sqrt{k_n{}^2 + V_\theta{}^r}\,\omega\right)\left[1 + K_0 \sec^2\theta\, F(ik_n)\right] + (K_0 \sec^2\theta)^{-1} \cos\left(K_0 \sec^2\theta\,\omega\right); \tag{87}$$

and

$$\zeta_{Cr} = \frac{M}{\pi U}\int_{-\pi/2+\delta}^{\pi/2} d\theta \sec\theta \cos\left(K_0 \sec^2\theta\,\omega\right)\{C[\quad] - \Sigma_j C_j[\quad] - D[\quad] + \Sigma_j D_j[\quad]\}, \tag{88}$$

in which the parameters are exactly those listed for the w counterparts in the evaluation of w. They are to be evaluated at $z = 0$, which is a very simple task.

Surface Rate of Strain S (PSBT)

From Eq. (9) one can define

$$S \equiv -\frac{\partial w}{\partial z}\bigg|_{z=0} = \left[\frac{\partial u}{\partial x} + \frac{\partial v}{\partial y}\right]\bigg|_{z=0} (\sec^{-1}), \tag{89}$$

so that the parameter S is considered to be a measure of the rate of straining of the surface. The z partial differentiation is easily applied to the expressions for w, and so the counterpart expressions for S involve the function

$$G(m) \equiv \frac{\partial}{\partial z} F(m, z)\big|_{z=0} = G'(m) + i\, G''(m). \tag{90}$$

We need not explicitly list $G'(m)$ and $G''(m)$, since they are very easily obtained from Eq. (73). The results for S are

$$S_{B\ell} = -\frac{M}{2\pi^2}\int_{-\pi/2+\delta}^{\pi/2+\delta} d\theta \int_0^\infty dm\; e^{-m\omega}\, m\, \Sigma_n\{\quad\}_n,$$

where

$$\{\quad\}_n = \frac{A_n e^{-k_n(H+\Delta)}}{(m_\theta{}^2 + k_n{}^2)}\left[-k_n + K_0 \sec^2\theta\, G'(m_\theta)\right]; \tag{91}$$

$$S_{C\ell} = \frac{M}{2\pi^2}\int_{-\pi/2+\delta}^{\pi/2+\delta} d\theta \int_0^\infty dm\; e^{-m\omega}\, m \frac{\partial}{\partial z}\{\mathrm{Re}\, C(\quad) - \Sigma_j\, \mathrm{Re}\, C_j(\quad) + \mathrm{Re}\, D(\quad) - \Sigma_j\, \mathrm{Re}\, D_j(\quad)\}; \tag{92}$$

$$S_{Bs} = \frac{M}{\pi^2}\int_{-\pi/2+\delta}^{\pi/2} d\theta\, K_0 \sec^2\theta \int_0^{\sqrt{V_\theta{}^r}} dK \sin(K\omega)\, K\, G''\left(\sqrt{V_\theta{}^r - K^2}\right) \Sigma_n \frac{A_n e^{-k_n(H+\Delta)}}{K_\theta{}^2 - k_n{}^2}; \tag{93}$$

and

$$S_{Cs} = \frac{M}{\pi^2} \int_{-\pi/2+\delta}^{\pi/2} d\theta \int_0^{\sqrt{V_\theta r}} dK \sin(K\omega)\, K \frac{\partial}{\partial z} \{C'[\ ] - C''[\ ] - \Sigma_j C_j[\ ] + D[\ ] - \Sigma_j D_j[\ ]\}. \tag{94}$$

As in Eq. (92), the z partial differentiation is performed (very easily), and then the result is evaluated for $z = 0$. The residue terms are

$$S_{Br} = \frac{M}{\pi} \int_{-\pi/2+\delta}^{\pi/2} d\theta\, \Sigma_n A_n e^{-k_n(H+\Delta)} \left\{ \begin{array}{l} \frac{1}{2} \sin(\sqrt{k_n^2 + V_\theta r}\,\omega)\,[-k_n + K_0 \sec^2\theta\, G(ik_n)] \\ \quad + K_0 \sec^2\theta \sin(K_0 \sec^2\theta\,\omega) \end{array} \right\} \tag{95}$$

and

$$S_{Cr} = \frac{M}{\pi} \int_{-\pi/2+\delta}^{\pi/2} d\theta\, K_0 \sec^2\theta \sin(K_0 \sec^2\theta\,\omega) \frac{\partial}{\partial z} \{C[\ ] - \Sigma_j C_j[\ ] - D[\ ] + \Sigma_j D_j[\ ]\}. \tag{96}$$

Again, the coefficients are easily obtained from the counterpart expressions for w, and so do not need to be explicitly listed.

Effect of the Rigid-Lid Condition

As mentioned in the Introduction, the rigid-lid boundary condition is the basis of most internal wave calculations. It is that the surface displacement ζ and hence the velocity component w vanish at $z = 0$. One operating definition of internal wave effects, in fact, is that these are the effects in a free-surface boundary condition calculation which survive the imposition of a rigid-lid boundary condition. From Eq. (27), for example, it is seen that internal wave effects can be extracted by simply taking the limit

$$K_0 \to \infty \qquad \text{(rigid-lid boundary condition)} \tag{97}$$

in the previous expressions. Of course, surface displacement and $W|z = 0$ vanish in this limit, but strain rate S does not. The limit in Eq. (97) also has the effect of moving the pole at $K = K_0 \sec^2\theta$ on the real axis out to infinity, so that this pole gives no contribution—hence, no Kelvin wake [2]. These conditions and the limiting homogeneous fluid case[2] are useful checks on the above expressions.

NUMERICAL CALCULATIONS FOR LOCALIZED SURFACE DISTURBANCE INDUCED BY A RANKINE OVOID

In this section numerical computations are performed for an isolated contribution from a hull, viz, the localized surface displacement ζ_l and rate of strain S_l induced by the hull when it is below the thermocline. We shall see that the hull can be simulated by a point source and point sink of specified strength, separated by a specified distance. Then we have a superposition

of contributions from each of these two (source and sink), which are given by Eqs. (83), (84), (91), and (92) in our calculations later on in this section.

Simulation of the Ovoid

We describe the hull simply as a Rankine ovoid which is simulated by a point sink and point source. This is essentially identical to Yim's procedure [2] for the hull. It is explained in fluid mechanics texts [15], and we shall just give the bottom line here.

Shown in Fig. 5 is a slice through the center of the ovoid in the xz plane. The ovoid (hull) is a body of revolution about the x axis traveling in the negative x direction with speed U. Its length is 2ℓ and its width is $2h$ in Fig. 5. The distance from its center to the point source (toward front of ovoid) or sink (toward rear of ovoid) is a. The strength of the point source is M, as defined in Eq. (9), and the point sink can be regarded as a point source of strength $-M$. The values of

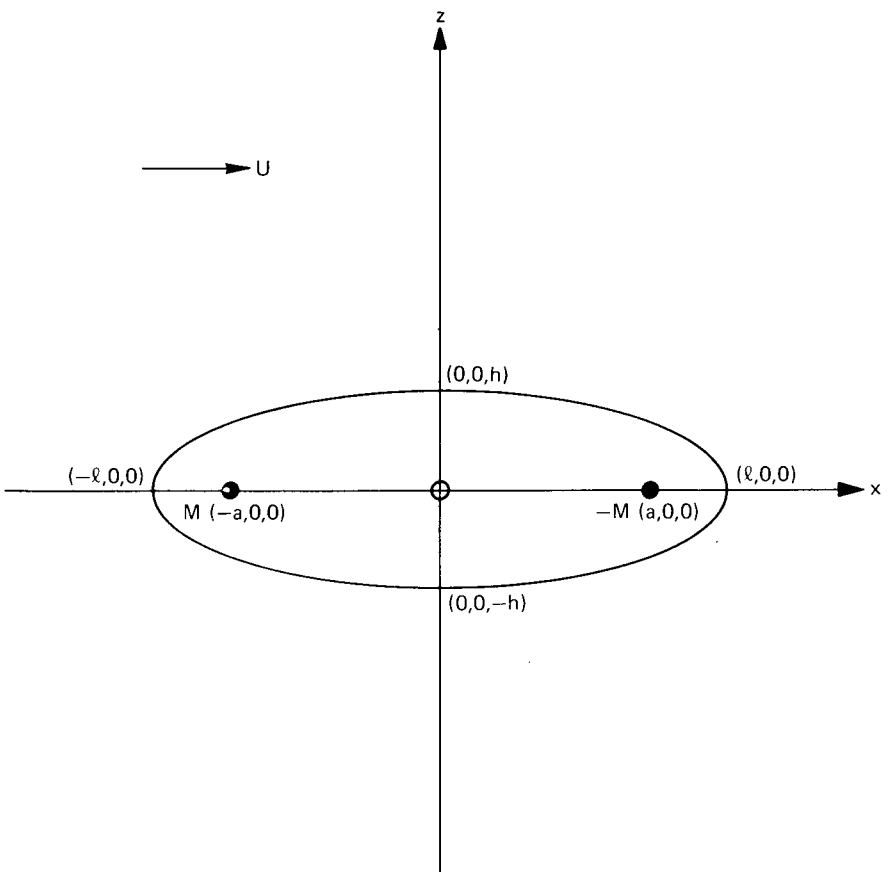

Fig. 5 – Coordinate diagram for hull simulation in an incompressible fluid moving with velocity U

M and a are adjusted to the half-length ℓ and half-width h parameters of the hull through the equations

$$M = (\pi h^2 U/a)\sqrt{h^2 + a^2} \tag{98}$$

where a is found as a solution of

$$f(x) = x^2 - 2\ell^2 x + \ell^4 - h^2 \ell \sqrt{h^2 + x} = 0, \tag{99}$$

where

$$x \equiv a^2.$$

A numerical solution of Eq. (99) consists of stepping x from 0 to ℓ^2 in preset increments and finding where $f(x)$ changes sign. At this point the solution x is zeroed in on through use of the Newton-Raphson method. The solution a is then used in Eq. (98) to find M. In Table 1 are given solutions for a for several h and ℓ ovoid parameters. Our calculations below will be for a particular choice of ovoid parameters. Our canonical Rankine ovoid will have a length of 100 m ($1 =$ 50 m) and a width of 10 m ($h/\ell = 0.1$). For these parameters we compute $a = 47.49$ m and $M =$ 78.97 m$^2 \times U$. The ovoid dimensions we use are very close to those used by Yim. Our computations for these parameters have utilized homogeneous fluid techniques, but the corrections for density stratification are minor and unimportant in this case. Certainly much more serious approximations are inherent in the model B-V profile used below.

Table 1 – Solutions for the Source-Sink Separation Parameter a for Various Rankine Ovoid h/ℓ Ratios

h/ℓ†	Length in Meters				
	25	37.5	50	62.5	75
0.05	24.37	36.56	48.75	60.94	73.12
0.10	23.75	35.62	47.49	59.37	71.24
0.15	23.11	34.67	46.23	57.79	69.34
0.20	22.47	33.71	44.95	56.18	67.42
0.25	21.82	32.73	43.64	54.55	65.46
0.30	21.15	31.73	42.30	52.88	63.45
0.35	20.46	30.69	40.92	51.15	61.38
0.40	19.74	29.61	39.49	49.36	59.23

†Length ℓ is in meters and h is contained in the ratio h/ℓ. See Eq. (99) in text.

Use of Symmetries

With regard to coordinate axes shown in Fig. 1, it is perfectly clear that there must be symmetry under a reflection on the surface through the x axis, i.e.,

$$\zeta(x, -y) = \zeta(x, y) \quad \text{and} \quad S(x, -y) = S(x, y).$$

With respect to coordinates defined in Eq. (38),

$$\zeta(R, 2\pi - \delta) = \zeta(R, \delta) \qquad \text{and} \qquad S(R, 2\pi - \delta) = S(R, \delta), \tag{100}$$

so that we can restrict our attention to $0 \leq \delta \leq \pi$. We shall specify now that $\zeta(R, \delta)$ and $S(R, \delta)$ represent contributions from a single point source, but the statement in Eq. (100) applies to any axisymmetric distribution of point sources and sinks. From Eqs. (83), (84), (91), and (92) we see that $\zeta_\ell(R, \delta)$ and $S_\ell(R, \delta)$ can be written in the forms

$$\zeta_\ell(R, \delta) = \int_{-\pi/2+\delta}^{\pi/2+\delta} d\theta\, f(\cos(\theta - \delta))\, g_e(\cos\theta)\, \sec\theta$$

$$S_\ell(R, \delta) = \int_{-\pi/2+\delta}^{\pi/2+\delta} d\theta\, f(\cos(\theta - \delta))\, g_e'(\cos\theta) \tag{101}$$

where g_e and g_e' are even functions of $\cos\theta$.

Hence, for example, $\zeta_\ell(R, \delta)$ can be manipulated as follows:

$$\zeta_\ell(R, \delta) \underset{\theta \to \theta+\delta}{=\!=} \int_{-\pi/2}^{\pi/2} d\theta\, f(\cos\theta)\, g_e \cos(\theta + \delta) \sec(\theta + \delta)$$

$$\underset{\theta \to -\theta}{=\!=} \int_{-\pi/2}^{\pi/2} d\theta\, f(\cos\theta)\, g_e \cos(\theta - \delta) \sec(\theta - \delta) \qquad \text{[cf. Eq. (100)]}$$

Also,

$$\zeta_\ell(R, \pi - \delta) = \int_{-\pi/2}^{\pi/2} d\theta\, f(\cos\theta)\, g_e \cos(\theta + \delta - \pi) \sec(\theta + \delta - \pi)$$

$$= -\int_{-\pi/2}^{\pi/2} d\theta\, f(\cos\theta)\, g_e \cos(\theta + \delta) \sec(\theta + \delta).$$

By such manipulations, we find that

$$\zeta_\ell(R, \pi - \delta) = -\zeta_\ell(R, \delta) \qquad \text{and} \qquad S_\ell(R, \pi - \delta) = S_\ell(R, \delta), \tag{102}$$

which means that we can restrict our attention to $0 \leq \delta \leq \pi/2$ in calculations of the localized surface disturbance due to a point source. The symmetry relation of Eq. (102) does not apply to stratification and residue contributions. In Eq. (101), it is seen that for the special case $\delta = 0$ the θ integration actually needs to be carried out only between $\theta = 0$ and $\theta = \pi/2$.

We can also develop symmetry relations, based on Eq. (102), for the total localized surface disturbance from the hull, which is simulated by a point source and a point sink. The appropriate coordinate system is shown in Fig. 6. If we denote, for example, $\zeta_\ell^{(h)}(R, \delta)$ as the total surface displacement due to the hull with respect to the origin of coordinates indicated in Fig. 6, and if we denote $\zeta_\ell(R_1, \delta)$ as the contribution of the point source of strength M, then

$$\zeta_\ell^{(h)}(R, \delta) \equiv \zeta_\ell^{(h)}(P) = \zeta_\ell(R_1, \delta_1) - \zeta_\ell(R_2, \delta_2). \tag{103}$$

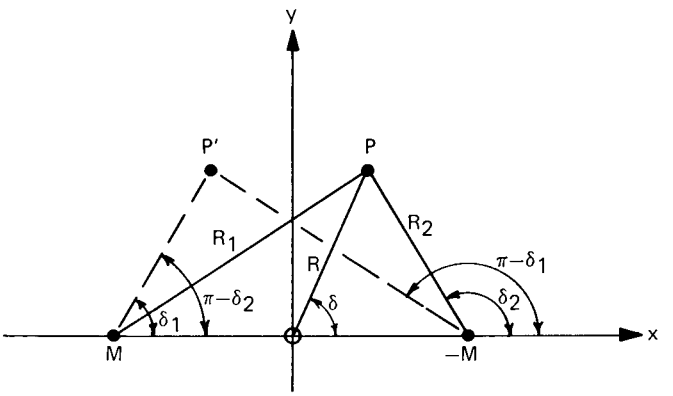

Fig. 6 – Coordinate system for calculation of surface disturbance due to the hull. P is the field point under consideration, and P' is a conjugate point at the reflection of P through the y axis. The source and sink surface projection points are shown on the x axis symmetrically placed about the origin of coordinates.

With respect to Fig. 6, we have from Eq. (102)

$$\zeta_t^{(h)}(R, \pi-\delta) \equiv \zeta_t^{(h)}(P') = \zeta_t(R_2, \pi-\delta_2) - \zeta_t(R_1, \pi-\delta_1) = -\zeta_t(R_2, \delta_2) + \zeta_t(R_1, \delta_1) = \zeta_t^{(h)}(P).$$

With these manipulations we have deduced a symmetry relation for $\zeta_t^{(h)}(R, \delta)$. Exactly analogously, a symmetry relation for $S_t^{(h)}(R, \delta)$, the total localized rate of strain due to the hull, can be deduced. The results are

$$\zeta_t^{(h)}(R, \pi-\delta) = \zeta_t^{(h)}(R, \delta), \qquad S_t^{(h)}(R, \pi-\delta) = -S_t^{(h)}(R, \delta). \tag{104}$$

Equation (100) also applies here, so that we may restrict our attention to $0 \leq \delta \leq \pi/2$ in the calculations of localized surface disturbance due to the hull.

Numerical Procedure

A computer program was written to evaluate $\zeta_t^{(h)}(R, \delta)$ and $S_t^{(h)}(R, \delta)$ over the surface, using the notation of the preceding section. The procedure was to calculate the localized disturbance in Eqs. (81) and (96) over a surface mesh for a single point source, and then to combine point-source and point-sink contributions according to the geometry of Fig. 6 in a parabolic interpolation scheme (see, e.g., Eq. (103)). The program is very complicated, including a variety of interpolation and iterative schemes to take care of various practical difficulties which arise. At its heart, however, the approach can be described quite simply. The basic form of the point source expressions is as follows:

$$\begin{aligned} \zeta_t &= \frac{M}{2\pi^2 U} \int_{-\pi/2}^{\pi/2} d\theta \, \sec(\theta+\delta) \int_0^\infty dm \, e^{-mR\cos\theta} \, \mathscr{F}(M_{\theta+\delta}, \sec^2(\theta+\delta)) \\ S_t &= \frac{M}{2\pi^2} \int_{-\pi/2}^{\pi/2} d\theta \, K_0 \sec^2(\theta+\delta) \int_0^\infty dm \, e^{-mR\cos\theta} \, m \, \mathscr{G}(m_{\theta+\delta}, \sec^2(\theta+\delta)), \end{aligned} \tag{105}$$

where m_θ is given by Eq. (75). The technique used is to evaluate the m integration by special integration formulae, developed from a technique which we shall refer to as Filon's method [17]. This gives an integrand value for a given θ mesh point. The θ integration is handled by Simpson's rule. The discussion of Filon's method, along with a description of the formulae needed in the evaluation of Eq. (105), is given in Appendix D.

In Filon's method one separates the integrand into two factors, so that the integral has the form

$$G(a, b) = \int_a^b F(x) f(x)\, dx. \tag{106}$$

The factor $F(x)$ is chosen to be analytically integrable; i.e., the integral in Eq. (106) could be evaluated in closed form if $f(x)$ were replaced by unity. As Appendix D shows, the power of this technique is that the numerical evaluation of G now requires a choice of mesh with subinterval width h only small enough that $f(x)$ can be adequately approximated by a Taylor expansion to second order about the center of an adjacent pair of subintervals. Put more concisely, we need h small enough so that f can be fitted by a parabola in an adjacent pair of subintervals. This can be an immense practical simplification over a brute-force application of Simpson's rule (which is a special case of Filon's method for $F(x) = 1$) if $F(x)$ is rapidly varying compared to $f(x)$. In this case the time-consuming evaluation of the integrand need be carried out at far fewer mesh points (larger h) than in Simpson's rule, which would require a more finer grid of points. For example, in Eq. (105), the exponential factor is rapidly varying in the far field, so that the choice

$$F^{(1)}(m) = e^{-mR\cos\theta}, \tag{107}$$

associated with Eq. (106), is made for at least a portion of the m integration. A further simplification occurs when $m >> \sqrt{V_\theta r}$, $\sqrt{V_\theta}$. In this case, continuum contributions dominate, and they are given by (see Eq. (105))

$$\mathscr{F}(m, \sec^2\theta) \approx m\frac{m\cos md - (K_0\sec^2\theta)\sin md}{m^2 + K_0^2\sec^4\theta} \approx \mathscr{G}(m, \sec^2\theta). \tag{108}$$

Actually, the asymptotic approximation used in the computer program also includes an associated approximation for bound states and for the one normalization root term which occurs when $V_\theta < 1$. The point we make here is that when the asymptotic approximation is sufficiently accurate (e.g., within 3%), we use it and resort to a further application of Filon's method for continuum states based on Eq. (108). We use both

$$F^{(2)}(m) \equiv e^{-mR\cos\theta}\cos md$$

and

$$F^{(3)}(m) \equiv e^{-mR\cos\theta}\sin md. \tag{109}$$

Actually, there are situations when $\sqrt{V_\theta r}$ is comparable to m even though $m >> \sqrt{V_\theta}$, and we must heed the prescription of Eq. (105) which dictates that we replace m in Eq. (108) by m_θ. Filon's method has been extended to encompass this case too, as described in Appendix D.

It is quite clear from Eqs. (105) and (108) that the m integration is very slowly convergent, especially when R is not too large, or θ is sufficiently close to the upper or lower limits of its integration. In fact, when the exponent in Eq. (105) vanishes, our basic contour integration techniques are apparently not valid, since the convergence in the exponential was assumed. We developed a linear interpolation or extrapolation scheme to handle these points, but this is of no major importance in the present discussion. The point is that the slow convergence in the m integration is what motivated us to make full use of Filon's method—e.g., with the help of asymptotic approximations. The m integral in Eq. (105) was computed in groups of six subintervals at a time. In each of these groups the subinterval width h was computed. When we were not in the asymptotic region, h was computed iteratively in a doubling scheme so that the changes of the most rapidly varying phases in the trigonometric functions in $f(x)$ over a subinterval h in the group did not exceed a certain value (e.g., 0.5). The maximum such h for each successive group was determined this way and used. When it was determined that the asymptotic approximation was valid, $F^{(2)}$ and $F^{(3)}$ in Eq. (109) were also used and the residual f functions were simple enough that h was calculated analytically as the minimum value of

$$h = 0.5 \left| f/(df/dm) \right|$$

in the subgroup distilled from the various residual f functions of Eq. (106) associated with $F^{(1)}$, $F^{(2)}$, and $F^{(3)}$. In this way the m integration was performed relatively quickly.

The θ integration was performed by dividing up the range $[0, \pi]$ into 100 subintervals and applying Simpson's rule. Some experimentation with the variable change from θ to u, where

$$u = \tan \theta, \tag{110}$$

was carried out, which lessens the impact of the singularities at $\theta = \pm \pi/2$ in Eq. (105), but the results are inconclusive at this writing. It appears that this transformation [2] is also advantageous for evaluation of the residue and stratification contributions, but this is a subject for future investigations. We shall discuss the results of the numerical procedure in the next part.

Results for Rankine Ovoid Model

The numerical computation of $\zeta_\ell^{(h)}(R, \delta)$ and $S_\ell^{(h)}(R, \delta)$ is carried out in this part, utilizing the coordinate system shown in Fig. 6. The calculations are performed for a variety of density-stratification models contained within the square-well description, which is embodied by Eqs. (43)–(45). The B-V profile designations and parameters used are given in Table 2. The thermocline profiles T1-T7 are obtained by fitting (graphically) various averaged, smoothed, seasonal B-V profiles [16] in waters near the United States with our square-well model. An example of this procedure is shown in Fig. 7 for winter and summer B-V profiles in Canadian Square Plate 1214 off the west coast. These correspond to the profiles T1 and T2 in Table 2, respectively. Beside T1, C2 can, for example, be taken as representative of winter conditions in some ocean areas. The variety of profiles T2-T6 can be taken as representative of summer conditions in the world oceans.

We first intended to show the pattern, never previously calculated, of localized surface disturbance over a range of R and δ values in Fig. 6 ($0 \leq \delta \leq \pi/2$). This necessitates a rather

Table 2 – B-V Profile Parameters Used in the Square-well Model Calculations of Localized Surface Distrubance

B-V Profile Designator	H (m)	A (m)	$N_0^2 \times 10^6$ (sec^{-2})	$N^2 - N_0^2 \times 10^6$ (sec^{-2})
H†	10	10	0	1
C1	10	10	15	1
C2	10	10	80	1
C3	10	10	150	1
C4	10	10	250	1
C5	10	10	350	1
C6	10	10	450	1
C7	10	10	550	1
T1	45	40	64	44
T2	15	42.5	84	72
T3	5	22.5	100	205
T4	10	20	95	260
T5	10	35	80	280
T6	0	25	70	460

†The mnemonic significance of the designators is H (homogeneous fluid), C (constant-stratification fluids), and T (fluids with thermoclines).

complete pattern for a single point source, followed by interpolation of these results in accordance with Fig. 6. Furthermore, with all the possible combinations of speed, depth, and profile designator, it became clear that this would be a very costly project. We did carry it out, however, for one depth (130 m) and speed (20 knots) for the H profile, and the results for a few of the δ values are shown in Figs. 8 and 9. The results indicate a surface depression centered over the center of the hull (i.e., the Bernoulli Depression) and extending out almost one hull length in radius, as far as $\zeta_t^{(h)}(R, \delta)$ is concerned. The rate-of-strain calculation in Fig. 9 indicates a blob of surface contraction centered over the point sink in Figs. 5 and 6 and a blob of surface expansion centered over the point source. The results which led to Figs. 8 and 9 took the better part of an hour to compute on the CDC 3800, since a rather complete pattern of point-source disturbance is needed as a preliminary. Put another way, while δ is fixed, δ_1 and δ_2 are nevertheless varying as R changes in Fig. 6 and in the computations. Figures 8 and 9 indicate that the expense is not only intolerable but also unnecessary if we are interested in the order of magnitude of the maximum surface effect, which seems to occur near the wake line ($\delta = 0$). The main virtue of confining ourselves to the wake line is that we need only the $\delta = 0$ R-dependence for the point source in a combination interpolation scheme for the displaced point source and sink. The computing time saved is tremendous. It takes only a few minutes now to compute a wake line R-dependence for the hull. This has been computed previously for the surface displacement in a homogeneous fluid [2], but not for the rate of strain.

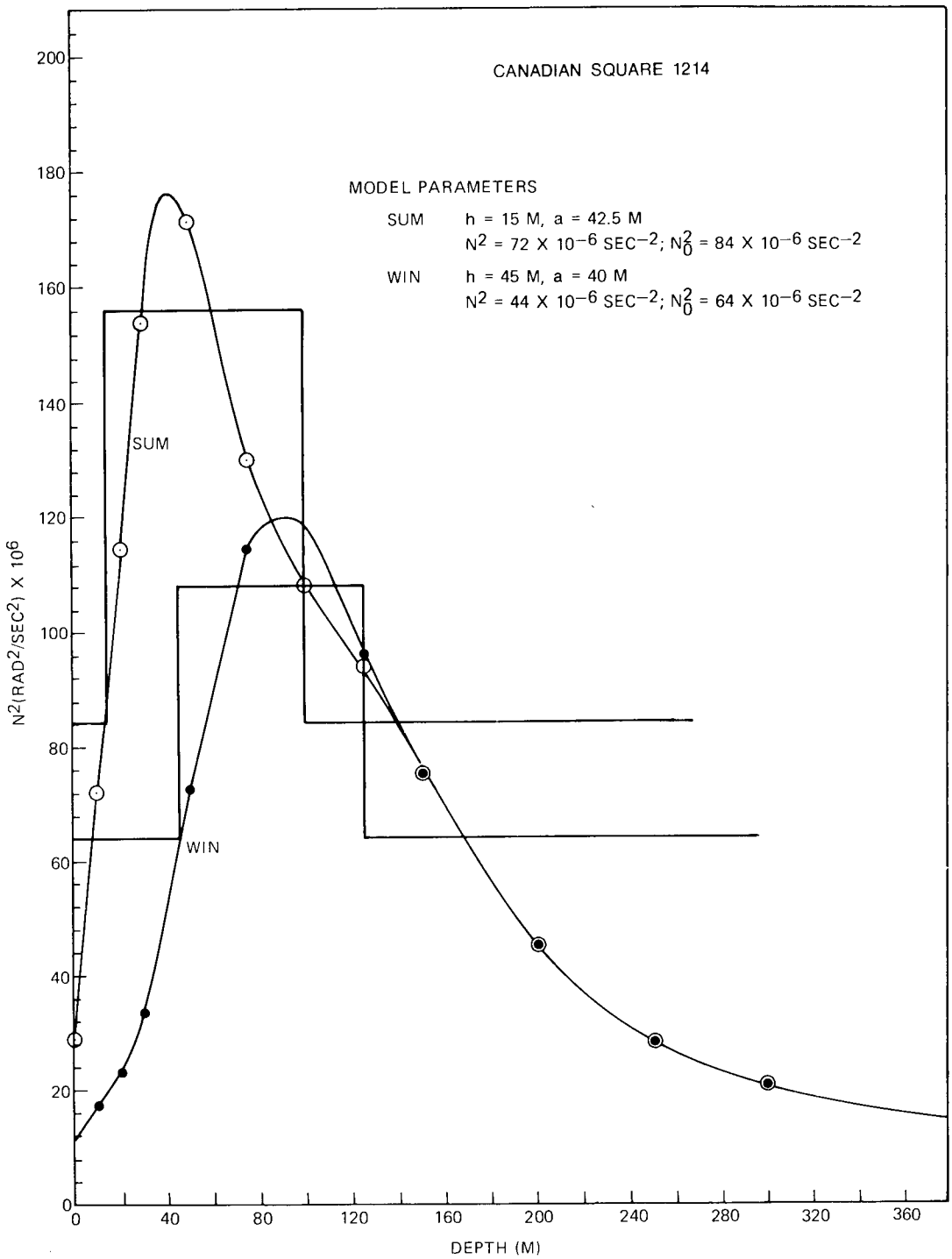

Fig. 7 — Illustrative square-well fits to two smoothed B-V profiles

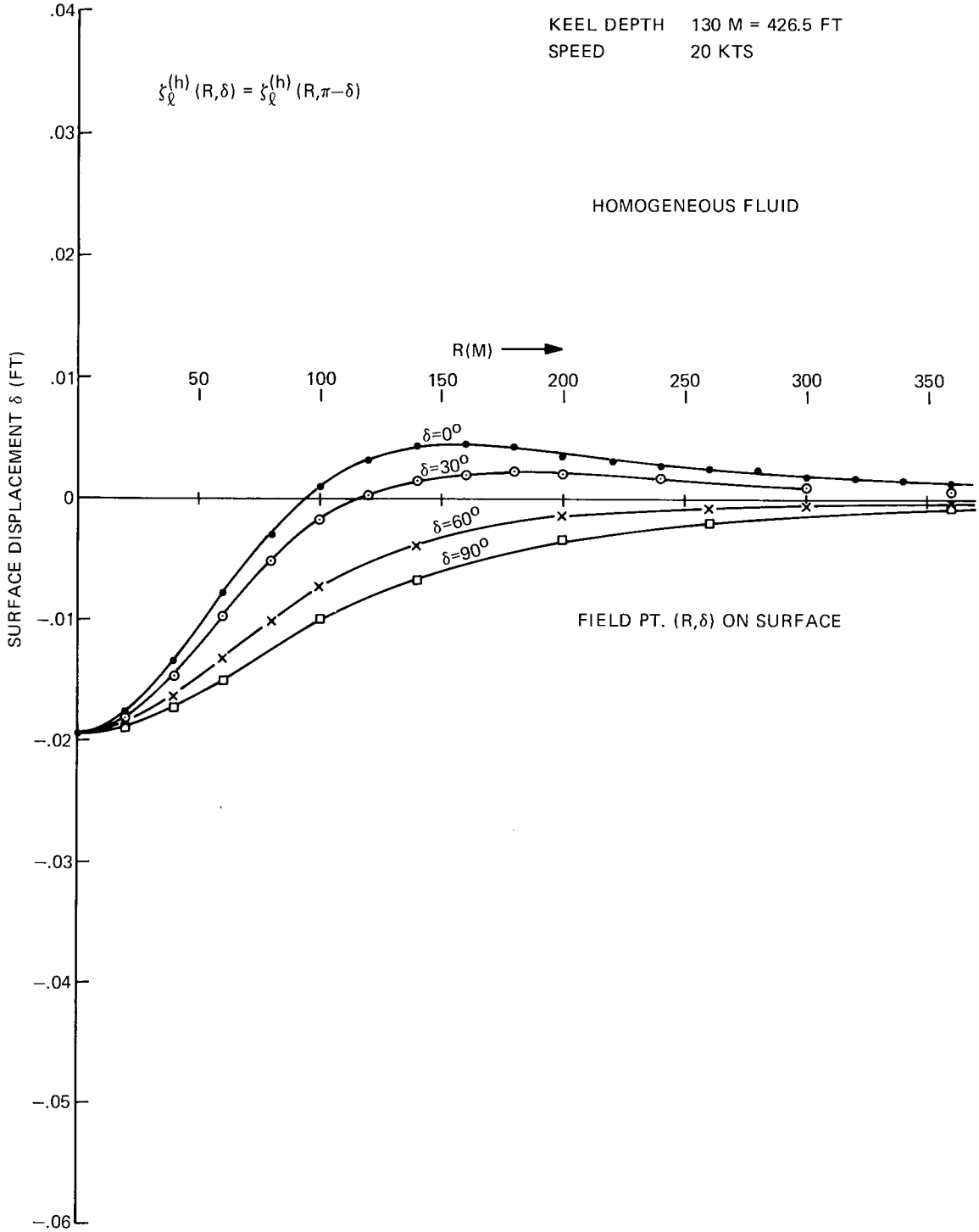

Fig. 8 — Surface displacement pattern from the hull. Center of the hull is at $R = 0$ and one end of it is at $R = 50$ m.

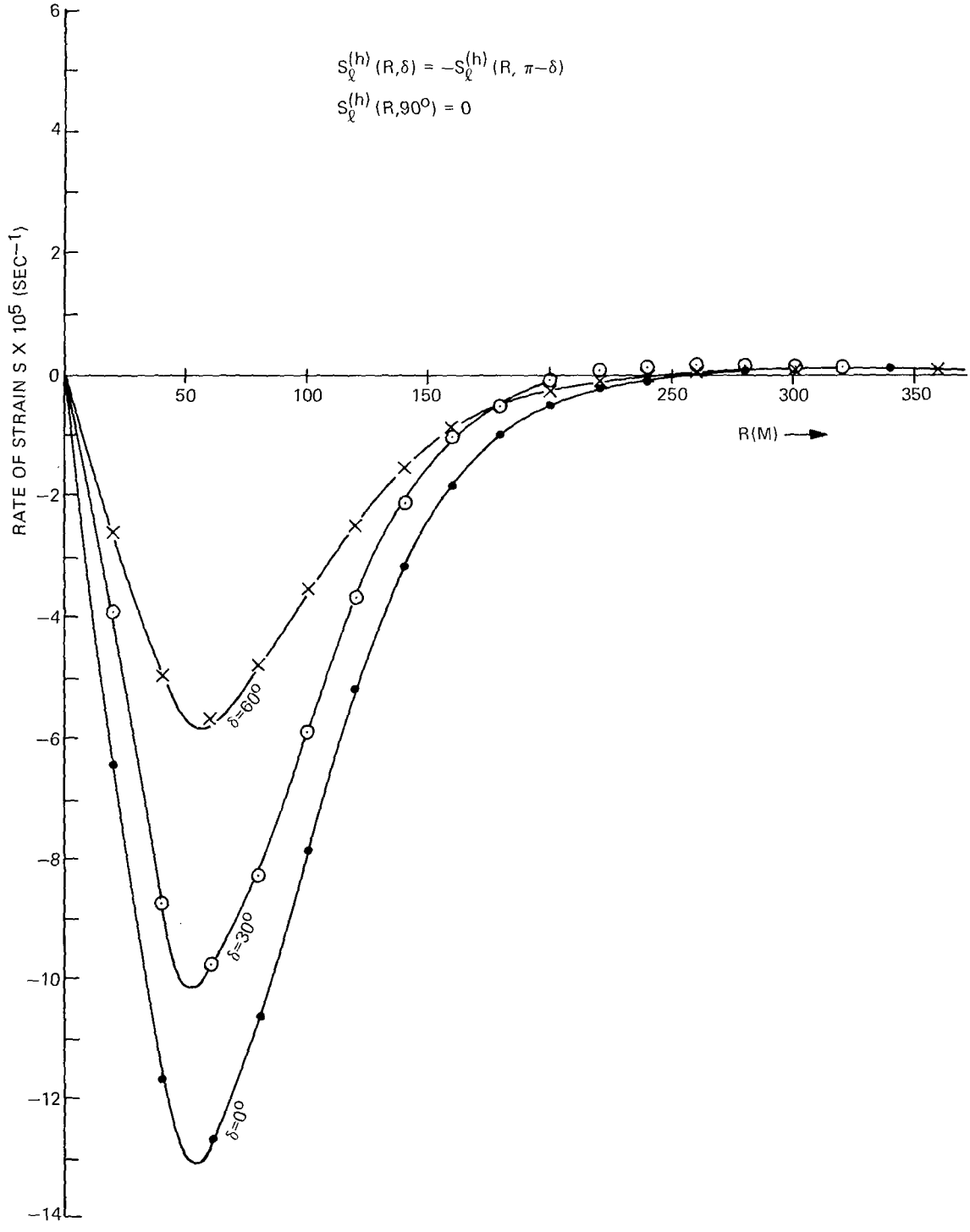

Fig. 9 — Surface rate-of-strain pattern for the parameters of Fig. 8

The wake-line R-dependence for the surface displacement, i.e., $\zeta_t^{(h)}(R, \delta = 0)$, is shown for various depths, speeds, and profiles in Figs. 10-21. Some profiles are missing for shallower depths, but this is merely because our computer program does not apply for a given profile when the point-source depth is no longer sufficient to place it beneath the thermocline. One thing of note in Figs. 10-17 is that the various C profiles, regardless of the amount of density stratification involved, yield surface displacements which do not differ appreciably from each other or from the H profile case. Another feature obvious in Figs. 10-21 is that the presence of a square-well thermocline in the T profiles can give a pronounced enhancement of surface displacement under certain circumstances, particularly in the vicinity of the point source and sink, where a pronounced surface displacement cusp apparently can occur. Some sort of resonance effect is suggested. A summary of maximum calculated surface displacements is contained in Table 3 to two significant figures.

Table 3 – Maximum Calculated Surface Displacements, Given $\zeta_t^{(h)}(R, \delta = 0) \times 10^3$ ft†

B-V Profile Designator	Speed of 10 knots					Speed of 20 knots				
	Depth (ft)				Misc. (Displ./Depth)	Depth (ft)				Misc. (Displ./Depth)
	500	400	300	200		500	400	300	200	
H	2.7	4.9	10	24		12	23	48	110	
C1	2.8	5.1	10	24		12	23	49	110	
C2	3.3	5.5	11	25		13	24	50	110	
C3	3.4	5.9	11	26		13	24	50	110	
C4	4.1	6.1	12	26		14	25	51	110	
C5	3.9	6.7	12	27		15	26	51	120	
C6	3.9	7.1	12	28		15	26	52	120	
C7	4.5	6.8	13	28		15	27	53	120	
T1	15	–	–	–	5.2/412	41	–	–	–	22/412
T2	4.3	5.7	–	–	26/330	15	210	–	–	77/330
T3	2.2	4.1	10	90	110/166	11	22	48	320	320/166
T4	1.9	4.1	9.8	260	51/166	11	22	47	990	200/166
T5	2.1	6.8	130	–	50/265	11	27	500	–	150/265
T6	2.1	3.3	8.7	52	130/166	10	20	46	180	880/166

†Two significant figures are used.

A perusal of Table 3 indicates that the thermocline in our model can have a pronounced effect on the H (and C) profile results. It can surpress the displacement somewhat in many cases, perhaps related to the fact that a fluid disturbance is partially reflected back down from the thermocline in its upward motion to the surface. In this picture the thermocline behaves like an index discontinuity in electromagnetism. On the other hand, in some cases substantial enhancement of surface displacement occurs – by as much as an order of magnitude under special circumstances which seem to be related to the parameters of the thermocline and the depth of the point source and sink.

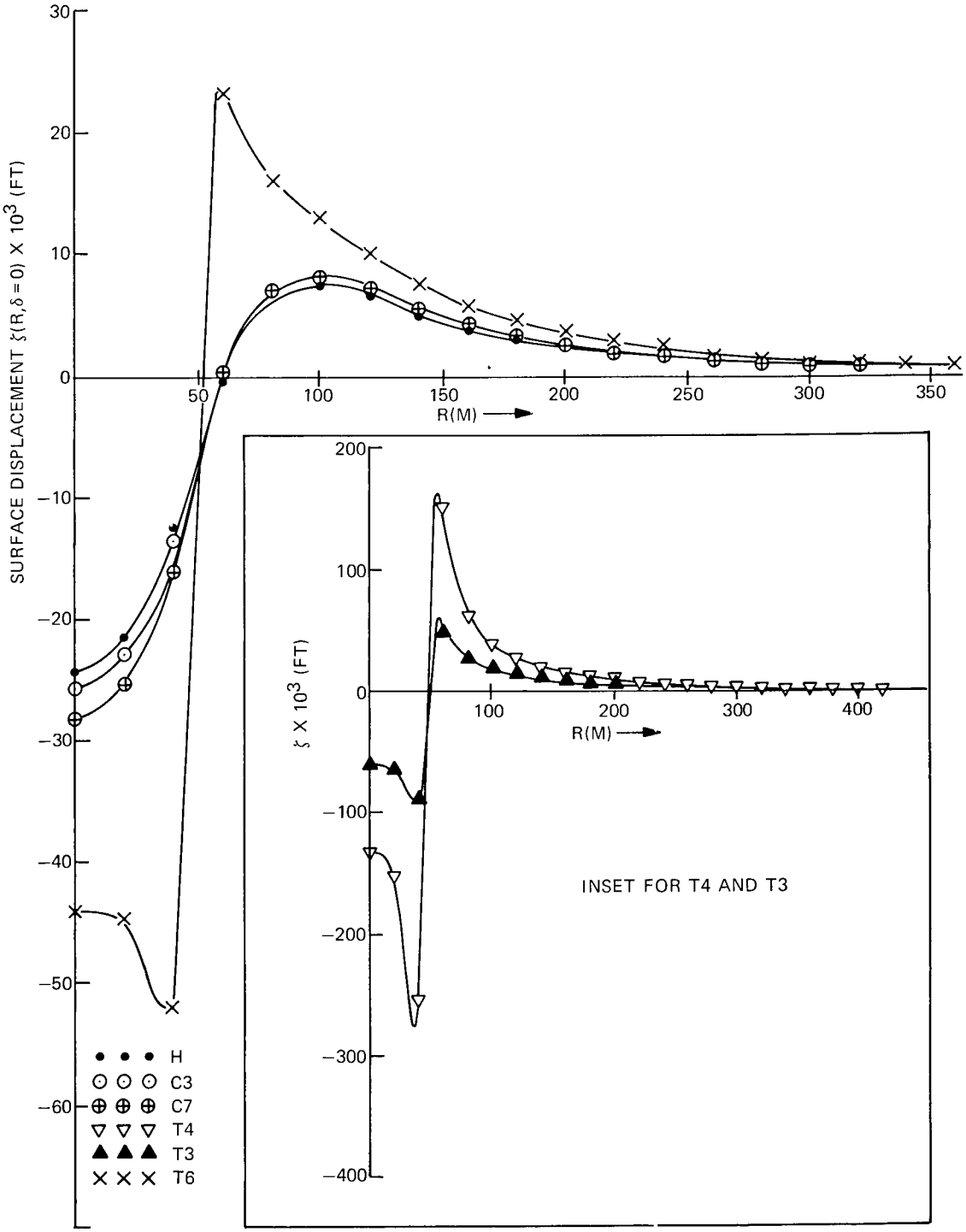

Fig. 10 — Wake-line surface displacement; depth 200 ft, speed 10 knots

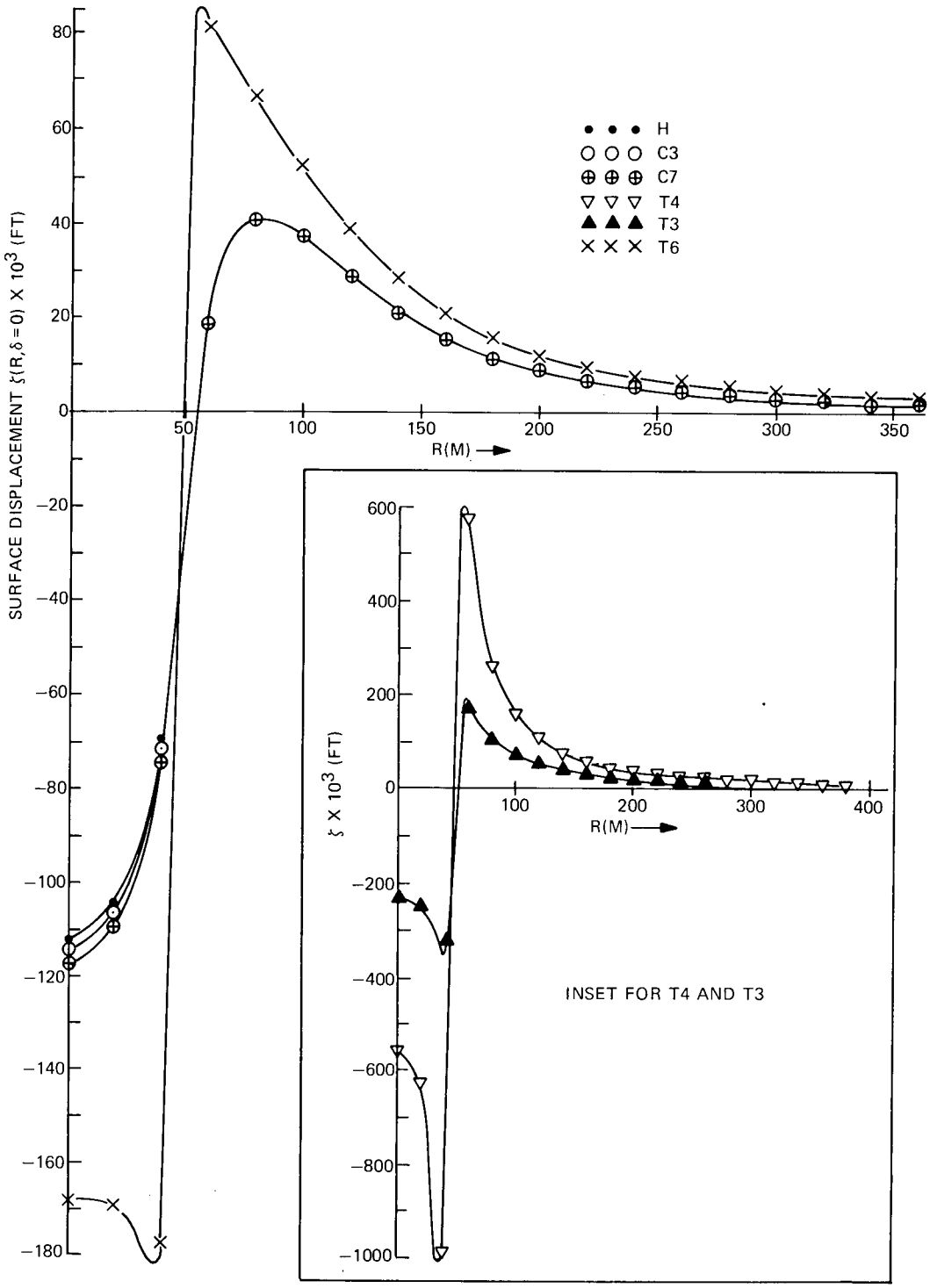

Fig. 11 — Wake-line surface displacement; depth 200 ft, speed 20 knots

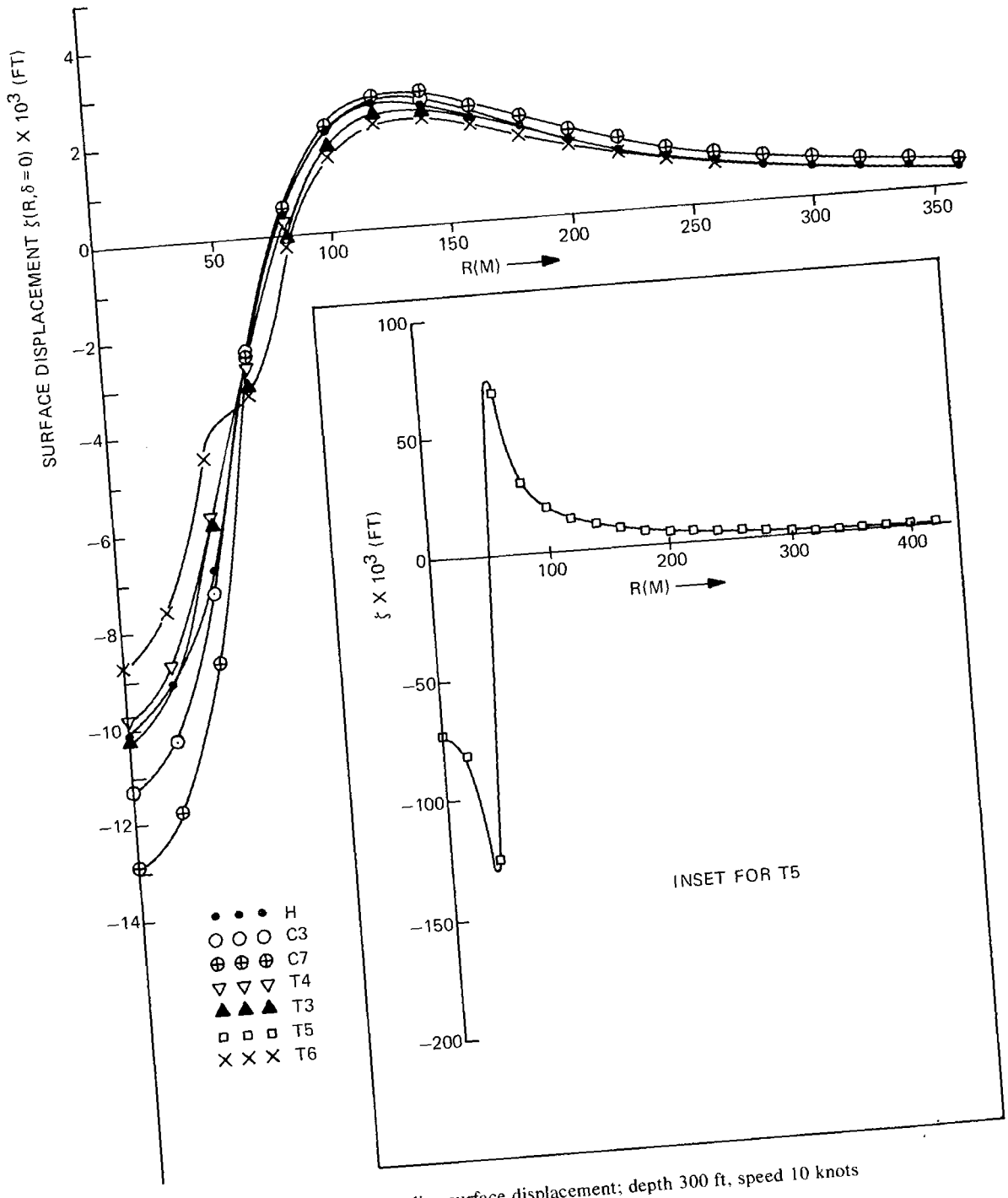

Fig. 12 — Wake-line surface displacement; depth 300 ft, speed 10 knots

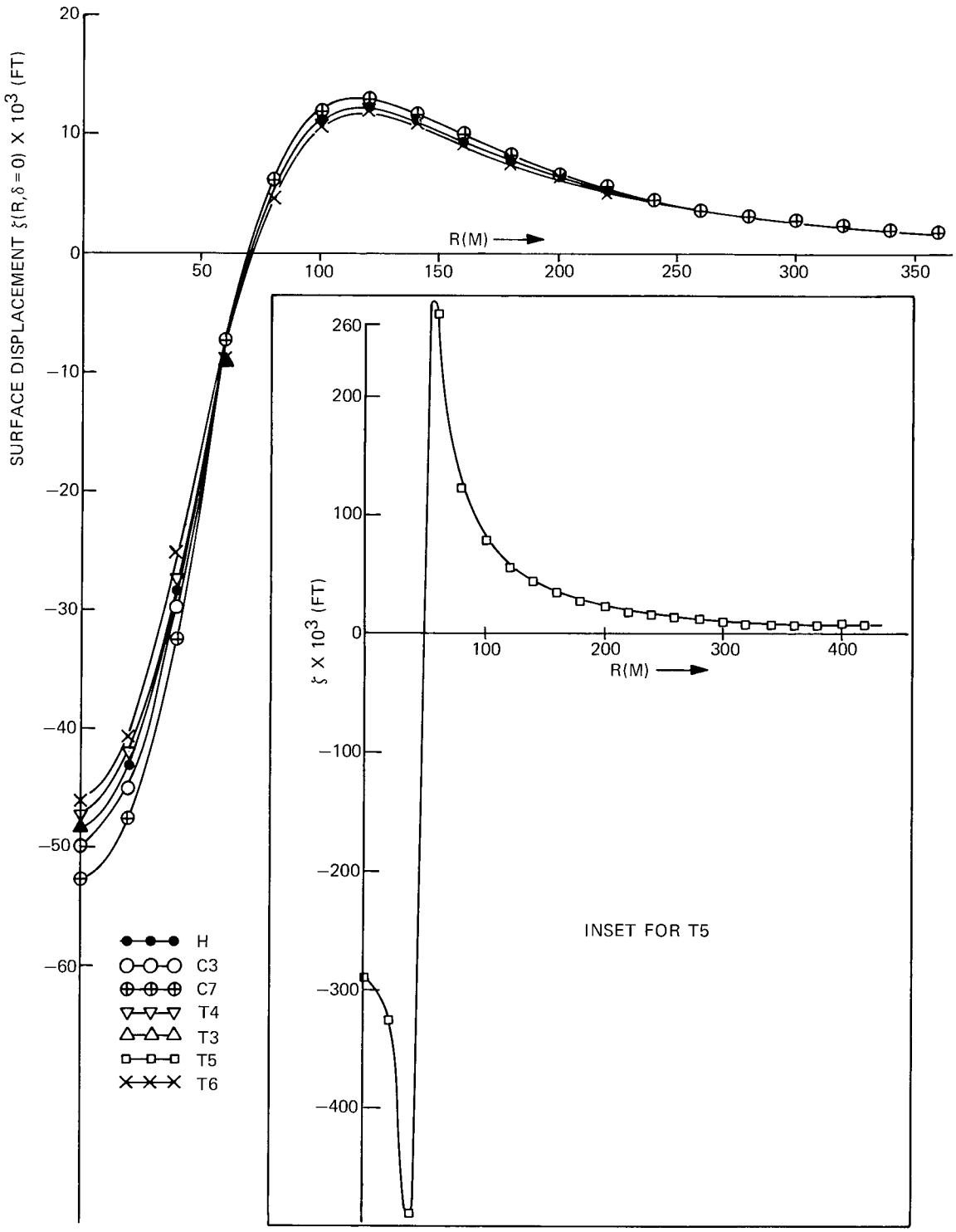

Fig. 13 — Wake-line surface displacement; depth 300 ft, speed 20 knots

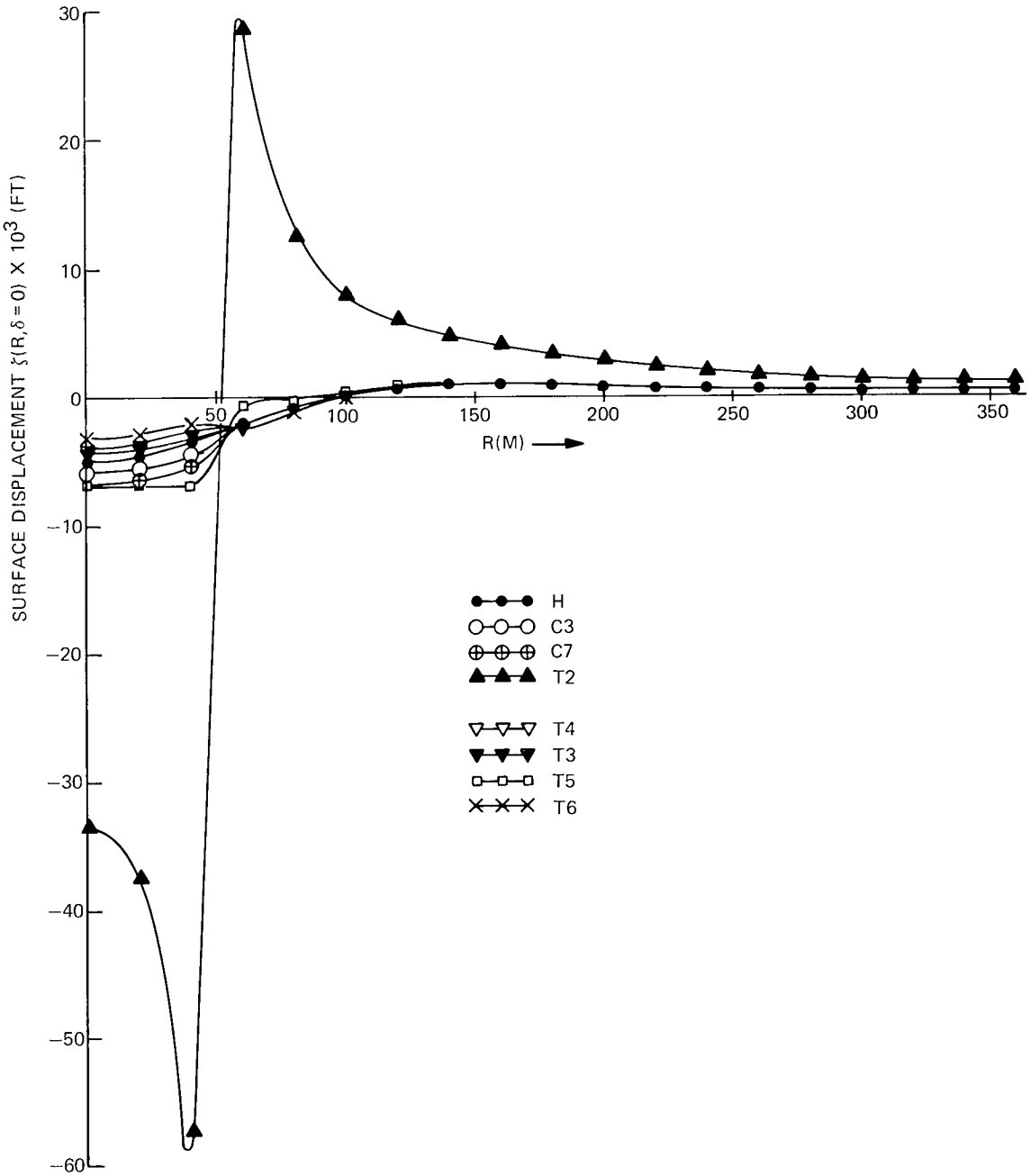

Fig. 14 — Wake-line surface displacement; depth 400 ft, speed 10 knots

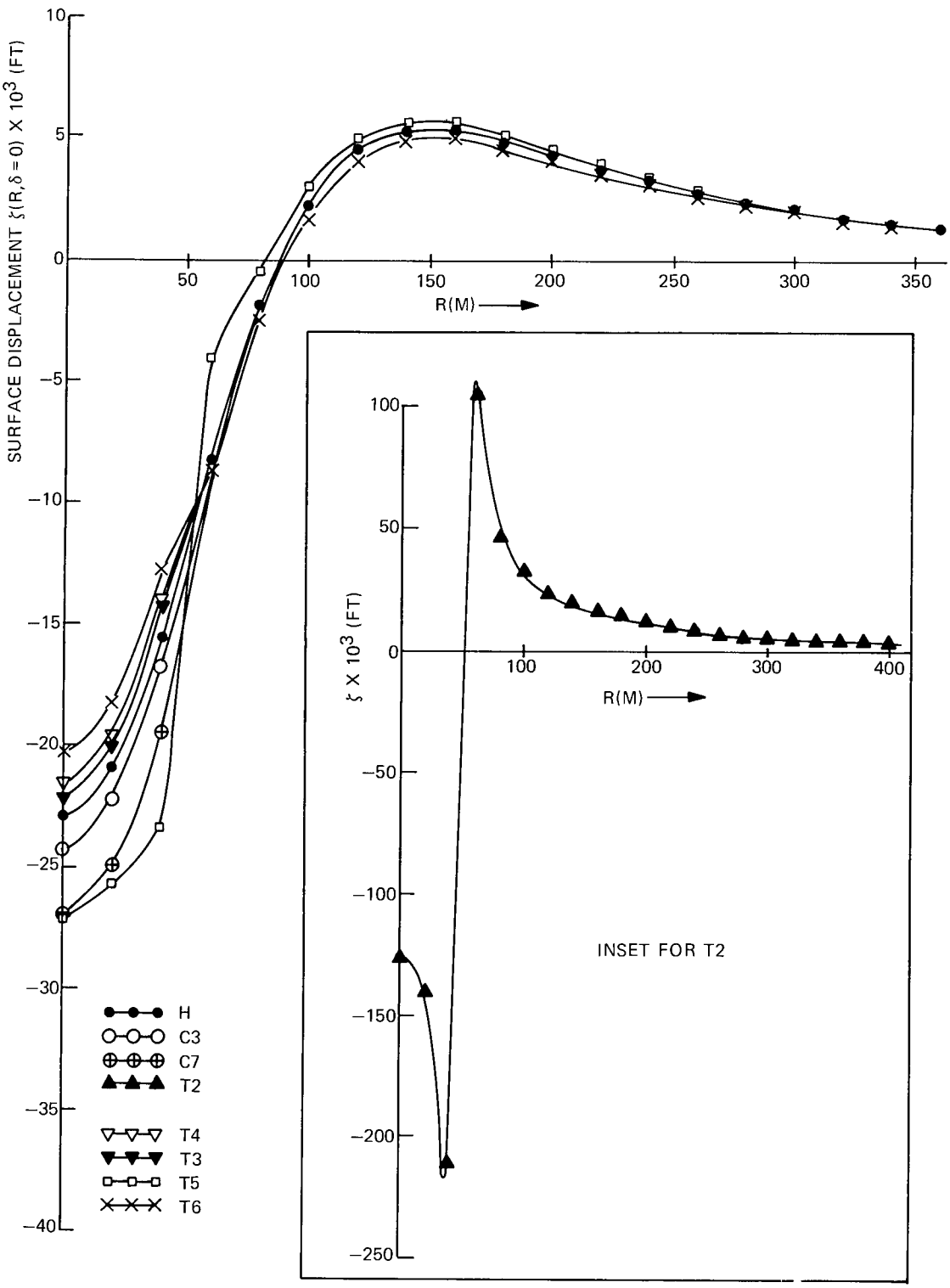

Fig. 15 — Wake-line surface displacement; depth 400 ft, speed 20 knots

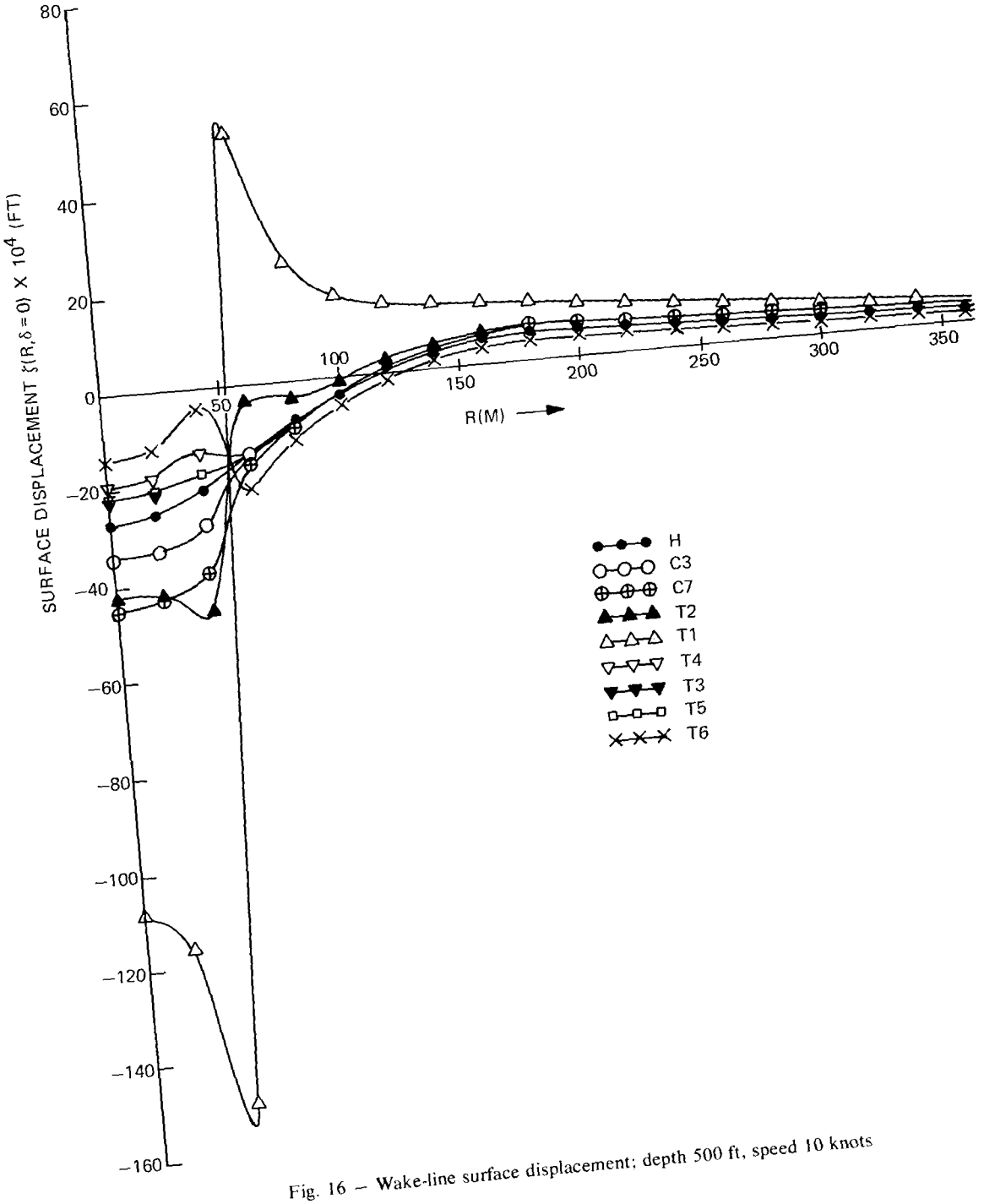

Fig. 16 — Wake-line surface displacement; depth 500 ft, speed 10 knots

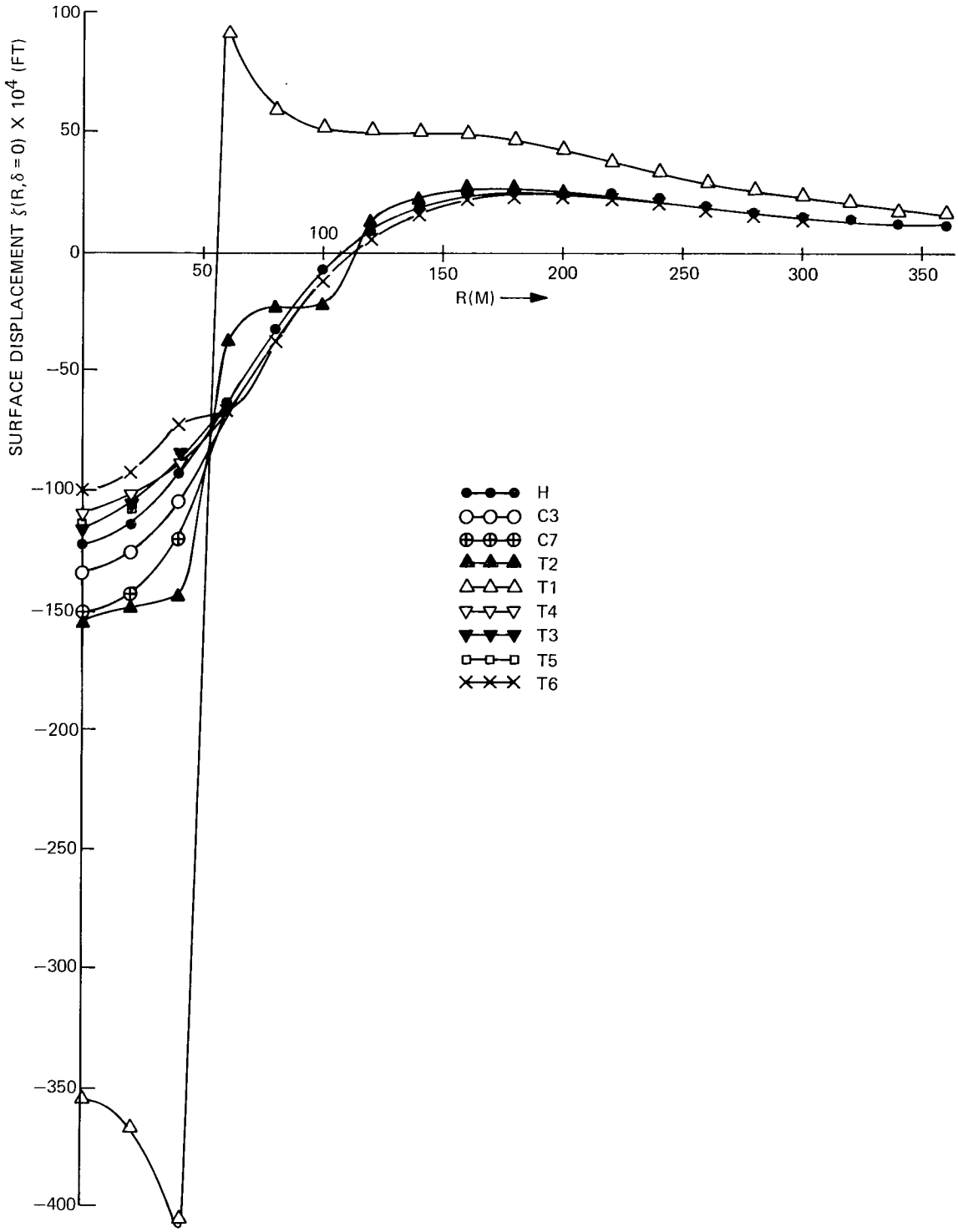

Fig. 17 – Wake-line surface displacement; depth 500 ft, speed 20 knots

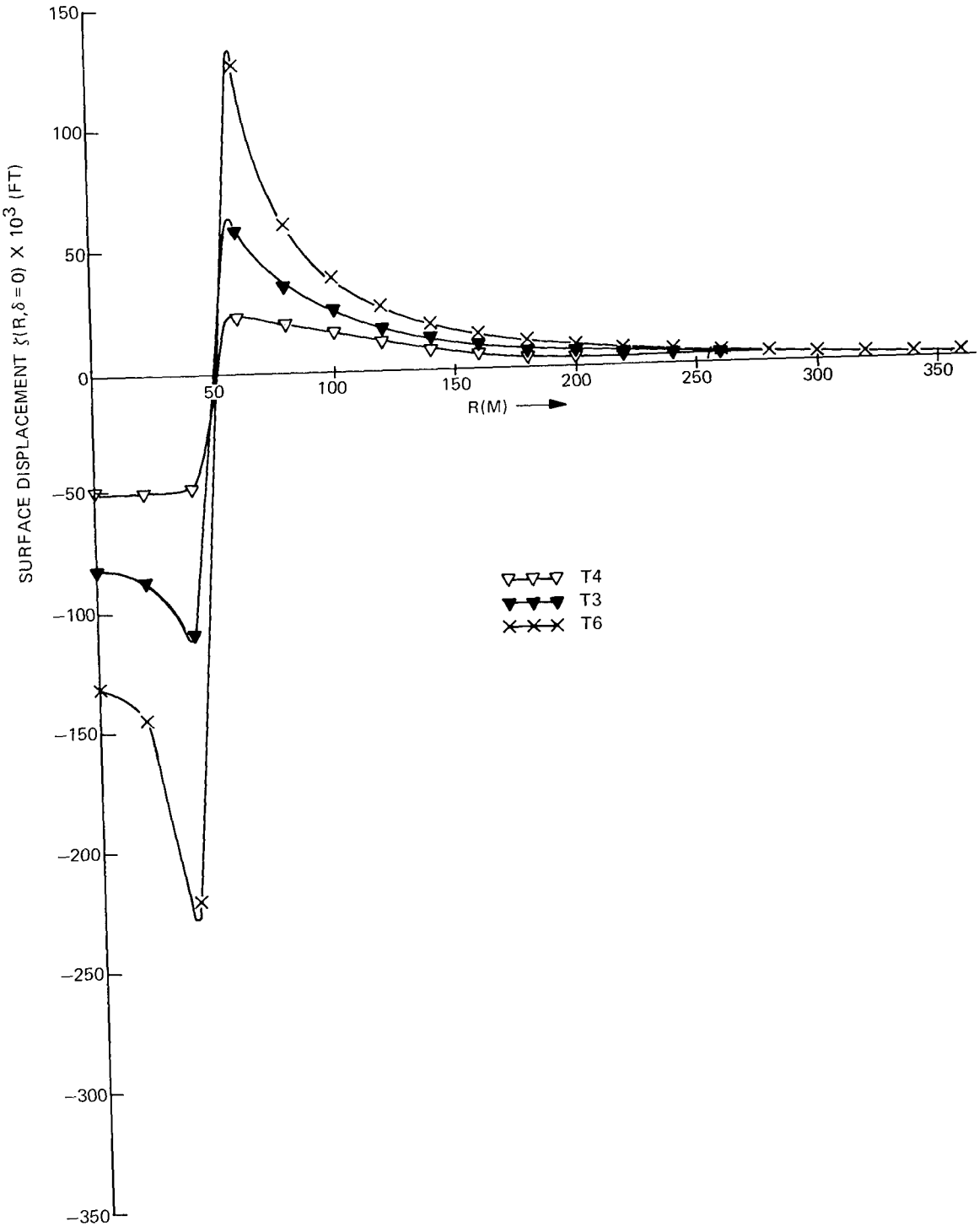

Fig. 18 – Wake-line surface displacement; depth 166 ft, speed 10 knots

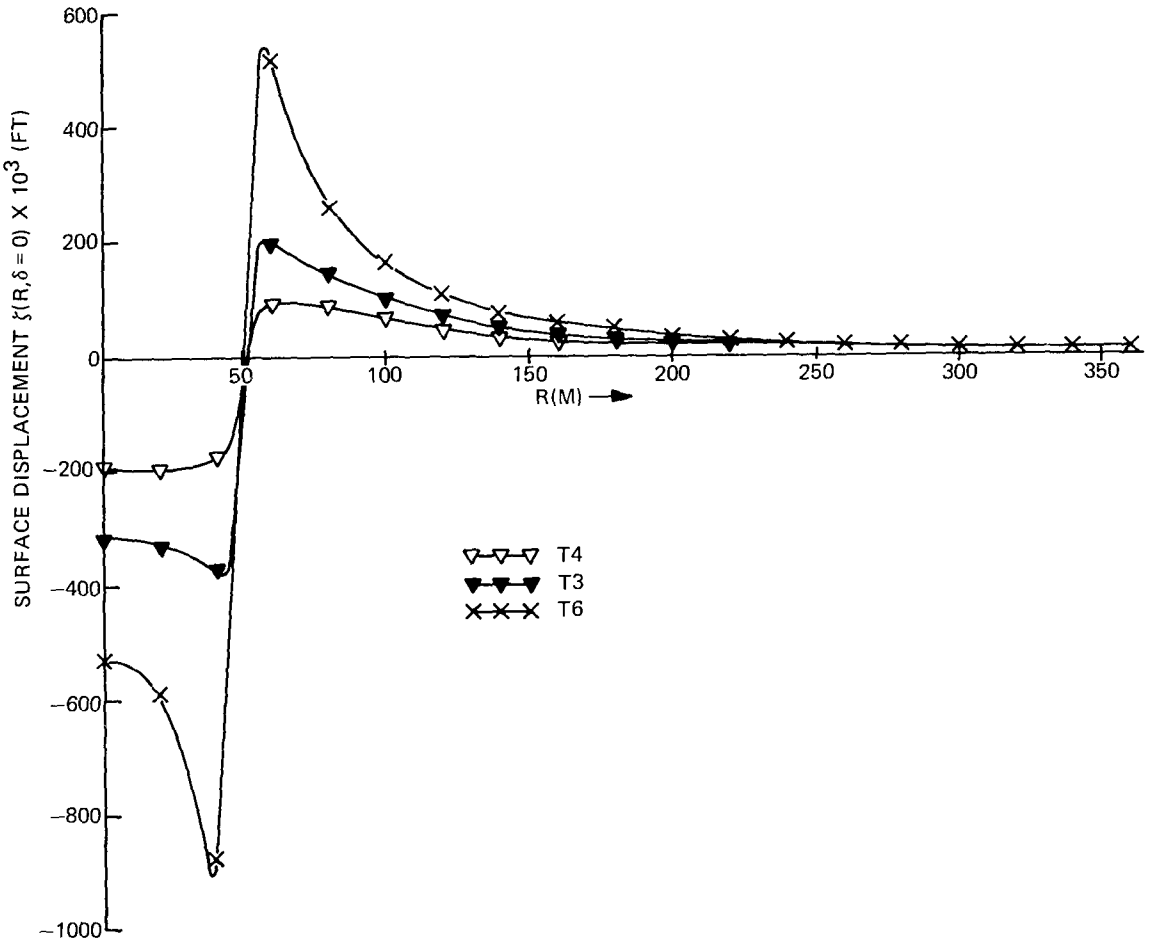

Fig. 19 – Wake-line surface displacement; depth 166 ft, speed 20 knots

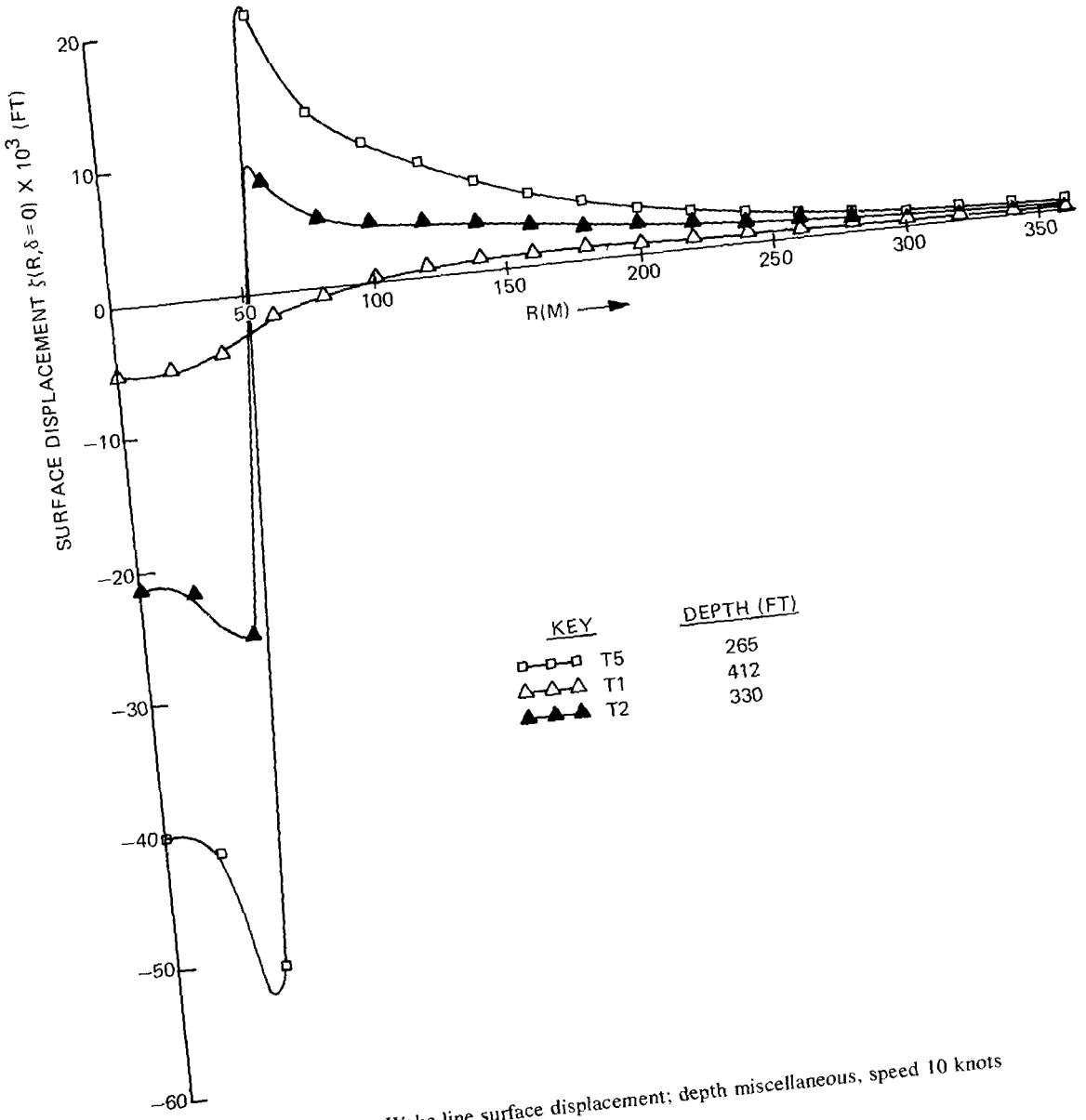

Fig. 20 — Wake-line surface displacement; depth miscellaneous, speed 10 knots

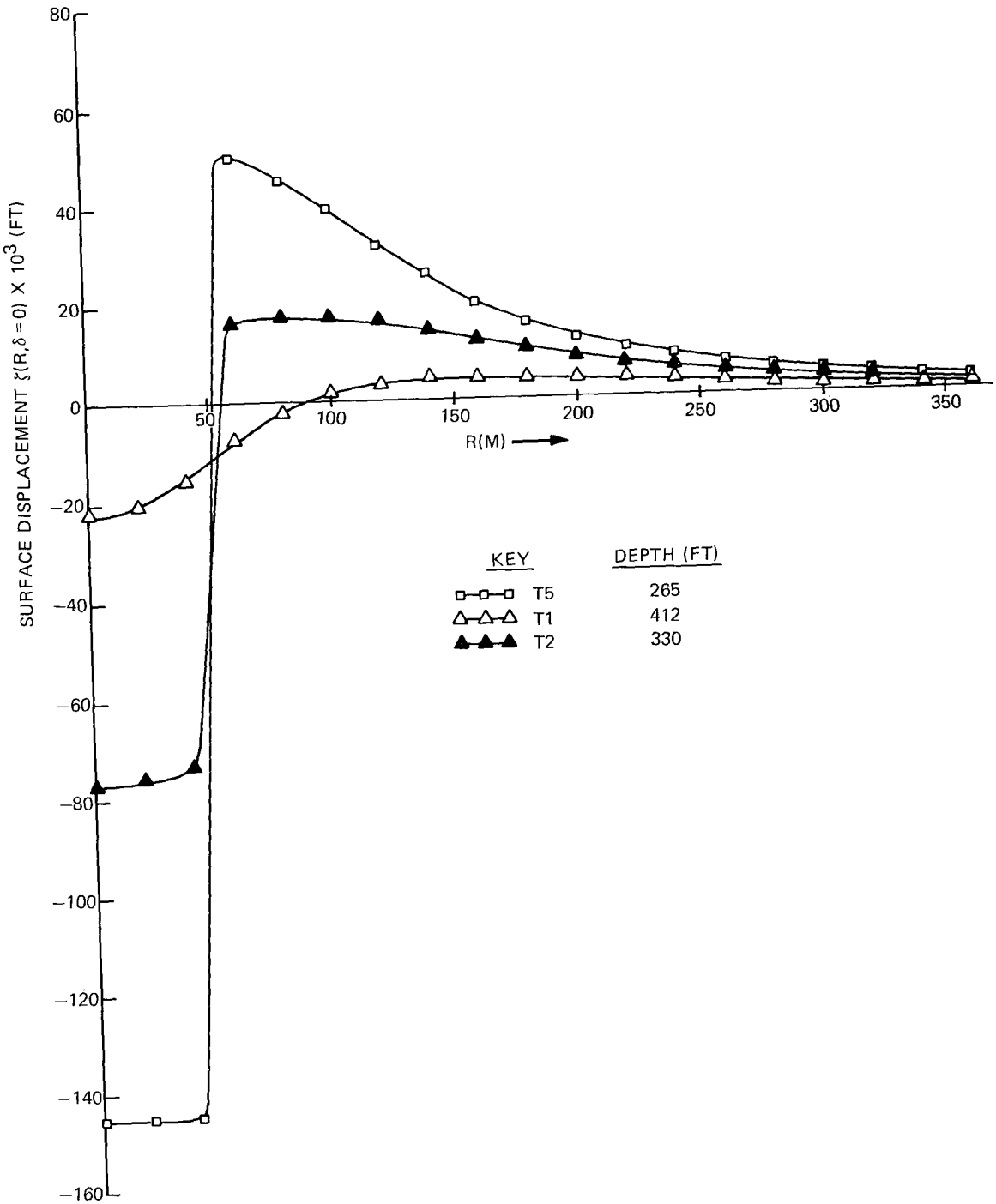

Fig. 21 — Wake-line surface displacement; depth miscellaneous, speed 20 knots

To see better what is going on we compute from Table 3 the ratio of maximum surface displacement for the particular T profile to the same quantity for the H profile and substract unity from it. This is a measure of the enhancement and we relate it to H, the depth to the top of the thermocline, and Δ, the depth of the point source (or sink) beneath the bottom of the thermocline. The results are given in Table 4, where the numbers give the fractional change from the homogeneous fluid results. Actually, therefore, negative numbers indicate a displacement diminution, whereas the positive numbers indicate a displacement enhancement. We see that the parameter $\Delta - H$ is a very relevant one; the enhancements occur when it becomes sufficiently small. The so-called resonance apparently occurs when it goes through zero. It seems to correspond to the increased importance of the terms of Eqs. (76d) and (76e) in the integrals of Eqs. (84) and (92). These terms give the effect of constructive wave interference due to the thermocline boundaries. They are absent when there is no thermocline. The magnitude of their contribution is surprising when there is a square-well thermocline.

The rate-of-strain wake-line dependence is shown for the H and C profiles in Figs. 22 and 23. The same sort of effects occur here. There seems to be no appreciable dependence on the amount of stratification in these profiles. The surface disturbance is again seen to increase with depth and speed.

While the integrals did seem to converge numerically for the H and C profiles in the surface rate-of-strain calculations, and did also for all the profiles in the surface displacement calculations, they did not converge for the T-profile calculations of rate of strain. Consequently, nonsensical rates of strain were calculated for the T profiles. The problem was that the contributions near the end points of the θ integration ($\theta = \pm \pi/2$) were inordinately large and unpredictable, and they gave the principal contribution to the integral. The source of this problem is not clear at this time, but some of the difficulties can be seen from Eqs. (105) and the fact from Eq. (108) that both $\mathscr{F}$ and $\mathscr{G}$ tend to the same bounded asymptotic form for $m_\theta >> \sqrt{V_\theta}$. The extra factor of m in the integrand of S_ℓ makes the asymptotic form $m\mathscr{G}$ unbounded. This problem could be especially severe as $\theta \to \pm \pi/2$, since the exponential damping factor becomes ineffective in aiding the m-integration convergence. The problem is especially heightened in this limit for the T profiles because the condition $m_\theta >> \sqrt{V_\theta}$ is increasingly difficult to realize, and without the asymptotic form of Eq. (108), Filon's method can not be nearly as effectively utilized to speed up the m integration. In addition, the extra factor of $K_0 \sec^2 \theta$ in the integrand of S_ℓ in Eq. (105) magnifies inaccuracies near the $\theta = \pm \pi/2$ limits. This motivated us to try the transformation of Eq. (110), which appears promising because of the factor $1 + u^2$ introduced in the denominator, but the price paid is an infinite upper limit in the u integration. We were not able to complete this in the time frame allotted, so we chose another tack.

It was decided to attempt to estimate rate of strain from the calculated surface displacement. We postulate that S is directly proportional to w at the surface, and therefore to $\partial\zeta/\partial x$ from Eq. (14). The postulate is

$$S \approx -C\, \partial\zeta/\partial x, \tag{111}$$

where C is a factor which may depend on speed, but, hopefully, not much on depth, thermocline characteristics, or anything else. To test this hypothesis we tried it on the calculated surface

Table 4 – Enhancement of Maximum Surface Displacement by the Presence of a Thermocline

B-V Profile Designator	Depth (ft)	$\Delta - H$ (m)	Displacement Enhancement $(T_{max}/H_{max}) - 1$	
			10 knots	20 knots
T1	500	– 17.6	5	2
	412	– 43	0.1	– 0.03
T2	500	37.4	0.6	0.3
	400	6.9	11	8
	330	– 14.4	2	0.8
T3	500	97.4	– 0.2	– 0.07
	400	66.9	– 0.2	– 0.03
	300	36.4	0	0
	200	6.0	3	2
	166	– 4.4	3	1
T4	500	92.4	– 0.3	– 0.1
	400	61.9	– 0.2	– 0.06
	300	31.4	– 0.04	– 0.02
	200	1.0	10	8
	166	– 9.4	0.7	0.2
T5	500	62.4	– 0.2	– 0.06
	400	31.9	0.4	0.2
	300	1.4	11	9
	265	– 9.2	2	1
T6	500	102.4	– 0.2	– 0.2
	400	71.9	– 0.3	– 0.2
	300	41.4	– 0.2	– 0.04
	200	11.0	1	0.5
	166	0.6	3	5

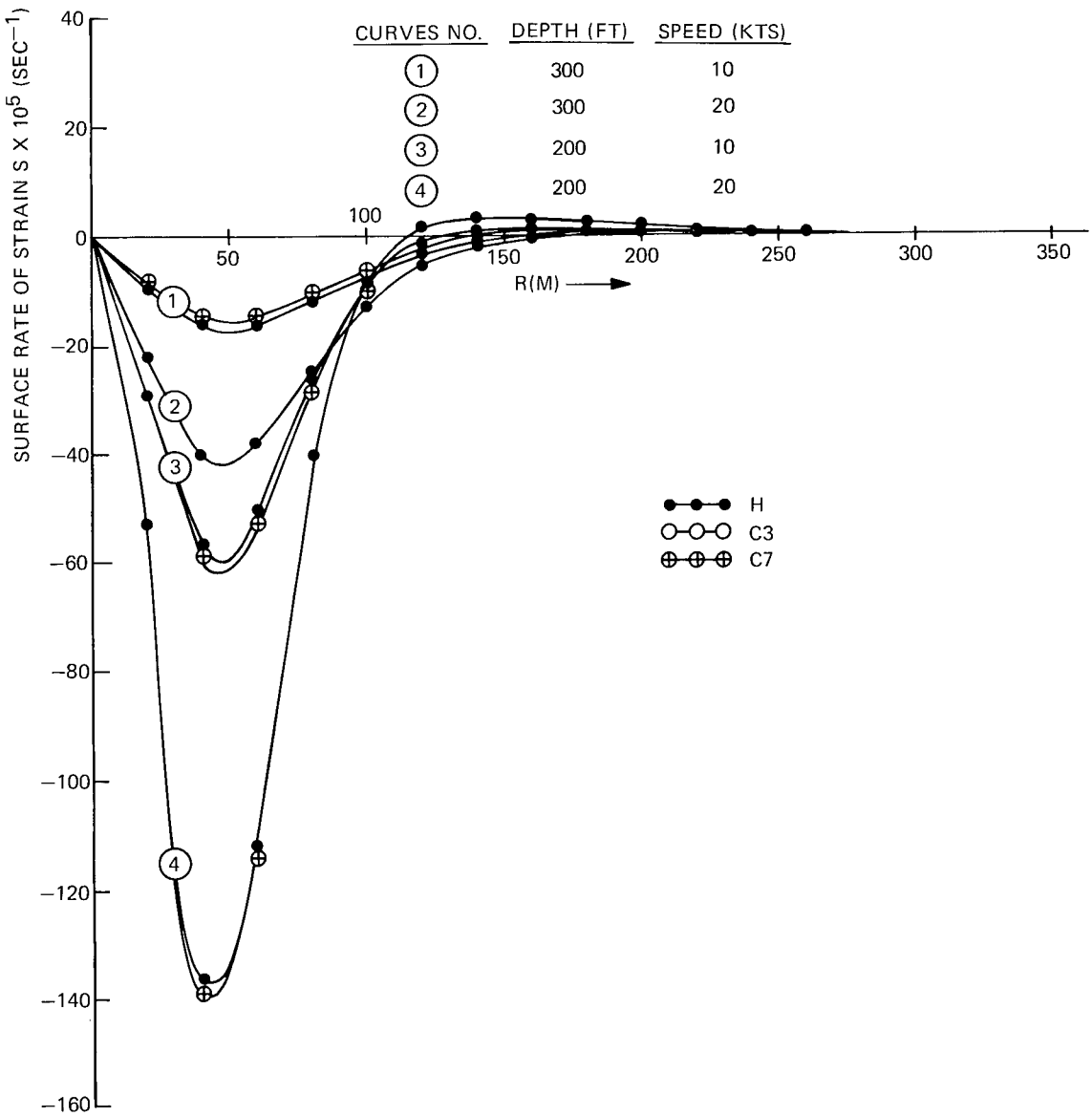

Fig. 22 — Wake-line surface rate of strain; depth variable, speed variable

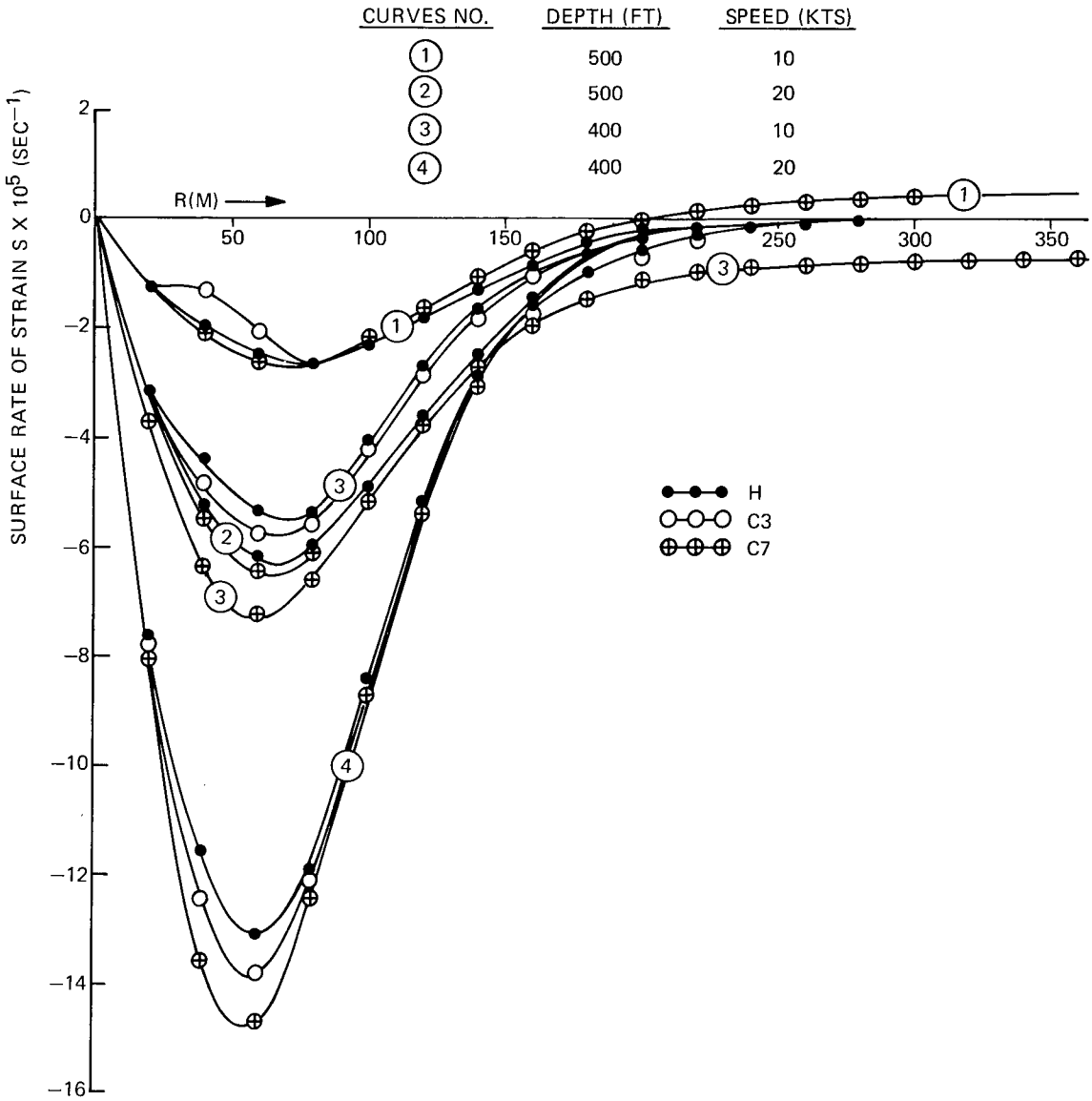

Fig. 23 — Wake-line surface rate of strain; depth variable, speed variable

rate of strain and displacement for the H and C profiles at four depths, for the two speeds, and for two R values. These R values are $20m$ and the value of $R = R_{max}$ at which the rate of strain is maximum. The slopes of S are estimated from Figs. 10-17, and the R_{max} values and appropriate S values are obtained from Figs. 22 and 23. The results are indicated in Table 5. It is seen that the values of C in Eq. (111) do not depend much on depth for a given R. They do depend on R and the velocity U, but all the C values have the same order of magnitude. We are looking for the order of magnitude of the maximum surface rates of strain for the T profiles. The results of Table 5 indicate that Eq. (111) will suffice for this purpose. We can perhaps gain a little more accuracy by using two different constants for the two speeds. Table 5 suggests that we choose

$$C(10\text{ knots}) \approx 2.2\text{ sec}^{-1} \quad \text{and} \quad C(20\text{ knots}) \approx 1.1\text{ sec}^{-1}. \tag{112}$$

Piacsek's results for wake collapse [9] suggest a proportionality between horizontal surface velocity and S of similar accuracy for various thermocline characteristics, so we are further encouraged in this regard.

The maximum surface rates of strain are given in Table 6. These are calculated for the H and C profiles and are estimated according to the method of the preceding paragraph for the T profiles. Just as for the surface displacement, the rate of strain shows a dramatic "resonance" enhancement over and above the H- and C-profile results as $\Delta - H$ approaches zero.

Table 5 – Values of C in the Postulated Relationship $S = {}^{-}C(\delta\zeta/\partial x)$†

Speed (knots)	R Value	Depth (ft)			
		200	300	400	500
10	R_{max}	2.8	2.2	2.1	0.81
	20m	3.9	3.0	3.1	3.4
20	R_{max}	0.93	1.5	1.2	1.1
	20m	2.3	1.6	1.6	1.5

†C is in units of sec $^{-1}$.

Possible Effects of a More Realistic Model

Figure 7 shows that realistic smoothed B-V profiles do not have sharp thermocline boundaries, as in the square-well model we have used. The square-well model is known to overestimate constructive wave interference effects in transmission problems, so it may well be that the sort of resonance enhancement we have found for the surface disturbance as $\Delta - H$ approaches zero would not be nearly as dramatic for a calculation on the more realistic smoothed B-V profile. In addition, we have neglected current shear effects, which can be substantial, although the maximum effect may not be changed drastically [9].

Table 6 — Maximum Surface Rate of Strain, Given $-S_t^{(h)}(R, \delta = 0) \times 10^4$ in sec^{-1}

B-V Profile Designator	Speed of 10 knots					Speed of 20 knots				
	Depth (ft)				Misc. (Rt. Str./Depth)	Depth (ft)				Misc. (Rt. Str./Depth)
	500	400	300	200		500	400	300	200	
CALCULATED										
H	0.25	0.54	1.6	6.0		0.62	1.3	4.0	14	
C1	0.27	0.56	1.6	5.7		0.62	1.3	4.0	14	
C2	0.27	0.55	1.6	5.7		0.62	1.3	4.0	14	
C3	0.26	0.57	1.6	5.6		0.63	1.4	4.0	14	
C4	0.28	0.58	1.6	5.7		0.62	1.4	4.0	14	
C5	0.30	0.55	1.7	5.6		0.63	1.4	4.0	14	
C6	0.23	0.64	1.6	5.8		0.64	1.4	4.0	14	
C7	0.26	0.72	1.5	5.9		0.64	1.5	4.0	14	
ESTIMATED†										
T1	7.4	—	—	—	0.79/412	9.2	—	—	—	1.3/412
T2	1.6	31	—	—	13/330	1.9	59	—	—	17/412
T3	0.22	0.42	1.1	75	85/166	0.48	1.1	3.4	39	130/166
T4	0.20	0.42	1.1	160	40/166	0.48	1.1	3.4	77	66/166
T5	0.18	3.0	80	—	25/265	0.48	3.4	41	—	41/265
T6	0.31	0.35	1.1	26	120/166	0.55	3.4	3.3	44	260/166

†See text.

By restricting attention to smoothed B-V profiles we have neglected considerations of density microstructure. At any instant density variation with depth is not smooth. Indeed, there are also density inhomogeneities in the horizontal plane perpendicular to the depth direction. Present indications are that density microstructure corresponds to a very spiky B-V profile with a length scale of a few meters. The detailed effect of this is not presently clear, but it would seem to act to prevent fluid disturbances from reaching the surface, and it would seem to further legislate against the sort of resonance enhancement we have calculated. To what extent is a subject for future investigations, but all the above considerations may make the H- and C-profile results in tables 3 and 6 closer to the truth than some of the enhanced disturbances calculated with the T profiles and the square-well model.

COMPARISON WITH PREVIOUS RIGID-LID CALCULATIONS OF SURFACE DISTURBANCE INDUCED BY WAKE COLLAPSE

The wake collapse region shown in Fig. 1 has been regarded as contributing significantly to the surface disturbance induced by a deeply submerged body. The relatively slow variation along the wake direction and the gravitational origin of wake collapse in a stratified fluid has enabled

a treatment different from the one we have given [4,6,8,9]. The fully expanded wake, just before collapse, is treated as a mixed region of reduced density gradient, which represents the initial condition in a solution of the Navier-Stokes (N-S) equations. The body does not otherwise appear in the problem. Further, pressure variations along the wake direction are effectively ignored, which enables the solution of the previous equations without this variable in the problem. With respect to Fig. 1, the coordinates in the N-S equations are y, z, and t in an inertial reference frame. This is the so-called $2d + t$ approximation. The body motion is included by the transformation $t \rightarrow [t + (x/u)]$. Finally, the surface boundary condition used in the solution of the N-S equations is that the surface is undisplaced, which only correctly includes internal wave effects, and which we have referred to as the rigid-lid boundary condition.

Piacsek [9] has performed a numerical solution of the N-S equations, which treats wake collapse effects in the above procedure. He has utilized rather good analytic fits [10] to a wide variety of smoothed B-V profiles [16] and a modified Gaussian model for the mixed region of the fully expanded wake [18]. We have given a summary in Table 7 of his results, as we understand them, which apply rather closely to the B-V frequency profiles on which we have made square-well fits. Included in Table 7 are (a) our profile designator, (b) the Dugan parameters [10] (p_1, p_2, p_3) which specify the analytic fit used by Piacsek, (c) the maximum surface value of $\partial u/\partial x$, which corresponds quite closely to our rate of strain, (d) the distance behind the fully expanded wake X_{max} at which the effect occurs for both $U = 10$ knots and $U = 20$ knots, and (e) the transverse distance Y_{max} from the wake line at which the effect occurs. Two depths of the expanded wake center have been considered – viz, 75 and 150m.

Table 7 – Data for Maximum Surface Strain Rates Induced by Wake Collapse

Depth	B-V Profile Designator	Dugan Parameters			$10^4 \times (du/dx)_{max}$ in sec^{-1}	Lag Distance, X_{max}, in km		Y_{max} (m)
		P_1	P_2	P_3		$U = 10$	$U = 20$	
75 m	C1	1	6	6	8.3	34	68	60
≈ 246 ft	T1	5	4	5	4.4	13	26	100
	T2	3	3	3	6.8	13	25	80
	T3	2	2	3	14	24	48	120
	T4	2	1	4	8.4	24	48	180
	T5	3	3	3	10	8	17	80
	T6	2	1	3	7.5	26	52	210
150 m	C1	1	6	6	4.1	76	150	120
≈ 492 ft	T1	5	4	5	2.1	50	100	300
	T2	3	3	3	2.7	87	170	360
	T3	2	2	3	2.5	200	400	380
	T4	2	1	4	1.6	75	150	260
	T5	3	3	3	4.1	58	115	360
	T6	2	1	3	0.80	200	400	380

† Values are taken from Piacsek's calculations.

Tables 6 and 7 reveal some interesting comparisons between the localized surface disturbances induced by the hull and the extended internal wave effects at the surface induced by wake collapse. If we disregard the T-profile surface disturbance enhancements in Table 6, surface rate-of-strain decreases with depth, roughly according to a d^{-3} dependence. The wake-collapse maximum strain rates in Table 7 appear to vary with depth at a slower rate. It appears that the maximum localized hull contribution at higher speeds is somewhat larger down to about 250 ft, and the maximum wake collapse effects become larger for greater depths. Of course, there is a major conceptual difference between the maximum local contribution of the hull and the maximum contribution of wake collapse. Whereas the former occurs in the vicinity of the hull, the latter occurs at very large distance behind the hull, depending on depth, the local B-V frequency at depth, and other factors. Since damping effects are neglected in the calculations, Table 6 shows lag distances between the fully expanded wake position and the maximum surface rates of strain of between 8 and 400 km. Considering these distances, the transverse displacement of these surface disturbances from the wake line is quite small. Internal wave effects at the surface have lag times of tens of minutes.

DISCUSSION

A straightforward method of solving for the disturbance induced by a point source in an incompressible fluid with a free surface has been given in this work. In a real sense this is the Green's function for the problem, and it is the foundation for calculating effects induced by a submerged body, a region of turbulence, or any other perturbation on a static fluid in equilibrium. As is customary, a two-dimensional Fourier transform (FT) was introduced to handle the situation where the static fluid is density stratified along the depth coordinate, and the equations were linearized. This made the calculation of fluid perturbation at sufficient distances from the point source possible. Indeed, the FT of a fluid velocity component $\overline{w}$ is seen to satisfy a wave equation, or equivalently, a one-dimensional Schrödinger equation, where the negative of the square of the B-V frequency plays the part of the depth-dependent potential.

An eigenfunction expansion for the infinite fluid problem was adduced and found to yield a particular solution for $\overline{w}$ in the presence of a point source in the region of interest in the fluid. The straightforward evaluation of this expansion, with the further use of the residue theorem from complex variable theory for the contribution of the continuum eigenstates, was found to be an elegant and powerful method for the evaluation of the particular solution. This was demonstrated in the $\overline{w}$ solution for (a) the homogeneous fluid (Appendix A), (b) the constant-stratification fluid, which involved a small extension of the homogeneous fluid results, and (c) the square-well model, which enabled the addition of the thermocline region. The full solution for $\overline{w}$ was seen to involve the addition of an appropriate solution of the associated homogeneous equation for the infinite fluid (without the point source) whose size was adjusted to satisfy the free-surface boundary condition.

The use of analytically soluble model B-V potentials in the Schrödinger equation for the fluid is a technique which may be useful in future calculations. For example, the potential could be modeled as a series of square-well potentials, histogram style, or it could be modeled as a series of straight-line segments of appropriate slope to fit the B-V profile. These calculations would be

more tedious, but certainly not insurmountable. In this way, one should obtain better fits to the smoothed B-V profiles, but also these models may well be useful for investigation of density microstructure effects.

Viscosity was initially used in the equations to account for causality effects and then was dropped. It was seen to prescribe the treatment of singularities in the evaluation of the inverse FT to obtain the spatial dependence of the fluid disturbance. Other ambiguities were also removed. Contour integration techniques were then used to separate clearly the various contributions; e.g., localized, wavelike, and background stratification contributions are visible as different parts of the contour integration. The influence of surface tension was elaborated (pp. 25-34). Its inclusion in a future calculation may well show interesting effects.

Detailed calculations were carried out for the localized surface disturbance from a submerged Rankine ovoid, sometimes referred to as the Bernoulli depression. Several constant-stratification models were used, as well as square-well model fits to several representative, smoothed B-V profiles found in waters near the United States. The constant-stratification model results differed very little from the homogeneous fluid results, despite the use, for at least one profile, of stratification levels which greatly exceed those ordinarily found in realistic smoothed B-V profiles. On the other hand, the model B-V profiles with square-well thermoclines gave surface disturbances which differed substantially from the homogeneous fluid disturbances. In particular, a sort of resonance enhancement in surface disturbance was observed when the depth of the hull (ovoid) centerline beneath the bottom of the thermocline became comparable with the depth to the top of the thermocline. While the sharp boundaries of the thermocline in the square-well model give order-of-magnitude resonance enhancement of localized surface disturbance above the point source and sink, used to simulate the Rankine ovoid, it is expected that the effects of considering a more realistic fit to the smoothed B-V profile and including density microstructure will substantially reduce the magnitude of this enhancement effect. Nevertheless, this phenomenon deserves further study.

A comparison was made of maximum localized surface rate of strain with previously calculated maximum surface strain rates found from wake collapse. If the resonance enhancement effect mentioned in the preceding paragraph is disregarded, it is found that the localized hull disturbance dominates to a depth of about 200 to 300 ft, but that the wake collapse effects become larger for greater depths. The two different effects occur at different parts of the surface, however, with the localized disturbance in the vicinity of the hull and the internal wave effects from wake collapse considerably to the rear of the hull by as much as tens of kilometers in many cases.

Because of the joint importance of localized and wavelike disturbances to a complete surface pattern, future calculations should include both effects in realistic, model density environments, preferably utilizing a free-surface boundary condition. This work gives a basis for doing this. The point-source problem can be approached as in the above discussion. The hull can be handled by superposition of the contributions from a displaced point source and point sink, as we have done. The sail of a submarine has been simulated by a displaced line source and line sink [2]. It appears that the turbulent wake can be handled similarly [6,8]. The problem is to simulate the streamline behavior near the turbulent wake boundary by a line-density distribution of point sources and sinks. The source density along the wake line must vary to properly account for the

turbulent wake in its growth and collapse stages. A suitably defined quadrupole density has been previously mentioned elsewhere in this regard. An approach like this in principle goes beyond the accuracy of a $2d + t$ approximation, which is often used in wake collapse calculations.

ACKNOWLEDGMENTS

The author would like to thank Mr. Terry R. O'Neal for his able assistance in computer programming, which led, for example, to the results of Table 1 and Figs. 3 and 4. Helpful discussions with Dr. Louis Wetzel and Dr. Alfred Aitken are also gratefully acknowledged.

REFERENCES

1. J. K. Lunde, "On the Linearized Theory of Wave Resistance for Displacement Ships in Steady and Accelerated Motion," Trans. Soc. Naval Arch. Mar. Engrs. **59**, 25-85 (1951).

2. B. Yim, "Waves due to a Submerged Body," Technical Report 231-3, Hydronautics, Inc., Laurel, Md., May 1963.

3. S. F. George and J. D. Wilson, "Local Disturbance due to a Moving Submerged Submarine," NRL Radar Analysis Staff Technical Memorandum No. 33, (Sept. 6, 1973).

4. J. P. Dugan, A. C. Warn-Varnas, and S. A. Piacsek, "Collapse of Partially Mixed Regions in Stratified Fluids," NRL Memorandum Report 2841, July 1974.

5. G. F. Carrier and A. Chen, "Internal Waves Produced by Underwater Vehicles," Hydrodynamic Studies, Final Report, Vol. I, TRW Report 18202-6001R0-00, APL/JHU Issuing No. POR3631, 1971.

6. G. F. Carrier and L. G. Redekopp, "Internal Waves Produced by Underwater Vehicles: The Near Field," TRW Group Report POR-3614, Aug. 1974.

7. J. W. Miles, Geophys. Fluid Dyn. **2**, 63 (1971).

8. C. L. Hindman, "Internal Waves Produced by Collapsing Wakes," TRW Group Report 26062-6002-RU-00 (POR-3609), April 1974.

9. S. A. Piacsek, unpublished wake collapse calculations, Naval Research Laboratory.

10. J. P. Dugan, B-V profile classification procedure in "Free Surface Velocities due to Wake Collapse Phenomenon-Calculations for Smooth Density Profiles," unpublished calculations.

16. T. H. Bell, Jr., A. B. Mays, and W. P. DeWitt, "Upper Ocean Stability: A Compilation of Density and Brunt-Vaisala Frequency Distributions for the Upper 500 m of the World Ocean," NRL Reports 7799, 7800, Oct. 1974.

11. L. D. Landau and E. M. Lifshitz, *Fluid Mechanics*, Addison-Wesley, Reading, Mass., 1959, Sec. 15.

12. Chia-Shun Yih, *Fluid Mechanics*, McGraw Hill, New York, 1969, pp. 67-69.

13. See, e.g., L. I. Schiff, *Quantum Mechanics*, 3d ed., McGraw-Hill, New York, 1968, Sec. 90.

14. See, e.g., G. Arfken, *Mathematical Methods for Physicists*, p. 268 (Academic Press, New York, 1966).

15. See e.g., L. M. Milne-Thomson, *Theoretical Hydrodynamics*, Chap. XVI (Macmillan New York, 1974).

17. B. Noble, *Numerical Methods; 2, Differences, Integration, and Differential Equations,* Interscience Publishers, Inc., New York, 1964, pp. 242-253.

18. J. P. Dugan, A. C. Warn-Varnas, and S. A. Piacsek, "Numerical Model for Mixed Region Collapse in a Stratified Fluid," NRL Memorandum Report 2597, June 1973.

Appendix A
HOMOGENEOUS FLUID SOLUTION FOR $\bar{w}$

The eigenvalue Eq. (28), using Eq. (30), is

$$u_{zz} + k^2 u = 0 \Longrightarrow u_k = (2\pi)^{-1/2}\, e^{\pm ikz}, \tag{A1}$$

and we must use both degenerate states in the eigenfunction expansion of Eq. (29). Hence, Eq. (31) becomes (if $x_s = y_s = 0$)

$$\bar{w}_\rho(K, z) = \frac{M}{2\pi} \int_0^\infty dk\, \frac{ik\, e^{-ik(z-z_s)} - ik\, e^{ik(z-z_s)}}{k^2 + K^2}$$

$$= \frac{M}{2\pi i} \int_{-\infty}^{\infty} dk\, \frac{k}{(k + iK)(k - iK)}\, e^{ik(z-z_s)}. \tag{A2}$$

The contour may be closed by an infinitely large semicircle in the upper half-plane for $z - z_s > 0$ and in the lower half-plane for $z - z_s < 0$. By the residue *th* we obtain

$$\bar{w}_\rho(K, z) = \begin{Bmatrix} (M/2) \exp\,[-K(z - z_s)] \\ -(M/2) \exp\,[\ \ K(z - z_s)] \end{Bmatrix} \text{ for } z - z_s \begin{Bmatrix} > 0 \\ < 0 \end{Bmatrix}. \tag{A3}$$

The solution of the homogeneous Eq. (36) which satisfies Eq. (32) is

$$\bar{w}_H(K, z) = Ae^{Kz}, \tag{A4}$$

and A is determined from Eq. (37). For simplicity we suppose $z > z_s$, so that the free-surface boundary condition at $z = 0$ becomes

$$A(K \cos^2 \theta - K_0) = (M/2)\, e^{Kz_s}(K \cos^2 \theta + K_0). \tag{A5}$$

The full solution for $z > z_s$ is

$$\bar{w}(K, z) = \bar{w}_\rho + \bar{w}_H = \frac{M}{2}\left[e^{-K(z-z_s)} + \frac{K + K_0 \sec^2 \theta}{K - K_0 \sec^2 \theta}\, e^{K(z+z_s)}\right]. \tag{A6}$$

Appendix B
EVALUATION OF $\overline{W}_{p2}^{C}$

From Eq. (52) we have

$$\overline{w}_{p_2}^{C} = M\int_0^\infty dk\ [\rho^2/(k^2 + K_\theta^2)]\ (N_k^2/k)\cos 2\rho \sin k(z + H)\cos k\Delta$$

$$= (M/4)\int_{-\infty}^{\infty} dk[\rho^2/(k^2 + K_\theta^2)](N_k^2/k)\cos 2\rho[\sin k(z + H + \Delta) + \sin k(z + H - \Delta)]$$

$$= -(iM/4)\int_{-\infty}^{\infty} dk[\rho^2/(k^2 + K_\theta^2)]\ (N_k^2/k)\cos 2\rho\Big[e^{ik(z+H+\Delta)} + \begin{cases} -e^{ik(\Delta - z - H)} \text{ for } \Delta - z - H > 0 \\ e^{ik(z+H-\Delta)} \text{ for } z + H - \Delta > 0 \end{cases}\Big].$$

In the second line of this equation a trigonometric identity is used, and the lower limit of the integral is extended to $-\infty$, where we use the fact that the integrand is even in k. We use this fact again in the third line, which is written this way so that we can now close the contour with a semicircle of infinite radius in the upper half-k-plane. Only the pole at $k = iK_\theta$ is enclosed,† as well as the poles on the imaginary k axis associated with N_k^2 (see Eqs. (53) - (56)) at $k = ik_j$. By the residue theorem

$$\overline{W}_{p2}^{C} = 2\pi i\ [\mathscr{R}(iK_\theta) + \Sigma_j \mathscr{R}(ik_j)], \tag{B2}$$

where, e.g., $\mathscr{R}(iK_\theta)$ is the residue at the pole $k = iK_\theta$. With use of Eq. (56) we obtain

$$\overline{W}_{p2}^{C} = -\frac{1}{4}\frac{\rho(iK_\theta)^2 \cos 2\rho(iK_\theta)}{K_\theta^2 - V_\theta \cos^2 \rho(iK_\theta)}\ [e^{-K_\theta(\Delta + z + H)} - \operatorname{sgn}(\Delta - z - H)\ e^{-k_\theta|\Delta - z - H|}]$$
$$+\frac{1}{4}\Sigma_j \frac{\rho(ik_j)^2 \cos 2\rho(ik_j)}{(K_\theta^2 - k_j^2)(1 - F_j k_j)}\ [e^{-k_j(\Delta + z + H)} - \operatorname{sgn}(\Delta - z - H)\ e^{-k_j|\Delta - z - H|}]. \tag{B3}$$

The inclusion of the poles associated with N_k^2 effectively removes the singularities associated with the first term.

---

†For K very slightly below the real axis, one has from Eq. (51),

$$K_\theta = \begin{cases} \sqrt{K^2 - V_\theta^r} - i\delta & \text{for} \quad \operatorname{Re} K > \sqrt{V_\theta^r} \\ -i\sqrt{V_\theta^r - K^2} + \delta & \text{for} \quad \operatorname{Re} K < \sqrt{V_\theta^r} \end{cases}$$

where δ is a small positive number.

Appendix C
Analytic Continuation of $F(z) = \sqrt{z^2 - a^2}$

We have

$$F(z) = \sqrt{(z-a)(z+a)} = \sqrt{r_1 r_2}\, e^{i(\theta_1+\theta_2)/2} \equiv \rho e^{i\phi}$$

where

$$z - a \equiv r_1 e^{i\theta_1} \quad \text{and} \quad z + a \equiv r_2 e^{i\theta_2} \tag{C1}$$

The situation is as depicted in Fig. C1 where a is real.

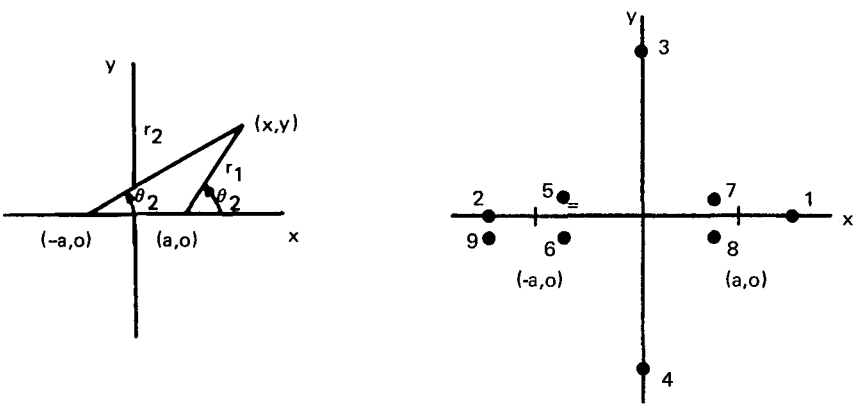

Fig. C1 – Complex z-plane and relevant parameters

Here

$$\begin{aligned} z &= x + iy \\ r_1 &= \sqrt{(x-a)^2 + y^2} \\ r_2 &= \sqrt{(x+a)^2 + y^2} \\ \theta_1 &= \tan^{-1}\frac{y}{x-a} \\ \theta_2 &= \tan^{-1}\frac{y}{x+a} \end{aligned} \tag{C2}$$

where $-\pi < \theta_1, \theta_2 \leq \pi$. In the second part of the sketch are shown eight numbered points; nos. 1-4 are on the axis and nos. 5-8 are near the real axis (within a very small distance ϵ). With these formulas we construct Table C1.

Noteworthy is that phase ϕ jumps discontinuously in crossing the real axis from point 5 to point 6 or from point 7 to point 8. If we exclude the branch cut from $(-a, 0)$ to $(a, 0)$ on the real axis from consideration, the function $F(z)$ is indeed single valued and analytic everywhere else in the z plane, as can be seen by considering the phases in the sequence (9, 6, 4, 8, 1.7, 3, 5, 2), for example. Put another way, the function $F(z)$ is single valued and analytic on one of the two Riemann sheets ($-\pi < \phi \leq \pi$ and excluding the branch cut).

Table C1—Complex Z-plane

Point	Coordinates $[x, y]$	r_1	r_2	θ_1	θ_2	ϕ
1	$[x, 0]$ } $x > a$	$x - a$	$x + a$	0	0	0
2	$[-x, 0]$ }	$x + a$	$x - a$	π	π	π
3	$[0, y]$ } $y > 0$	$\sqrt{a^2 + y^2}$	$\sqrt{a^2 + y^2}$	$\pi - \alpha$	α } $(\alpha > 0)$	$\pi/2$
4	$[0, -y]$ }			$-(\pi - \alpha)$	$-\alpha$ }	$-\pi/2$
5	$[-x, \epsilon]$ } $0 < x < a$	$a + x$	$a - x$	π	ϵ	$\pi/2 + \epsilon$
6	$[-x, -\epsilon]$ }			$-\pi$	$-\epsilon$	$-\pi/2 - \epsilon$
7	$[x, \epsilon]$ }	$a - x$	$a + x$	$\pi - \epsilon$	0	$\pi/2 - \epsilon$
8	$[x, -\epsilon]$ }			$-(\pi - \epsilon)$	0	$-\pi/2 + \epsilon$
9	$[-x, -\epsilon]$ $x > a$	$x + a$	$x - a$	$-\pi$	$-(\pi - \epsilon)$	$-\pi + \epsilon$

Appendix D
FILON'S METHOD AND RELEVANT PROCEDURES

Given is the integral

$$G(a, b) = \int_a^b F(x) f(x)\, dx \tag{D1}$$

which is to be evaluated numerically. The interval (a, b) is divided into $2n$ subintervals, each of width h, where n is an integer. There are $2n + 1$ associated mesh points and function values f_i $(i = 1, 2, \ldots, 2n + 1)$. The integrand is factored in such a way that $F(x)$ is analytically integrable, and the mesh size h need only be small enough that $f(x)$ can be reasonably accurately fitted by a parabola in an adjacent pair of subintervals, i.e., by a second-order Taylor expansion about the center of this pair of subintervals. Then

$$\begin{aligned} G(a, b) &= \sum_{r=1}^{n} \int_{x_{2r}-h}^{x_{2r}+h} dx\, F(x) \left\{ \frac{f_{2r+1} + f_{2r-1} - 2f_{2r}}{2h^2} (x - x_{2r})^2 + \frac{f_{2r+1} - f_{2r-1}}{2h} (x - x_{2r}) + f_{2r} \right\} \\ &= \sum_{r=1}^{n} (h/2) \left[(f_{2r+1} + f_{2r-1} - 2f_{2r})\, I_2(x_{2r}) + (f_{2r+1} - f_{2r-1})\, I_1(x_{2r}) + 2f_{2r}\, I_0(x_{2r}) \right] \\ &= \sum_{r=1}^{n} (h/2) \left\{ f_{2r-1}[I_2(x_{2r}) - I_1(x_{2r})] + 2f_{2r}[I_0(x_{2r}) - I_2(x_{2r})] \right. \\ &\qquad \left. + f_{2r+1}[I_2(x_{2r}) + I_1(x_{2r})] \right\} \end{aligned} \tag{D2}$$

where

$$I_j(x) \equiv \int_{-1}^{1} du\, F(hu + x)\, u^j \qquad (j = 0, 1, 2).$$

As an application of this method, the reader can verify that Simpson's rule is obtained for the special case $F(x) = 1$ in Eq. (D1). Another case we use is for the functions

$$F^{(1)}(m) \equiv e^{-m\omega}, \qquad F^{(2)}(m) \equiv e^{-m\omega} \cos md, \qquad F^{(3)}(m) \equiv e^{-m\omega} \sin md \tag{D3}$$

and associated integrals $G^{(1)}$, $G^{(2)}$, and $G^{(3)}$ in Eq. (D1). The latter integrals are all obtained from the evaluation of

$$\mathcal{G} \equiv \int_a^b \mathcal{F}(m) f(m)\, dm,$$

where

$$\mathcal{F}(m) \equiv e^{-m\omega}\, e^{imd}. \tag{D4}$$

Assuming that $f(m)$ is real,

$$G^{(1)} = \lim_{d \to 0} \text{Re}\,(\mathcal{G}), \qquad G^{(2)} = \text{Re}\,(\mathcal{G}), \qquad G^{(3)} = \text{Im}\,(\mathcal{G}) \tag{D5}$$

and the integral

$$I_j(m) \equiv \int_{-1}^{1} du\, u^j\, e^{-(m+hu)\omega}\, e^{i(m+hu)d} \tag{D6}$$

associated with Eq. (D2) is easily evaluated. For constant stratification ($V_\theta = 0$, but $V_\theta{}^r \neq 0$) we are faced with evaluation of integrals of the type in Eq. (D3), but with m in the trigonometric functions replaced by $m_\theta = \sqrt{m^2 + V_\theta{}^r}$. To take advantage of Filon's method, we cast the problem in the form of Eq. (D4), where the real function $f(m)$ is, however, replaced by a complex function which approaches it as m becomes large. The replacement is

$$f(m) \to e^{i(m_\theta - m)d} f(m_\theta). \tag{D7}$$

The evaluation procedure of Eq. (D5) is unchanged, albeit slightly complicated by the fact that the function in Eq. (D7) is now complex.

The integral in Eq. (D6) can be rewritten as

$$I_j(m) = e^{-m\alpha/h} J_j(\alpha),$$

where $\alpha \equiv h(\omega - id)$, and

$$J_j(\alpha) = -(\partial/\partial\alpha)^j J_0(\alpha), \tag{D8}$$

where

$$J_0(\alpha) = \int_{-1}^{1} du\, e^{-u\alpha} = \frac{1}{\alpha}(e^{\alpha} - e^{-\alpha}).$$

These procedures simplify the evaluation.